Modeling of two-body fatigue wear of cylinder liner in internal combustion engines during the break-in period and its impact on engine lubrication

by
Chongjie Gu

B.Sc., Mechanical Engineering
Purdue University, 2015
Shanghai Jiao Tong University, 2015

Submitted to the Department of Mechanical Engineering in Partial Fulfillment of the
Requirements for the Degree
of
Master of Science in Mechanical Engineering

at the
Massachusetts Institute of Technology

June 2017

Signature of Author: Signature redacted

Department of Materials Science and Engineering
May 15, 2017

Certified by: Signature redacted

Dr. Tian Tian
Principal Research Engineer, Department of Mechanical Engineering
Thesis Supervisor

Accepted by: Signature redacted

Rohan Abeyaratne
Professor of Mechanical Engineering
Chair, Departmental Committee on Graduate Students

Modeling of two-body fatigue wear of cylinder liner in internal combustion engines during the break-in period and its impact on engine lubrication

by

Chongjie Gu

Submitted to the Department of Mechanical Engineering on May 15, 2017 in Partial Fulfillment of the Requirements for the Degree of Masters of Science in Mechanical Engineering

Abstract

Internal combustion engines are widely utilized in modern automobiles. Around 10% of the total fuel energy is dissipated to heat due to mechanical friction, among which 20% is caused by the contact between the cylinder liner and the piston rings. The wear of cylinder liner not only leads to surface damage, but also results in the change of liner lubrication conditions. Therefore, a large number of tests are performed by researchers to investigate the liner wear process and its impact on engine lubrication. This work is the first step toward developing a wear model to predict the evolution of liner roughness and ring pack lubrication during break-in period.

A physics-based liner wear model is built in this work, with focus on two mechanisms: surface plastic flattening and fatigue wear. Both mechanisms are simulated through a set of governing equations and are coupled together to complete the algorithm of the liner wear model. Simulations of break-in wear are performed to different liner surfaces finishes, with different external normal pressures. Simulation results indicate that the liner wear rate depends on the size and shape of liner surface asperities, which may provide guidance for surface manufacturing. The results also show consistence with the Archard's wear law, describing the proportional correlation between normal pressure and steady state wear rate.

This wear model is then used to study the influence of liner wear on engine lubrication. Through the friction for entire engine cycles, simulated results are compared with experimental friction measurements. The comparison shows that the calculated friction evolution during break-in has the same trend and comparable magnitude as the measurements, indicating the efficiency of the wear model. Some initial work of modeling of third-body abrasive wear is also discussed in this thesis.

Thesis Supervisor:

Dr. Tian Tian
Department of Mechanical Engineering
Massachusetts Institute of Technology

Acknowledgements

For the past two years, I received support and contributions to my thesis work from many people around me. Without their help, it would be much more difficult for me to overcome the barriers in my study life at MIT.

First of all, I would like to thank my advisor, Dr Tian Tian, for his consistent support and guidance throughout my research at MIT. The topic of modeling of cylinder liner wear was introduced to me by him, without whom the completion of this work would by no means be possible. I highly appreciate his knowledge, rich experience in academic areas and the logical thinking habit, from which I can benefit for my whole life.

This work is sponsored **by** the consortium on lubrication in internal combustion engines. The current consortium members are: Daimler, Mahle, PSA, Renault, Toyota, Volkswagen, Volvo, Shell and Wei Chai. I would especially like to thank Daimler, and their representatives, Hans-Juergen Fuesser and Matthias Martin. They strongly supported my internship in Daimler and gave me a lot of guidance both in academic areas and in life. I would also like to thank my colleagues in Daimler, especially Petra Obert and Michael Simon.

I am gratitude to my laboratory mates for their kind help and friendship. They are: Vinayak Teja Kalva, Yang Liu, Tianshi Fang, Yuwei Li, Sebastian Ahling, Zhen Meng, Qin Zhang; Mohamed Aziz Bhouri, Zhe Chen and Xiaofeng Qin. I would also like to thank former students in this group, especially Renze Wang, Haijie Chen, Kai Liao and Dallwoo Kim. They provide me both theoretical models and experimental results.

Finally, I would like to thank my friends and family members for their love and support throughout my life.

Table of Contents

Chapter 1. Introduction

1.1 Project motivation

Although the application of electric vehicles is a popular engineering topic nowadays, internal combustion engines are still widely utilized in modern automobiles. With the goal of pollution control and reduction of greenhouse gas emissions, it is always important to increase the engine's efficiency. An essential source of engine friction is the contact system of piston rings and cylinder liners. Averagely, for an internal combustion engine, around 10% of the total fuel energy is dissipated to heat due to mechanical friction. About 20% of the friction loss is caused by the contact of piston rings and liners [1].

Besides friction loss, the contact of a piston ring and liner also lead to wear of both surfaces of the ring and the liner, which can cause negative effect in friction reduction. The reason is directly related to the surface plateau-honed structures of cylinder liners. A critical manufacturing step in the manufacturing process of liners is called the plateau-honing process. The process includes three stages: rough honing, creating the valley part with grooves and fine honing leading to much smaller plateau roughness compared with valleys [2][3]. A typical honing structure is plotted in Figure 1.1. As the honing structure is gradually removed during the break-in period, the lubricant conduction can become worse and cause more friction loss. Therefore, it is interesting to study the break-in wear of the liner surface.

Currently, the methodology of studying the break-in wear process of cylinder liners is mainly based on experiments. Using tribometers to perform tests on liner samples or ring segments is a common way to investigate wear, friction or lubrication conditions. However, such a way is actually expensive and time consuming. Instead, the goal of this project is developing a computational wear model to reduce the amount of real wear experiments, investigate some properties of break-in wear and its influence on engine lubrication.

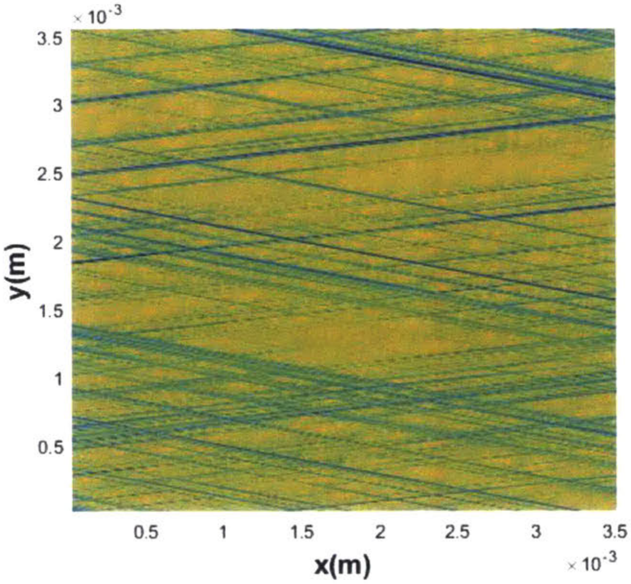

Figure 1.1 2-dinmensional plot of a liner surface with plateau and valley regions

1.2 Sliding wear of the engine liner

Wear is a direct result of surface to surface contact, either direct dry contact or lubricated contact. Based on the motion pattern, dynamic contact between two solid bodies can be divided into rolling contact or sliding contact, as shown in Figure 1.2 and 1.3.

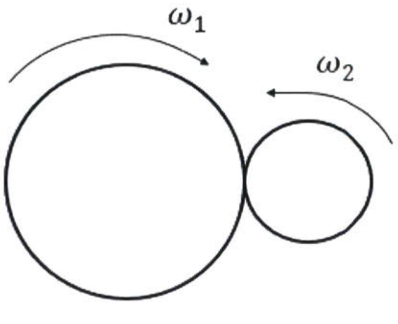

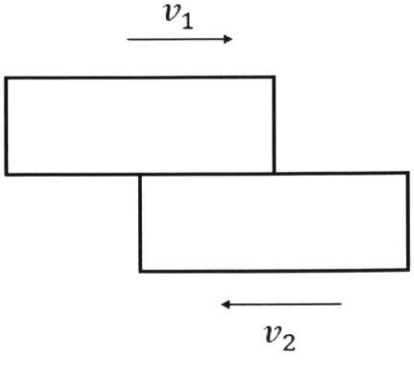

Figure 1.2 Rolling contact

Figure 1.3 Sliding contact

Sliding wear of metals can be influenced by many factors: constitutional relationship of materials, shape and size of surface asperities, sliding speed, contact pressure, and the ambient conditions.

1.2.1 Mechanisms of sliding wear

Three major mechanical mechanisms are involved in sliding wear of metals: surface asperity deformation, delamination due to fatigue, and abrasion of third-body particles. The first two mechanisms are components of two-body wear since they are caused by the direct contact of the sliding surfaces. In fact, some other non-mechanical mechanisms can also influence the wear of sliding, such as erosion and formation of tribolayers. In this thesis, only mechanical mechanisms are discussed and modeled.

Unlike fatigue and third-body abrasion, deformation of surface asperities occurs immediately after the two surface come into direct contact. The contact load between surfaces is transmitted through contact asperities, so that the real contact area is much smaller than the nominal area. Asperities of the softer surface are easily deformed and fractured under cyclic loadings. The contact among surfaces asperities can be elastic, elastoplastic or fully plastic, with permanent deformation if the contact between and two asperities involves plasticity. This mechanism dominates the surface topology change during the early stage of sliding wear, but continues as a minor mechanism after the transient period.

Fatigue wear occurs at least after several hundreds of sliding cycles, since cracks below contact asperities need repetitive loadings to propagate and finally lead to asperity fractures. Because of the existence of material flaws and different metal phases, voids can be initiated based on these structures under external loads. Then, cracks begin to propagate, starting from the generated voids, until reaching the edge of contact areas of asperities. The wear rate of fatigue wear is determined by the void nucleation position and the crack propagation rate.

Third-body abrasive wear is caused by particles trapped between the two surfaces, which can be soot or wear debris. When these particles are large, with average hardness comparable to the original surfaces, severe wear can occur [4]. In sliding wear, third-body wear happens after some asperities are fractured to become wear particles, and it will become even more severe because particles may agglomerate under some certain conditions. However, the honing structure on the liner surface can reduce third-body wear to some extent, since many particles are removed into deep valleys during sliding motions to prevent further scratching.

1.2.2 Sliding wear of the engine liner

As a specific wear condition, internal combustion engine liner wear has some special characteristics, which makes it possible to model the wear process under some assumptions.

As shown in Figure 1.4, the green line indicates the top position of the lubricated area on the ring surface as a function of the crank angle, while the blue line and red line represent the bottom position and minimum oil thickness position, respectively. When the piston moves to the top dead center, with the crank angle near zero, these three lines combine into one, indicating that the contact is almost dry in the top dead center. The top dead center is the focused region in this project as it usually experiences the most severe wear. Therefore, one important assumption can be made for wear in the top dead center is that no lubricant exists in the clearance between the liner and the piston ring. This assumption greatly simplifies the contact condition since the coupling of fluids and solids can be neglected.

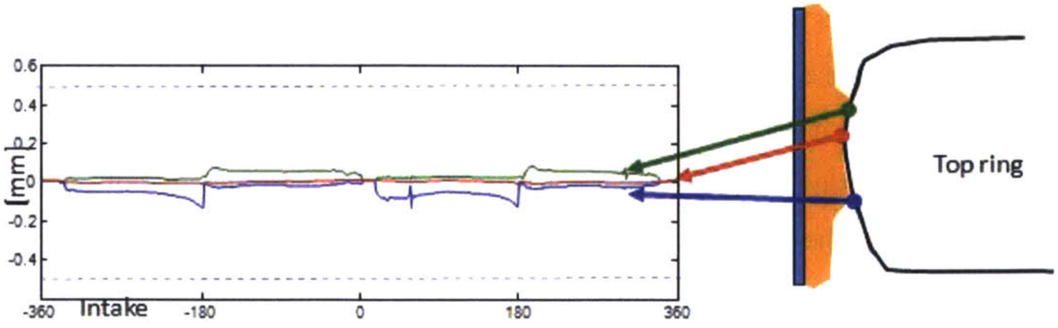

Figure 1.4 Lubrication conditions of the contact between liner and top ring [5]

Another special condition for the wear of liner is that the ring surface is much smoother than the liner surface, due to the diamond like carbon (DLC) coatings on piston ring surfaces [6]. Based on this, it is reasonable to assume that the ring is perfectly smooth and hard, so that wear only happens on the liner surface. This assumption is appropriate during the break-in period, but gradually becomes invalid because piston rings can experience wear after a long time of repetitive sliding motions against the liner. In this project, only break-in wear is studied and modeled, making this assumption efficient and useful.

1.2.3 Modeling of the engine liner wear

With some assumptions to simplify the physical situation, it is possible to model the break-in wear of the engine liner. Most of the previous work about engine liner wear modeling is mainly built through statistical approaches. According to Rafal Reizera and Pawel Pawlus, a statistical correlation can be used in wear modeling. The standard deviation of plateau part (Spq) and the core roughness height of the surface obey an approximate linear relationship [7]. This is useful when the interest is about some certain statistical parameters during wear. However, the work of Rafal Reizera is not possible to be directly applied to simulate the change of surface topology.

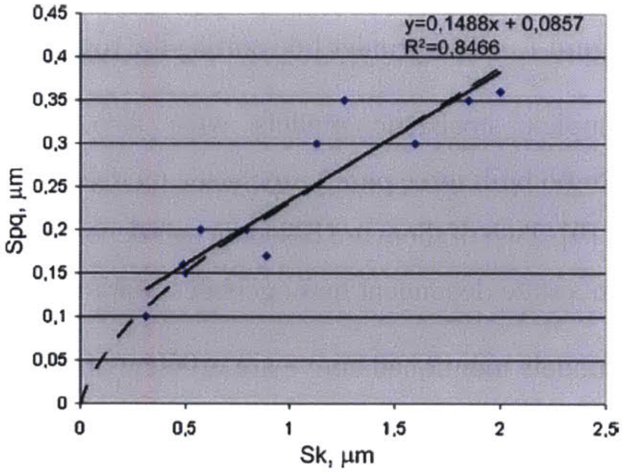

Figure 1.5 The correlation between Spq and Sk during wear [7]

A simple grinder model is built to simulate the wear process by Haijie Chen [8]. As shown in Figure 1.6, the wear process of a rough surface is modeled through cutting by a grinder line, which is created by a Gaussian random factor. The grinder liner slides back and forth, above the rough surface with a certain clearance. Once the grinder line interacts with the surface, a random proportion of the interacted volume is removed from the surface. The random proportion obeys a uniform distribution between 0 and 1. Adjusting the arbitrary parameters in a certain way, Chen was able to duplicate the hydrodynamic lubrication os an actual worn surface [8]. However, this model is purely mathematical and does not have predictive capability relating surface change with materials and rubbing time.

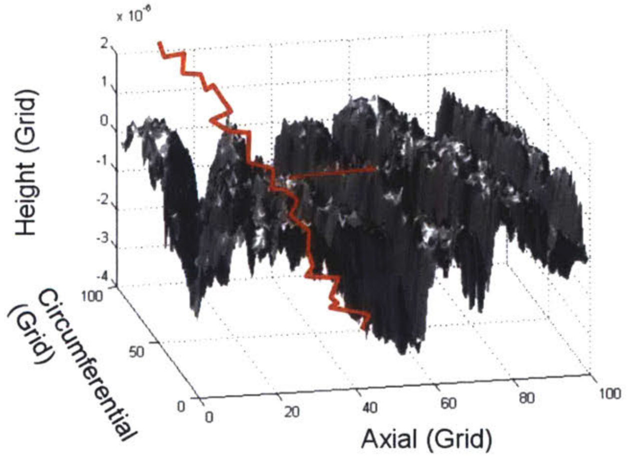

Figure 1.6 The grinder line cutting the rough surface [8]

Some other complex stochastic models were also established. For example, Massimiliano Giorgio built three purely stochastic models to simulate the wear process of cylinder liners [9]. Two of them are based on age-dependent processes, and the third model is based on a state dependent homogeneous Markov chain.

Statistical wear models mentioned above are efficient and useful in many conditions. However, statistical models are strictly limited to testing conditions from which input data is generated. It is usually very difficult to modify parameters in a statistical model if the external physical inputs are changed. Therefore, in this project, a physics-based liner wear model is established to connect input parameters with real mechanisms involved during wear.

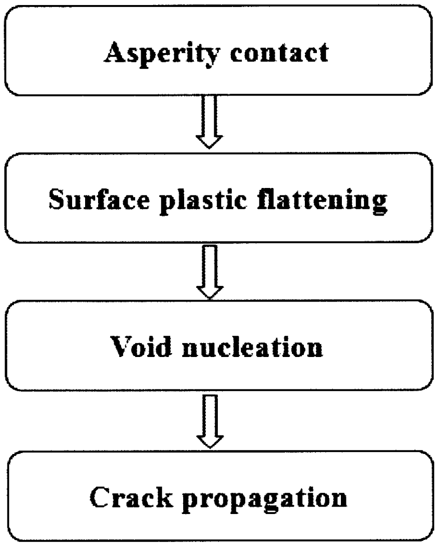

Figure 1.7 The wear model in this project

The two-body wear model of cylinder liner developed in this project is completed based on physical wear mechanisms. As shown in Figure 1.7, the model has several submodels, which are exactly the major mechanisms in break-in wear. Each submodel has one or more governing equations to carry the computation, which will be discussed in the flowing chapters. The model is able to simulate the surface topology change during break-in period under different external pressures. This model is a two-body wear model, only considering the direct contact between the liner and the piston ring surfaces. Some initial work of third-body is also introduced in this thesis, along with the discussion about the future work on the third-body wear.

1.3 Scope of the thesis

The objective of this thesis is to develop a wear model for the geometrical evolution of the liner finish during the break-in period and use it to analyze the influence of different input parameters, such as pressures and liner finishes. It is also applied to investigate the functional change in ring lubrication because of wear, with different liner finishes being tested. The model is expected to provide efficient simulations to minimize testing cost through reducing the number of testing cases on tribometers.

The two-body wear model is physics-based and comprised of different submodels. In Chapter 2, the mechanism of surface plastic flattening is modeled, through a contact model involving both elasticity and plasticity and a simple asperity flattening model. Some experimental measurements are also presented in Chapter 2, providing evidence that the surface plastic deformation occurs immediately after sliding begins.

Fatigue wear is introduced in Chapter 3, starting from the theory of delamination. Two submodels are needed to complete the simulation of fatigue wear: voids initiation model and crack propagation model. Because the former largely depends on microstructures of the material, the voids initiation model of both ductile cast iron and gray cast iron is discussed. Since the surface flattening mechanism convert most of the asperities from elastic contact to plastic contact, Paris' law is utilized for the calculation of crack propagation.

Chapter 4 describes the influence of liner wear on ring-liner lubrication. Friction for the entire cycle is calculated using an existing mixed lubrication model. Different liner surface finishes are tested and also compared with experimental results.

Chapter 5 discusses the initial modeling work of third-body abrasive wear. The final chapter summaries the thesis work and suggests areas of further improvements.

Chapter 2. Surface Plastic Flattening for Contact

In this chapter, the observation and modeling of plastic deformation of a rough surface is discussed. Because for the contact pair of ring and liner, ring surface is much smoother compared with the liner surface, the deformation of liner surface is actually close to a flattening process, with a fast change for the plateau roughness. This plastic flattening process is significant especially during the first running cycles after the beginning of wear process. This flattening process is short compared with the entire running duration, but due to the change of surface topology, both solid surface contact pattern and hydrodynamic lubrication behavior are completely changed. Therefore, it is essential to consider this mechanism, and integrate it into the entire two-body break-in wear simulation.

2.1 Experiment Observation of Surface Plastic Flattening

Among all different physical wear mechanisms, three different wear mechanisms are believed to have the greatest contributions to surface topology change: surface plastic deformation, asperity fracture and abrasion [10]. Surface plastic deformation occurs throughout the entire wear process, but during the first several cycles it is the most significant. In the experiment, it is observed that the surface is plastically deformed just after 5 cycles. Due to the limitation of testing device, it is impossible to set the number of running cycles to be lower than 5. However, it is a reasonable guess that the surface experiences plastic deformation immediately after the sliding process begins.

2.1.1 Experimental setup

The set of experiments is conducted on an SRV tribometer. The SRV is a multifunctional tribometer, originally designed for evaluating the friction and wear characteristics of lubricants and materials [11]. The modular design of SRV makes it convenient for the user to change input parameters, such as external load, temperature, sliding frequency and lubricant supply rate. For the latest generation of SRV, the machine can be tilted, in order to reach a specific angle between the horizontal line and compensate the possible difference caused by gravity, compared with real wear conditions [12]. The tribometer used in this project is systematically introduced in Reference 12. In this test series, the tilted angle is 30 degrees, which meets the condition of ring liner sliding contact in most passenger cars. The tiled SRV tribometer is presented in Figure 2.1. Figure2.2 shows the detailed experimental setup in the SRV tribometer. Two testing specimens are kept in contact before the start of the experiment. The upper specimen is the ring segment, which is attached to the ring holder. The ring holder is then directly connected to the oscillation motor, providing oscillation motion for the ring segment with a constant frequency. The lower sample is the liner sample in this experiment, which is attached to the liner sample holder. The liner sample keeps still, relative to the testing space. The external load is directly applied on the upper specimen, keeping the two specimens in contact for the entire wear testing process. Figure 2.3 illustrates the assembly of the ring segment and the liner sample. Both of them have the same radius of curvature of the contact surface, in order to make it more close to the real ring-liner contact in internal combustion engines.

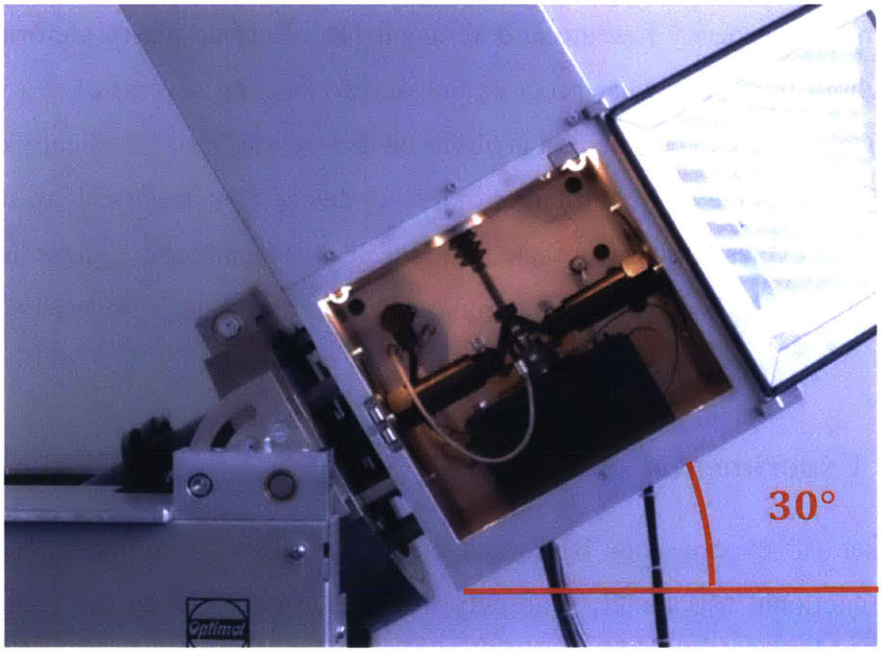

Figure 2.1 Tilted angle of the SRV

External load, oscillation frequency, temperature and oil supply rate can be manually controlled. In the set of experiments conducted in this project, only external load changes. One test is conducted under 75 Newton external load, the other is under 150 Newton. Other parameters are constants. The detailed experimental parameters are listed in Table 2.1.

In order to observe the surface topology evolution during wear process, for each external load (either 75 Newton or 150 Newton), surface roughness measurement of the liner sample is performed before testing and after 5 sliding cycles, 50 sliding cycles and 500 sliding cycles. The surface measurement device and measurement results are discussed in the next two sections.

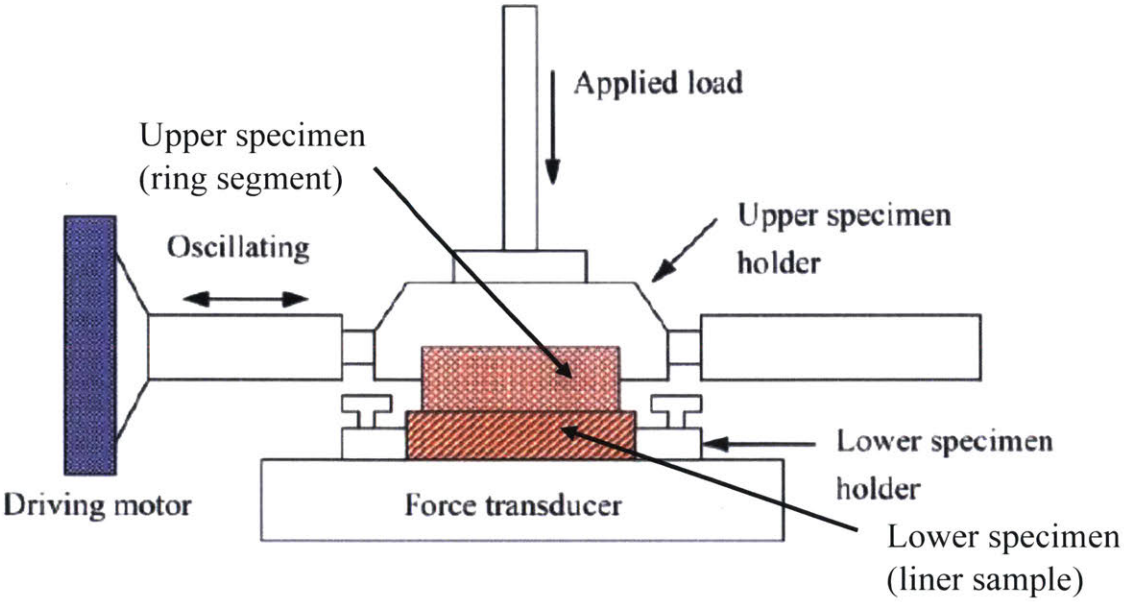

Figure 2.2 Detailed setup of wear tests in an SRV [13]

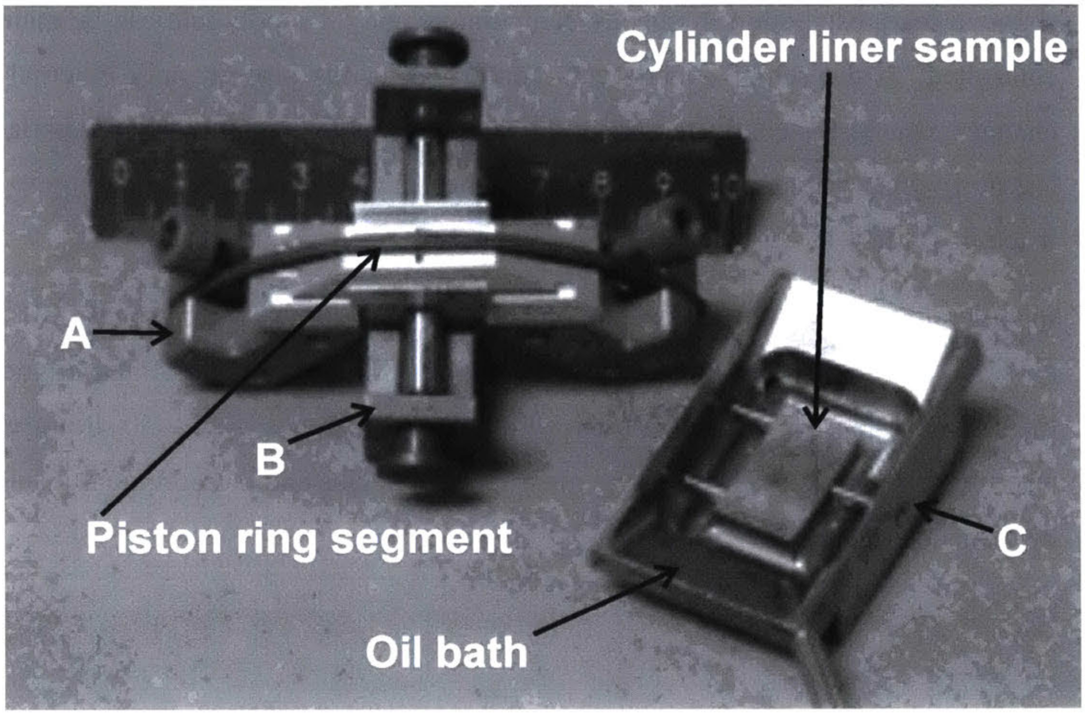

Figure 2.3 The ring segment holder and the liner sample holder [14]

controlled parameters	**value**	**units**
load	**75, 150**	**Newton**
temperature	**150**	**Celsius degree**
stroke	**3.0**	**millimeter**
oscillation frequency	**5.0**	**Hertz**
oil supply rate	**1.0**	**micro litter per minute**

Table 2.1 Experimental parameters

2.1.2 Surface roughness measurement

Confocal microscopy is a kind of surface measurement method based on optical technique. [15] Figure 2.4 shows the workflow of a confocal microscope. Laser from the laser source first goes through a pinhole, then reflects on two rotating mirrors, and finally illuminates the measured surface. The detector receives the reflected light. By analyzing the intensity of the reflected light from the measured surface, the system automatically switches the light intensity to surface height at different measure locations. The method of confocal microscopy has both its advantages and shortcomings compared with other measurement methods. Compared with methods require direct contact with the measured surface, for example stylus profiler, confocal microscopy can prevent possible damages to the measured surface caused by measurement process. [16][17] However, this method is unable to precisely measure the locations with large height gradient, usually leading to fake spikes. For a honing surface, these spikes occur mostly on the edge of valley structures. For a porous spray coated surface, locations with surface holes usually contains a lot of measurement error. Moreover, since the light received by the detector is reflected from the measured surface, oil deposits can also lead to measurement errors. In Section 1.1.3, surface measurement results using confocal microscopy method is presented, with some measurement errors can be observed. Those measurement errors do not influence us to analyze the surface plastic flattening process.

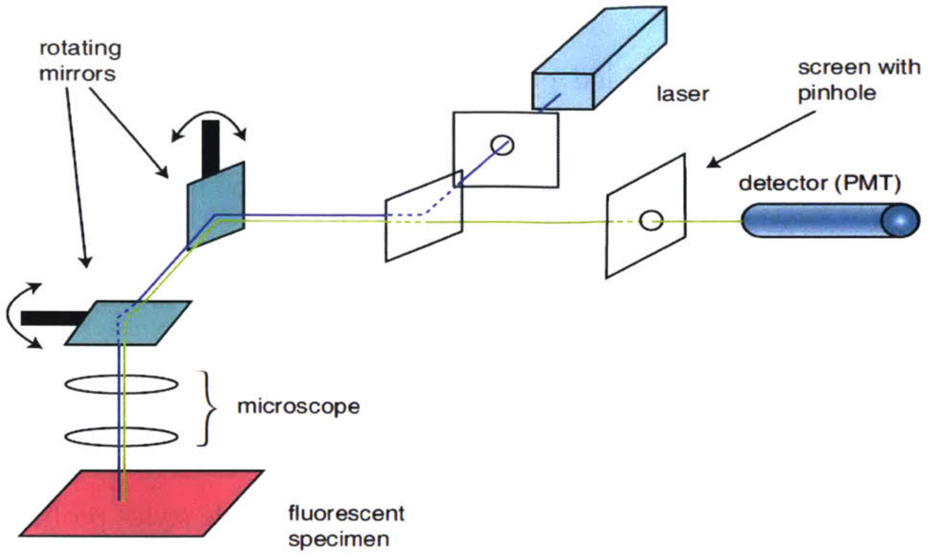

Figure 2.4 Workflow of a confocal microscope [18]

2.1.3 Experimental results

As stated in section 1.1.1, surface roughness measurement of the liner sample is performed before testing and after 5 sliding cycles, 50 sliding cycles and 500 sliding cycles. This makes it possible to observe the surface evolution and analyze wear mechanisms at a specific location.

Figure2.5 – Figure 2.8 are the surface measurement results using a confocal microscope. The four figures use the same datum plane and same height scale, making it easy to compare. As is mentioned in the previous section, measurement errors occur inevitably, leaving these regions containing no information about the surface height. Some measurement errors are identified in red circles in Figure 2.5 and Figure 2.6. The tested surface experiences significant plastic deformation, just after 5cycles, with many contact asperities being flattened. It is reasonable to conclude that the plastic flattening immediately starts from the beginning of the very first sliding process. Some small scratches are also detected on the surface of flattened asperities. Since there are no third-body particles between contact surfaces, neither soot nor wear debris, these scratches are caused by small but hard asperities on the ring segment surface. After 50

cycles, contact asperities are further flattened, with more material removed or compressed from the top of each asperity. After 500 cycles, the measurement shows the contact pattern gradually becomes stable, because the surface is close to the one after 50 cycles. Therefore, plastic flattening occurs mainly during the first several cycles, then elastic contact plays the dominant role. Although surface plastic flattening only dominates a short period compared with the rest of the wear time, it can significantly change the surface topology.

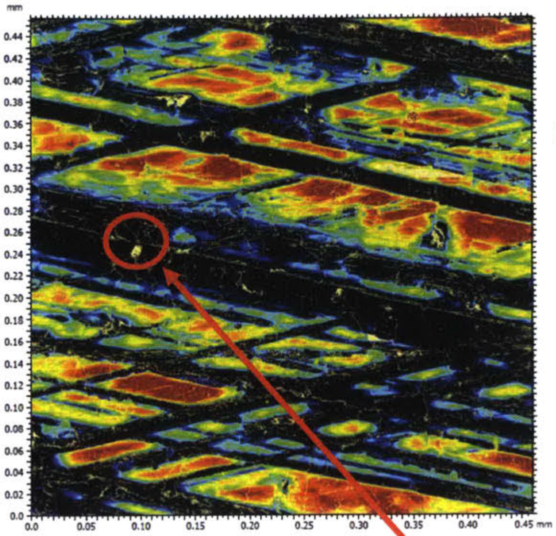

Figure 2.5 Measuredsurface before wear

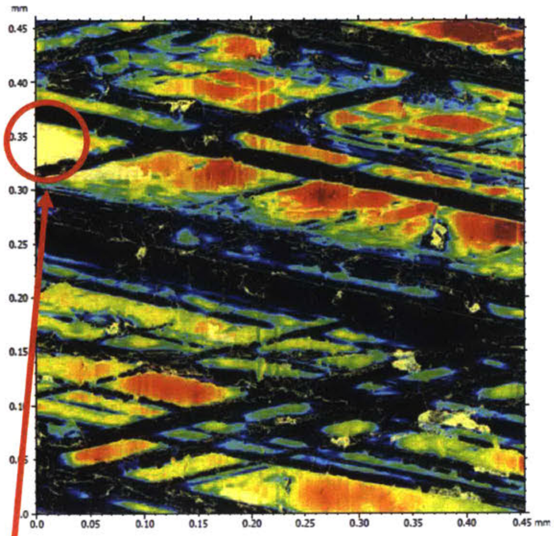

Figure 2.6 Measured surface after 5 cycles

Measurement errors

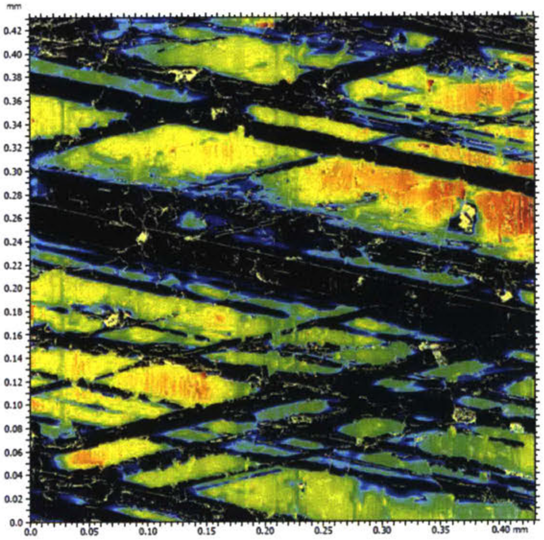

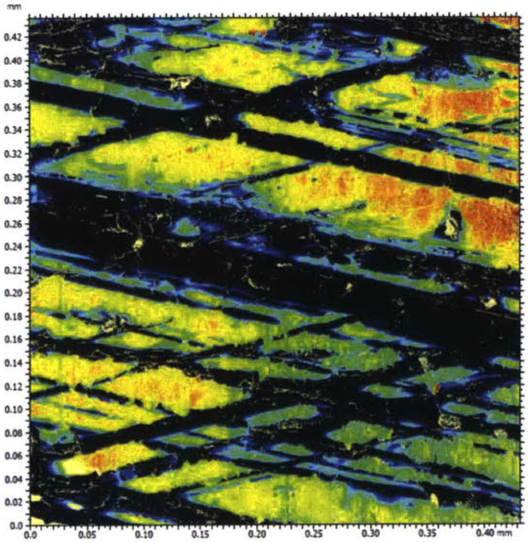

Figure 2.7 Measuredsurface after 50 cycles Figure 2.8 Measured surface after 500 cycles

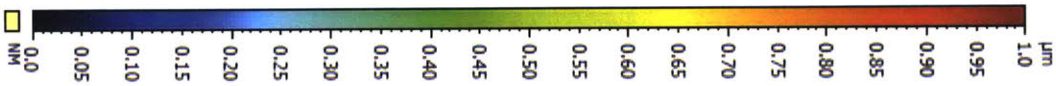

Figure 2.5 – 2.8 Surface measurement under 75 Newton external load

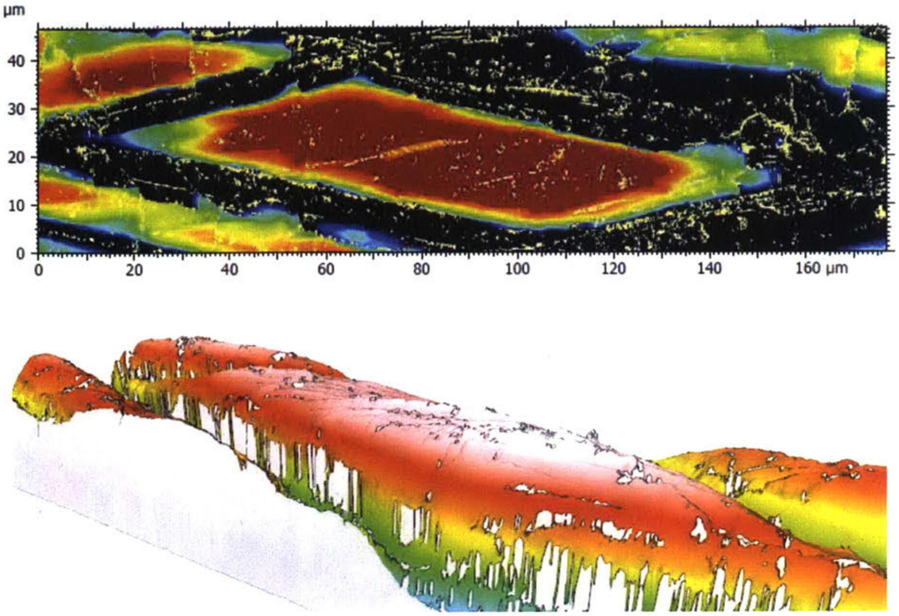

Figure 2.9 2D and 3D views of one asperity before wear

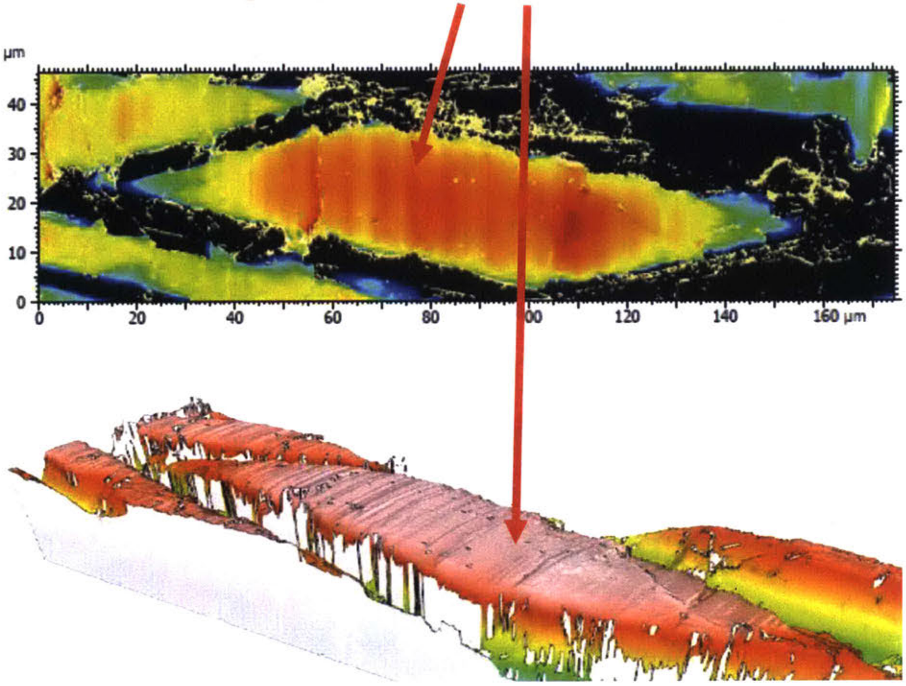
Flattened asperity and small scratches on its surface

Figure 2.10 2D and 3D views of one asperity after 5 cycles

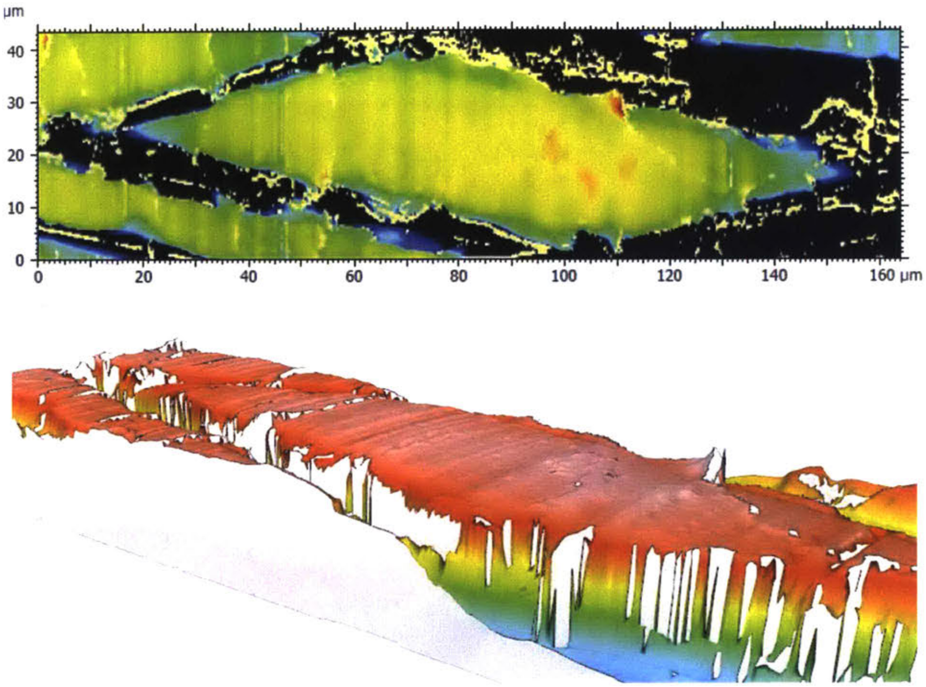

Figure 2.11 2D and 3D views of one asperity after 50 cycles

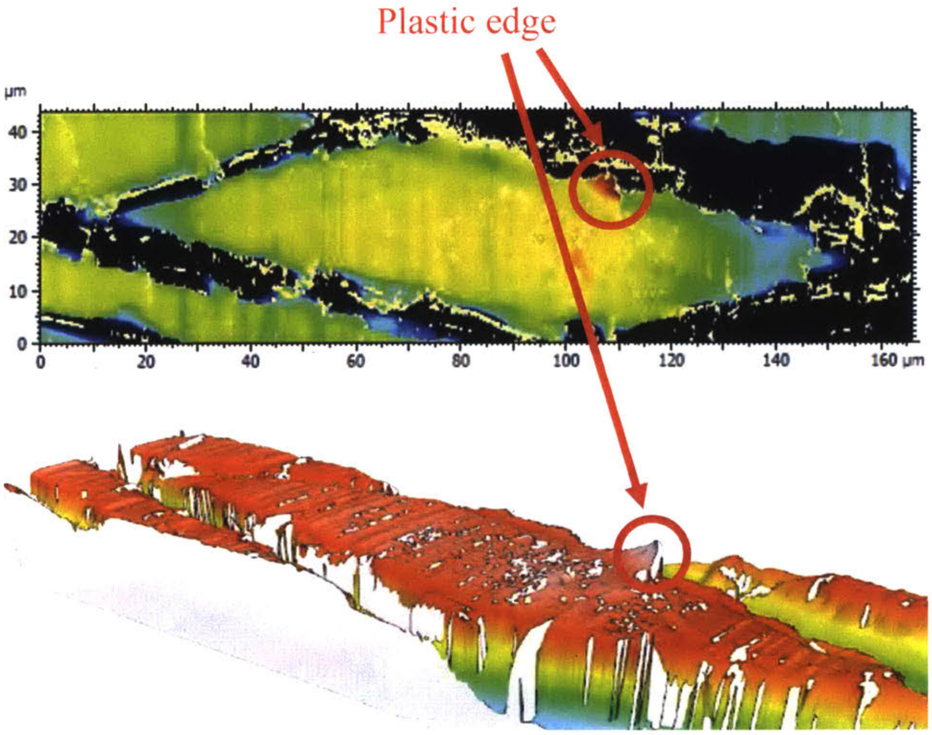

Figure 2.12 2D and 3D views of one asperity after 500 cycles

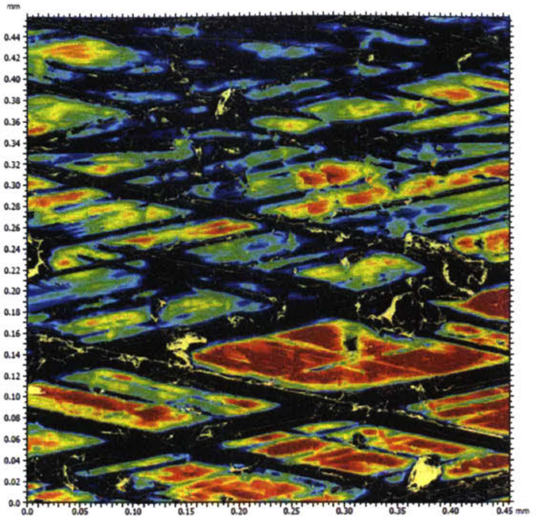

Figure 2.13 Measuredsurface before wear

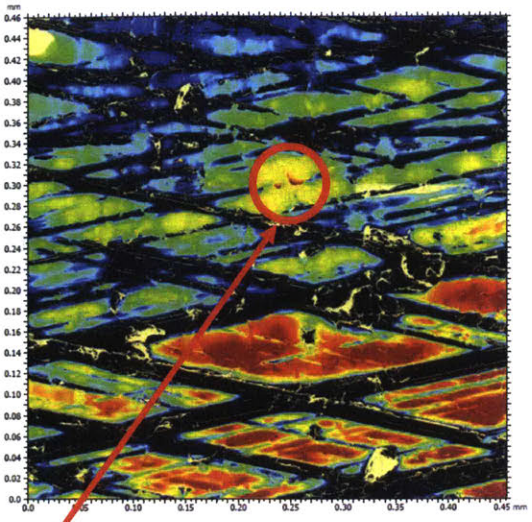

Figure 2.14 Measured surface after 5 cycles

Plastic edge covering the original grooves

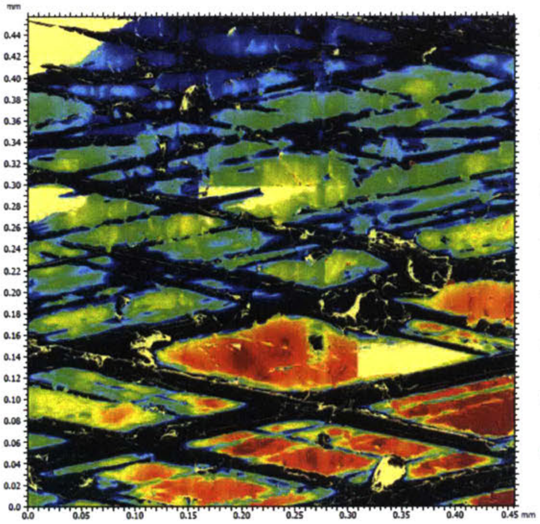

Figure 2.15 Measured surface after 5 cycles

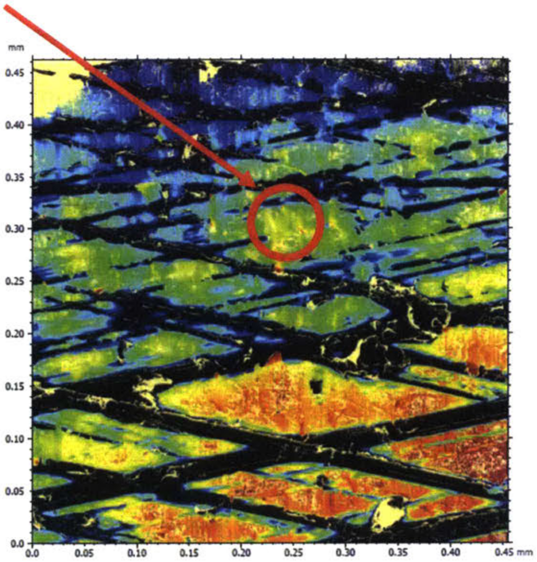

Figure 2.16 Measured surface after 500 cycles

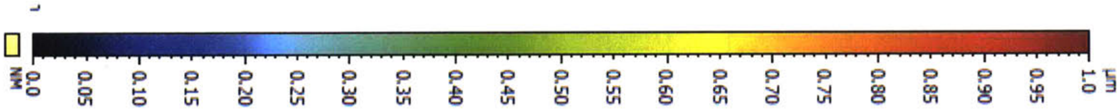

Figure 2.13 – 2.16 Surface measurement under 150 Newton external load

Figure 2.9 – Figure 2.12 reveal the change of a specific asperity. It is easy to notice the plastic flattening process from both 2D and 3D views. It is also very interesting to see the plastic edge on this asperity. This is a tail-like structure, which is mainly caused by adhesion effect between the two sliding surfaces. Since plastic edges may cover the honing grooves, they maybe have potential to cause more severe wear. This should be seriously concerned when the external load is large, because the influence of adhesion would increase under larger load. In Figure 2.13 – Figure 2.16, small honing grooves are covered by plastically deformed material. In this thesis, groove covering effect is presented here as one of the experimental observations, but not modeled in wear simulation due to its various shape and unpredictable behavior.

The surface flattening process is also quantitatively reflected from calculating the change of roughness parameters, S_k, S_{pk} and S_{vk}. In Figure 2.17, during the first 5000 cycles, S_k and S_{pk} both have decrease, indicating that the surface plateau part is flattened. Meanwhile, S_{vk} shows some small fluctuation, but keeps within a relative constant range. This meets with the initial expectation that the surface flattening process only influence the topology of the plateau part, while has little influence on the valley part, since the ring segment does not contact with grooves. Figure 2.18 is the corresponding plot when the external load increases to 150 Newton. S_k, S_{pk} and S_{vk} also show similar trend when external load is 75 Newton. Surface flattening occurs for different loads.

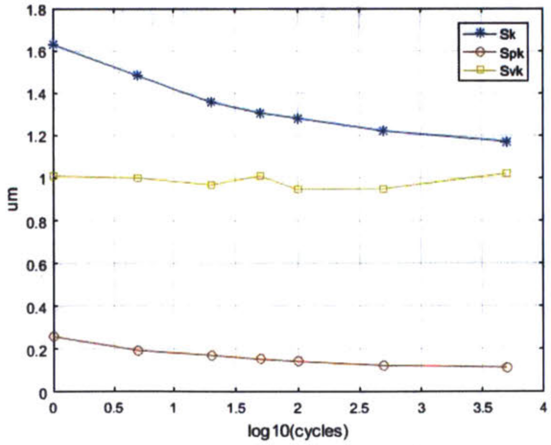

Figure 2.17 Change of roughness parameters for load 75 Newton

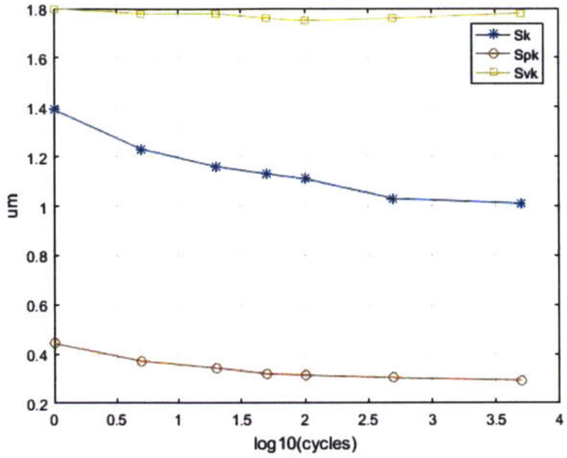

Figure 2.18 Change of roughness parameters for load 150 Newton

2.2 Surface contact modeling

In section 1.1, wear experiments indicate that a large area of liner surface experience plastic flattening, with change in surface topology. In order to simulate the plastic deformation, it requires a contact model first, which should include the effect of both elastic and plastic deformation.

As introduced in section 1.8, Chapter 1, the contact model for spherical asperities can be mathematically expressed as [19]:

$$A_c = \begin{cases} \pi R h & \text{if } h \le h_1 \\ \pi R h[1-2(\frac{h-h_1}{h_2-h_1})^3 + 3(\frac{h-h_1}{h_2-h_1})^2] & \text{if } h_1 < h \le h_2 \\ 2\pi R h & \text{if } h > h_2 \end{cases} \qquad \text{(Equation 1.1)}$$

$$P_a = \begin{cases} \frac{4E}{3\pi}(\frac{h}{R})^{1/2} & \text{if } h \le h_1 \\ H - H(1-k)\frac{\ln h_2 - \ln h}{\ln h_2 - \ln h_1} & \text{if } h_1 < h \le h_2 \\ H & \text{if } h > h_2 \end{cases} \qquad \text{(Equation 1.2)}$$

Where A_c is the real contact area, P_a is the mean contact pressure. R is the radius of the asperity tip, H is the hardness of the material, and k is the mean contact pressure factor, which represents that if the mean normal pressure P_a exceeds kH, initial yielding occurs. For cast iron, k is usually taken around 0.4. Figure 2.17 shows the asperity contact model.

The contact pattern is divided into three categories: elastic contact, elastoplastic contact and fully plastic contact. The three categories are identified by two critical penetration depth$h_1 = (\frac{3\pi kH}{4E})^2R$, $h_2 = (\frac{3\pi H}{2E})^2R$. When$h \leq h_1$, the contact is purely elastic, which is consistent with the famous Hertzian theory. The contact area is only half of the cross sectional area of an asperity in elastic range, and it increases to be the same in fully plastic range. Elastoplastic range is a transition, as in Figure 2.19

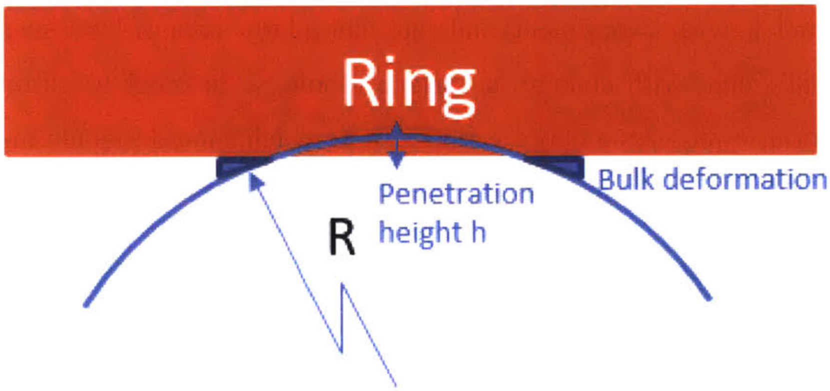

Figure 2.19 Contact model of an asperity with a spherical summit

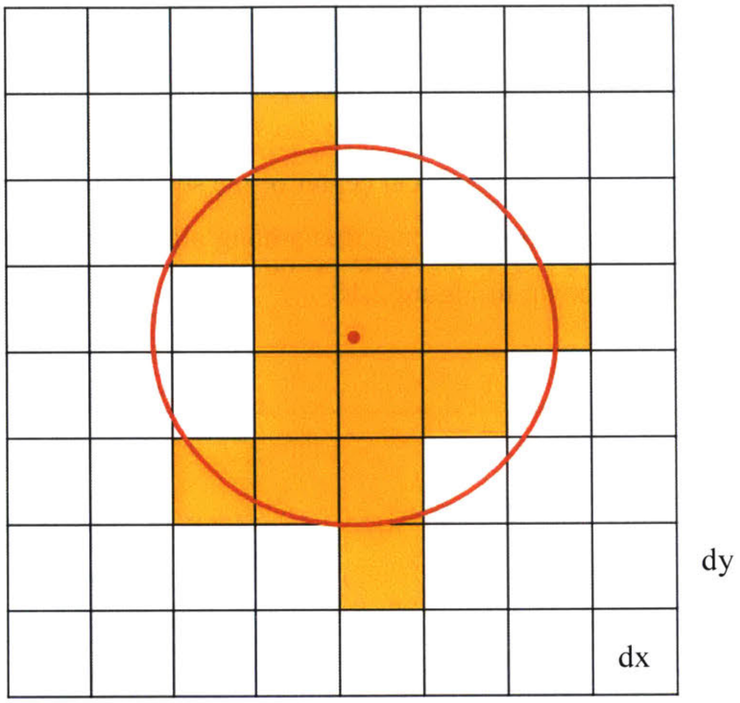

Figure 2.20 Converting to an asperity with a spherical summit

This asperity contact model is efficient under several assumptions. First, the contact occurs between a smooth surface and a rough surface, with the smooth surface considered as a rigid body. In the ring liner contact system, ring is much smoother compared with liner. In addition, the coating on the ring surface is harder than liner. Second, the interactions among asperities are neglected, so the deformation of each asperity only depends on the contact situation between the ring and its own. This assumption is sufficient for a sparse contact, with the real contact area much smaller than the nominal contact area. Third, bulk deformation is also neglected. As shown in Figure 2.17, due to deformation, some material is pushed outward from the center of an asperity. This deformation is called bulk deformation, which is not included in this model.

The final assumption is that all asperities need to be considered having spherical summits, in order to perform the calculation. However, the liner surface is represented as a matrix, containing each element reflecting the height of an area of 1.122μm ×

1.122µm. Due to the resolution of confocal microscopy method, one asperity consists many adjacent small squares in a matrix representation. To convert it into an equivalent spherical asperity, a circle is created with the same area as the sum of all squares in that asperity, centered in the geometrical center of the squares set. The penetration depth is taken as the maximum penetration value among all matrix elements in that asperity. This conversion is shown in Figure 2.18

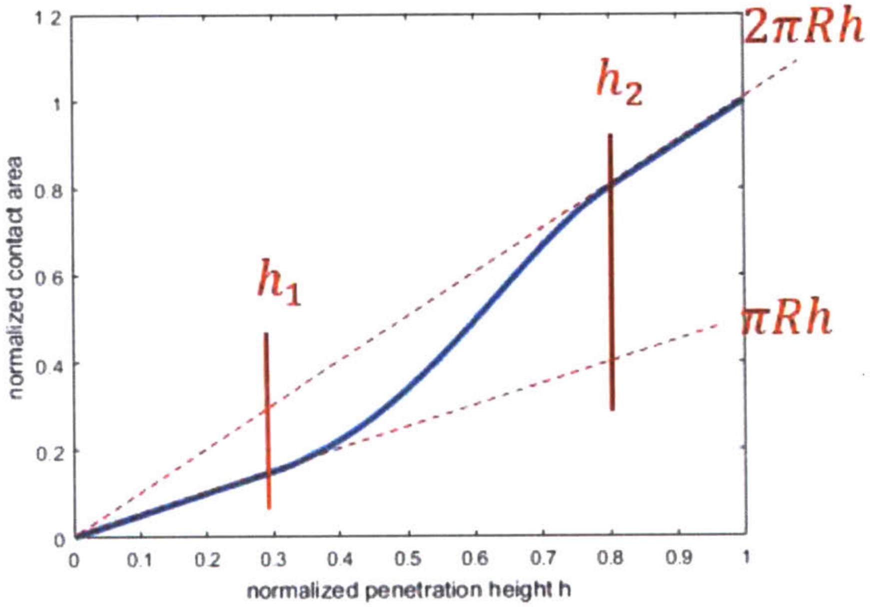

Figure 2.21 Normalized real contact area

With all assumptions and classifications, an asperity contact model is introduced into liner simulation. The model is able to identify plastic deformation in different plastic ranges, making it efficient to simulation the plastic flattening on the liner surface.

2.3 Modeling of asperity flattening

The detailed asperity plastic deformation is very complicated. Due to different shapes, contact pressures, contacting angles, all asperities on the liner surface can have various plastic deformation patterns. However, calculating the deformation for each asperity is not feasible since there are thousands of them contacting with the ring at the same time.

The calculation amount would be too large. Instead of trying to get specific solution for each asperity, an efficient wear model should adopt a relatively universal method to perform asperity deformation analysis over the entire simulating surface. As introduced in Chapter 1, asperity plastic deformation is modeled as plastic flattening with an elastic spring back [20]. If one asperity contacts elastically with the ring, it only experiences elastic deformation when the contact is happening, and it will immediately recover from the deformation once the contact ends. While if the contact deformation involves plasticity, the asperity will never get back to its original shape, but only has a small spring back. Figure 2.22 and Figure 2.23 show the shape of a spherical asperity after elastic contact and plastic contact, respectively. The amount of elastic spring back at the center of the contact asperity is given by KL Johnson [21]:

$$u_{el} = 2(1 - v^2)\frac{H}{E}\sqrt{\frac{A_c}{\pi}} \qquad \text{(Equation 1.3)}$$

Where v is the Poisson ratio, H is the material hardness, E is the elastic modulus, and A_c is the real contact area, calculated from Equation 1.1. Once the contact is beyond the Hertzain range, identified by the penetration depth$h > h_1 = (\frac{3\pi kH}{4E})^2$, this elastic spring back is used to simulate the asperity height after surface flattening. Because of the existence of spring back on each asperity contact plastically, asperities are not completely flattened. This can be revealed from the distribution of asperity height. In Figure 2.24, if the original asperity height distribution is Gaussian, then the distribution still has a right tail after the sliding process, as shown in Figure 2.25. In section 1.4, distribution changes for different surfaces are plotted, with results showing surface plastic flattening happens for all surfaces, especially at the beginning of wear.

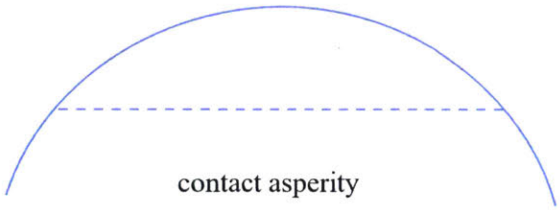

Figure 2.22 Elastic contact

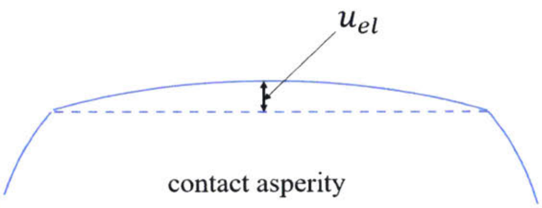

Figure 2.23 Plastic contact

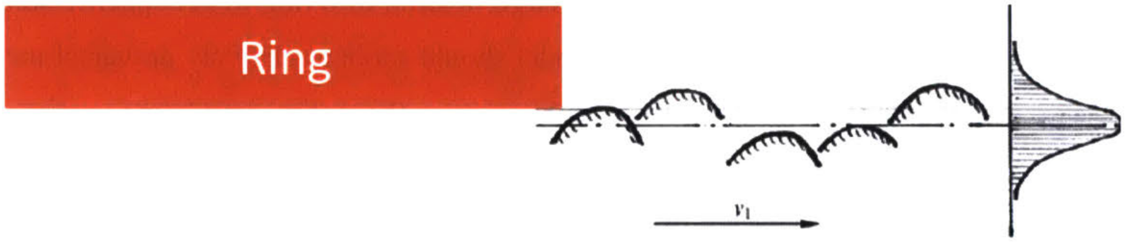

Figure 2.24 Distribution of asperity height before surface flattening

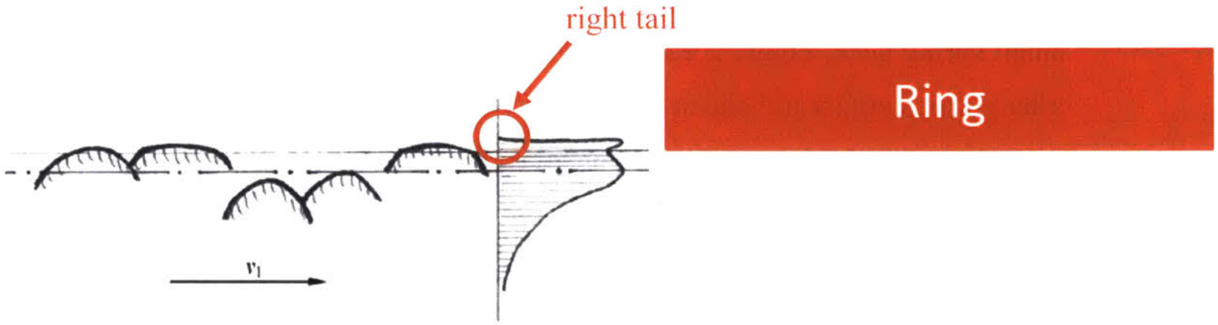

Figure 2.25 Distribution of asperity height after surface flattening

2.4 Simulation results for surface plastic flattening

Because the surface plastic deformation process is essentially important for surface topology change, simulations are conducted based on the previous theories for 5 different liner surface finishes: GG07, GG09, GG21, GG28 and GG30. The classification of different liner surface finishes is summaried in Figure 2.26. These liners are made of grey cast iron, and are classified according to structure height and plateau character, with smoother ones located on the left of the figure [22].

A good way to show the flattening effect is plotting the evolution of surface height distribution. Significant change can be observed from the height distribution curve, especially for its right tail because it represents the very top layer of the surface.

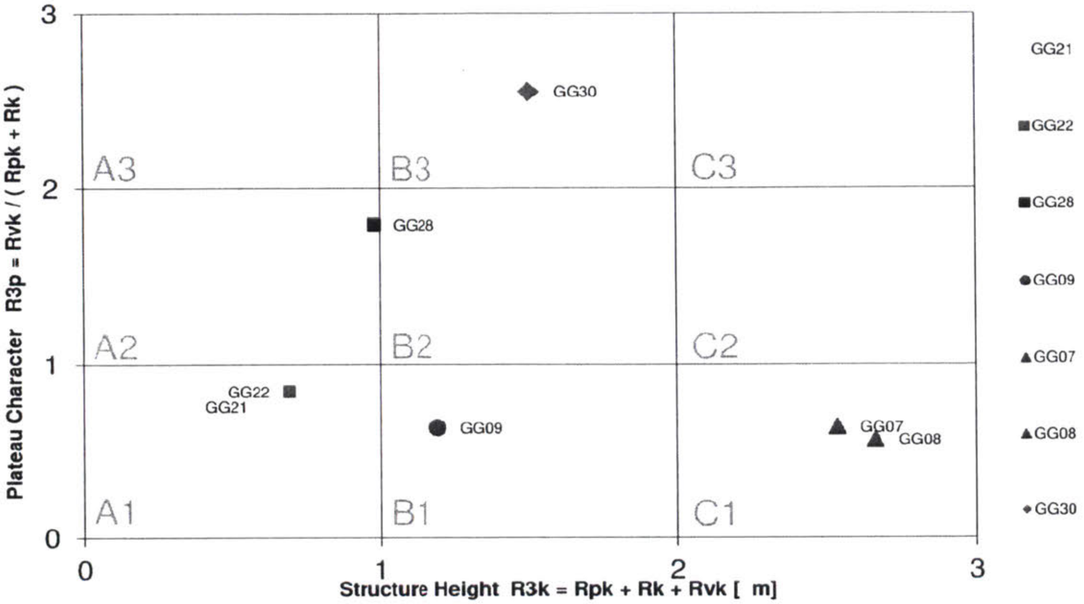

Figure 2.26 Roughness of liners used in wear simulations [22][23]

Figure 2.27 shows the height distribution change of GG30 during the first 20 cycles of wear process. The external normal pressure is set as a constant value, 2MPa. Initially, the surface height distribution curve has a smooth right tail, indicating that the surface is well finished before the wear process. Later, the occurrence of a peak reveals that the surface is flattened since heights of many asperities are gradually concentrated with a small range. Another important evidence is that this peak caused by surface plastic flattening actually moves to the left as the number of running cycles increases, which is clearly shown in Figure 2.28. This evidence reflects that the piston ring height reduces after each flattening to keep the total contact force as a constant, so that the height of plastic flattening process also decreases with time.

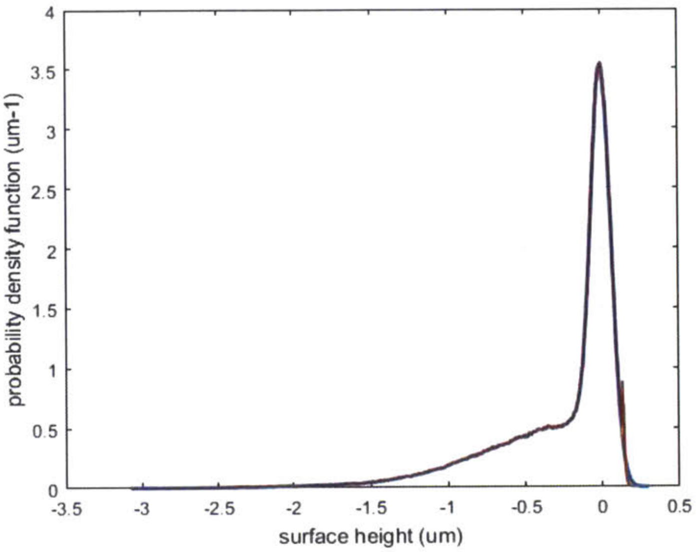

Figure 2.27 Height distribution change of GG30

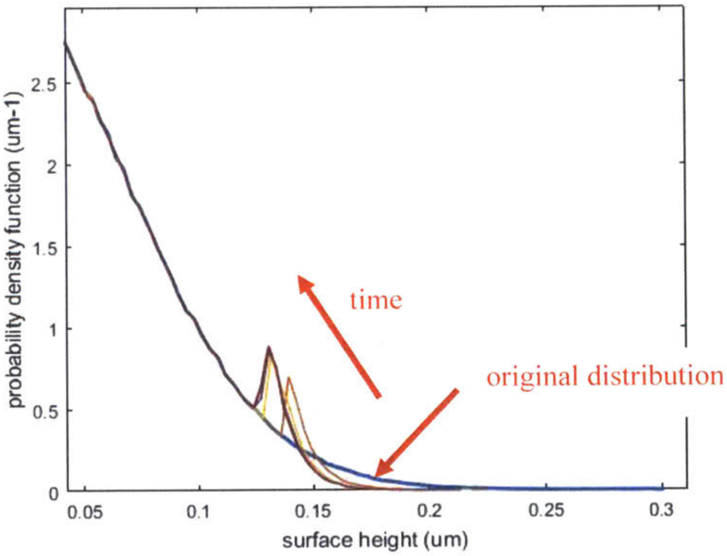

Figure 2.28 The right tail of height distribution change of GG30

It is also interesting to investigate the ratio of plastic contact among all asperities. Figure 2.29 shows the ratio of plastic contact for different external pressures and its change during the beginning of wear. When the wear process is about to start, up to 90% of the contact asperities are plastically deformed, which means the contact pressure is different from the result of Greenwood-Tripp calculation [24]. During the first several sliding cycles, the plastic contact ratio greatly decreases to a low level, less than 10%. Therefore, the beginning period is important for liner surface topology change, because it makes most of the asperities more flattened and converts many asperities from plastic contact to elastic contact. Since the dominant mechanism for the next stage of two-body wear is fatigue, this indicates that during fatigue growing process the contact condition of each specific asperity is relatively elastically stable. This makes the fatigue wear calculation more convenient, which will be discussed in Chapter 3.

As plotted in Figure 2.30 to Figure 2.37, surface height distributions and plastic contact ratios of GG07, GG009, GG21 and GG28 show similar trends with the plots of GG30. The surface plastic flattening process is essential for all different liner finishes.

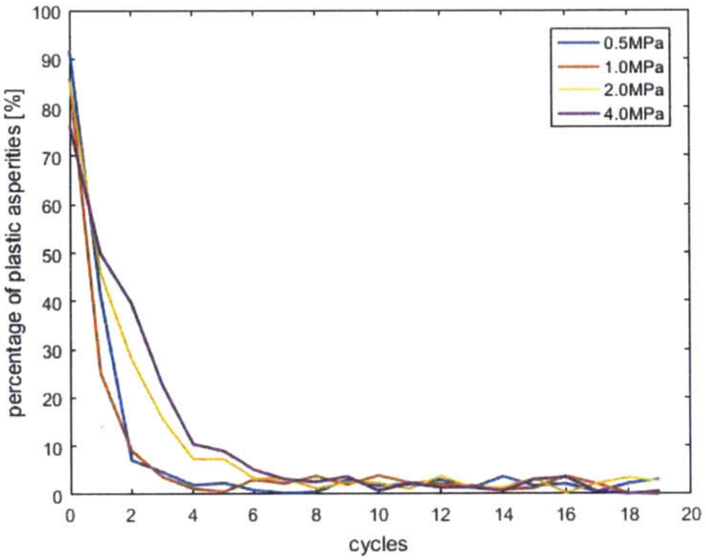

Figure 2.29 Percentage of asperities contacting plastically for GG30

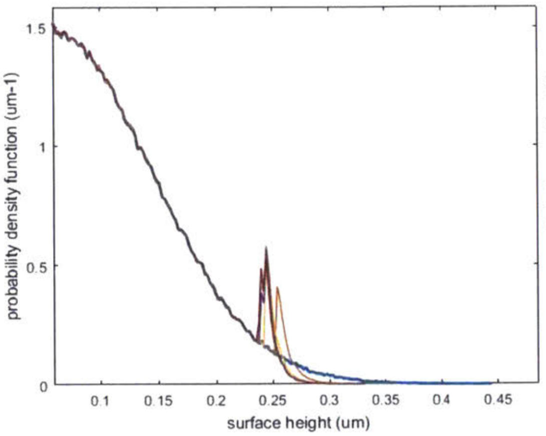

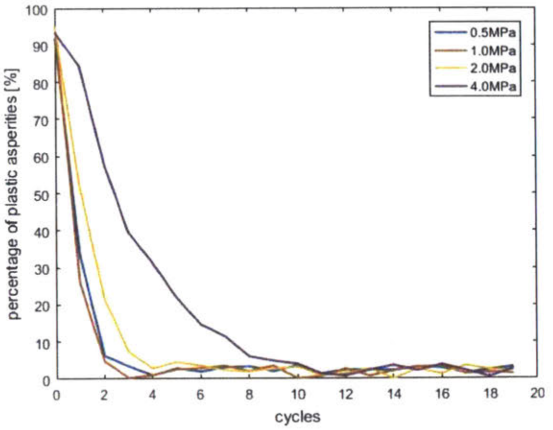

Figure 2.30 Height distribution of GG07 Figure 2.31 Plastic contact ratio of GG07

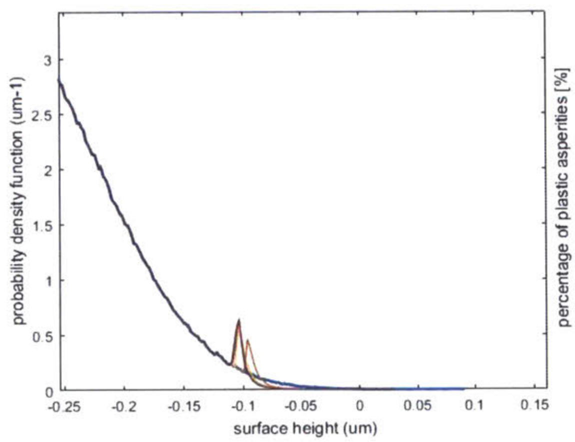

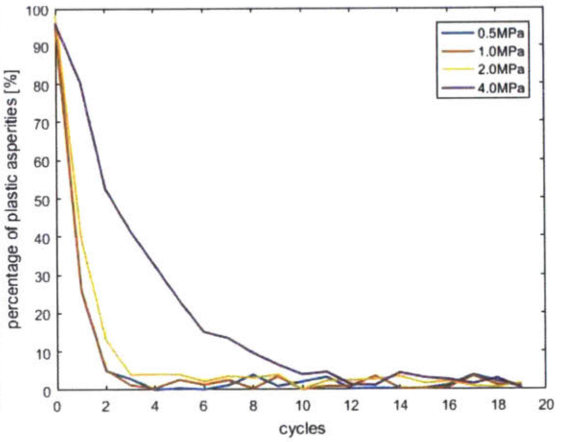

Figure 2.32 Height distribution of GG07 Figure 2.33 Plastic contact ratio of GG07

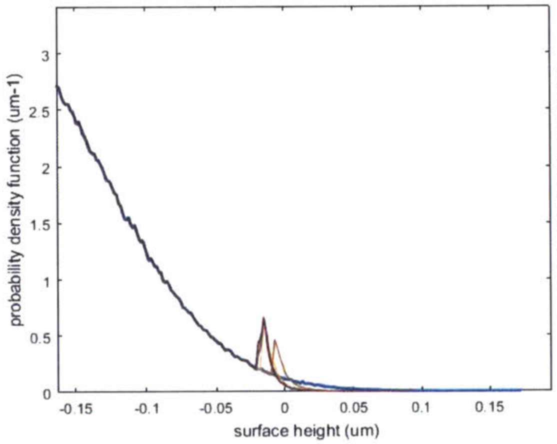

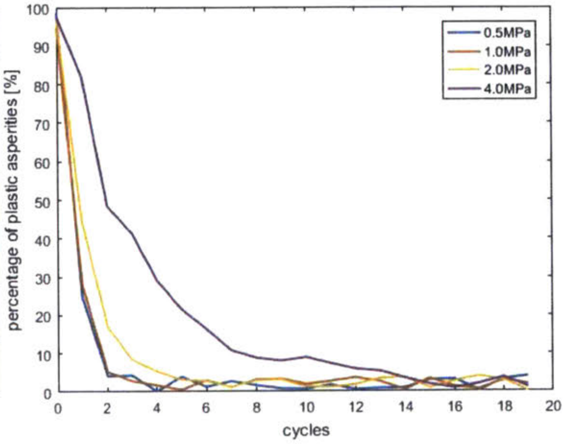

Figure 2.34 Height distribution of GG21 Figure 2.35 Plastic contact ratio of GG21

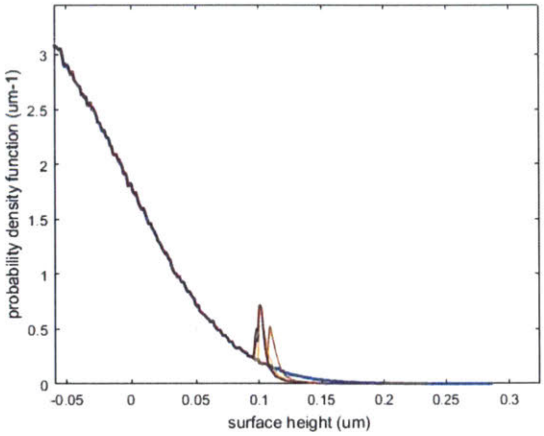

Figure 2.36 Height distribution of GG28

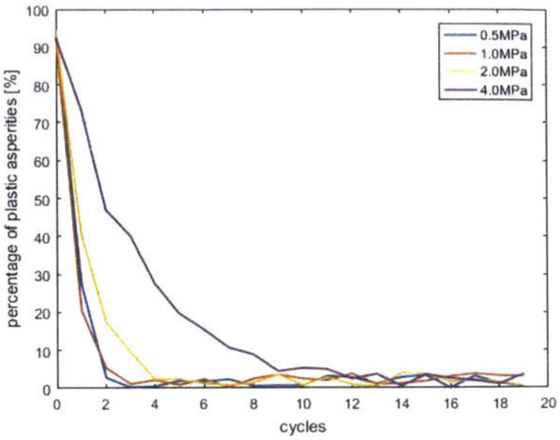

Figure 2.37 Plastic contact ratio of GG28

Conclusion

Surface plastic flattening is one of the most essential mechanism for two-body wear, resulting significant change of the original surface topology. Flattening mechanism has its influence throughout the entire wear process, but the influence is especially obvious during the beginning period of wear. Asperities contacting plastically with the ring are flattened, so as to reach an elastic contact condition. Although the plastic contact ratio is greatest reduced after several cycles, the plastic ratio never reaches zero. Therefore, the contact model used in the simulation includes elastic, elastoplastic and fully plastic contact conditions. From the plots of surface height distribution changes and plastic ratio changes for the beginning wear period of different liner finishes, it can be concluded that the plastic flattening mechanism is the dominant mechanism for the change of topology of a rough surface at the early stage of wear.

Chapter3. Delamination Theory and Fatigue Wear

In this chapter, a very important wear theory is applied: delamination theory. A two-body fatigue wear model is developed based on the delamination theory, with the focus on delamination of contact asperities on rough surfaces. Wear of metals is a complicated problem, because many different mechanisms and processes, from physical to chemical. The delamination theory proposed by Suh, systematically models the change at the subsurface level of contact, and its influence on the surface topology [25]. The direct related wear mechanism to delamination is fatigue wear. A model is developed and introduced in this chapter, based on fatigue wear mechanism, delamination theory and plastic flattening of the contact surface. The wear model is applied to surfaces with different roughness values, showing that the results of the model meet with the famous Archard's Law.

3.1 Delamination wear theory

Wear mechanisms can be roughly divided into two groups: chemical mechanisms and mechanical mechanisms. Among all mechanical mechanisms, surface plastic deformation, fatigue wear and abrasive wear are the most important three leading to surface topology change. Deamination theory is a theory which takes the fatigue part as the core mechanism in the wear process. It is widely supported by evidence for wear of metals and some other solid materials [25].

In delamination theory, wear starts with asperity deformation and fracture due to surface contact under a certain external load. This process starts immediately after contact begins, gradually switching plastic contact into elastic contact. The background and modeling results are shown in the previous chapter.

Meanwhile, the delamination process also begins at the subsurface of the contact material. It is essential to point out that the delamination process includes not only crack propagation and fracture of surface material, but also void initiation. Void initiation models are introduced in Section 3.2 and 3.3. For any multiphase material, external stress can cause tensions at the boundary of different phases, with material voids generated if boundary tensions are large enough and the boundary is under accumulation of plastic deformation.

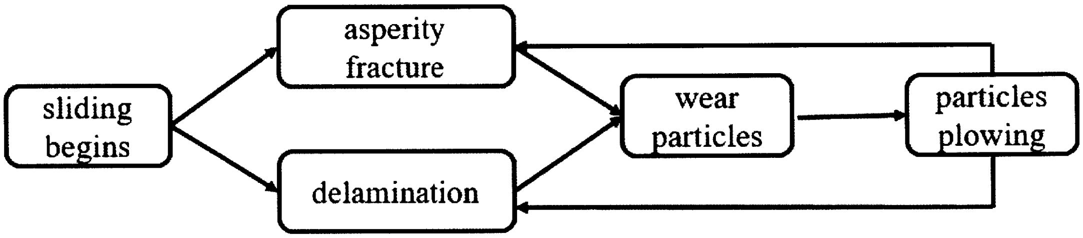

Figure 3.1 Flow chart of wear mechanisms in delamination theory

After voids are generated, cracks at the subsurface start to propagate under cyclic loading from these generated voids. In fact, original material flaws can also be starting points of cracks in most conditions, unless the material is perfectly manufactured and flaw-free. Then a crack stops propagating if it reaches the edge of the contact region, and a wear particle is detached from the original surface. The subsurface below the fatigue crack now becomes the new contact surface, so the next delamination process starts on this new surface.

Detached worn materials are trapped between two sliding surfaces, becoming third-body wear particles and causing more severe wear. The shape of these particles are various, but some correlations with the roughness of contact surface and material properties can be found. Figure 3.2 shows a sliding pair with one smooth surface and the other roughness. The contact area is the same for both surfaces at a specific epoch, but the subsurface region influenced by the contact are different. For the smooth surface, most of the subsurface experiences the loading, but for the rough surface, only regions under asperities are affected by this sliding process. Therefore, it is important to point out that the worn particles from the rough part have small aspect ratio, while worn particles detached from the smooth surface have very large aspect ratio, which means they are sheet-like. Another factor to influence worn particle shapes is the material brittleness. As shown in Figure 3.3, worn particles from brittle material are not likely to change shapes in further sliding process, but particles with a ductile material are easier to be compressed, reshaped between sliding surfaces and finally obtain small aspect ratios. In the liner ring contact system, ring surface is smooth and hard, but liner is rough. The liner surface contacts to the ring only with its asperities on the top surface, so the subsurface region with fatigue wear only limited to region under contact liner asperities. The worn particles from the liner are round shaped.

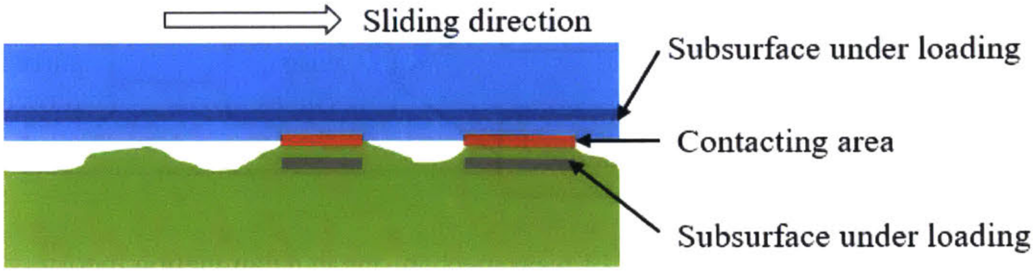

Figure 3.2 Sliding of a smooth surface over a rough surface

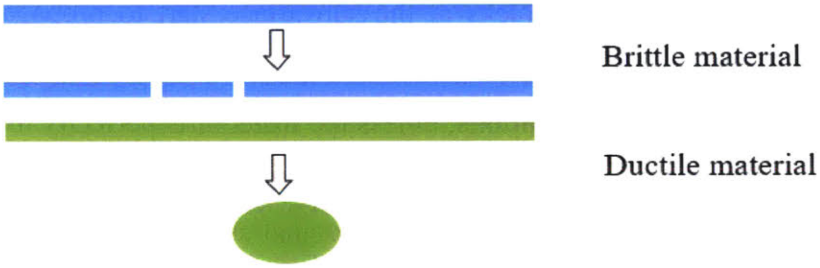

Figure 3.3 Worn particle from a brittle material and ductile material

With the existence of third-body worn particles, third-body wear is introduced. These particles can cause wear through cutting, pitting and plowing the original surfaces based on their sizes, shapes and different movement patterns [26][27][28]. Some initial work of third-body abrasive wear simulation is presented in Chapter 5, under the assumption that the worn particles are spheres.

3.2 Nucleation of material voids under contact asperities

In this section, the nucleation of material voids is discussed and modeled. Since the process of material voids nucleation is directly related to the microstructures of materials, two materials with completely different microstructures are taken into consideration. The important parameter in wear simulation is the depth of voids. Ductile cast iron and gray cast iron are the two materials in simulation, with their void nucleation depths are calculated respectively.

3.2.1 Nucleation of voids for ductile cast iron and some types of steel

Material under the contact area experience plastic deformation and has potential to initiate voids. Voids are likely to occur at the boundaries of different material phases, because each phase has its own elastic and plastic parameters. When they are under the same stress field together, the inconsistence of deformation causes boundary tension. This can be clearly illustrated in Figure 3.4. The material matric contains another material phase, represented by a circle in the center. Then after deformation of the entire material matrix, both two phases are stretched in some directions, with the generation of stresses σ_{rr}normal to the phase boundary. On side A of the boundary,$(\sigma_{rr})_A < 0$, which is a compressive stress. On side B, the boundary stress is tensile, with$(\sigma_{rr})_B > 0$.

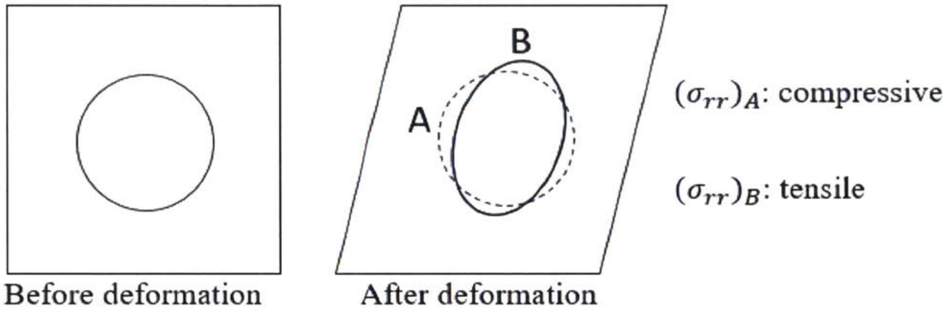

Figure 3.4 Deformation inconsistence and phase boundary tension

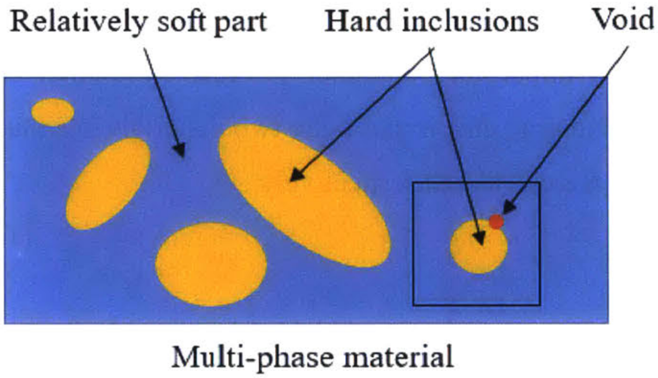

Figure 3.5 Materials modeled as two-phased with

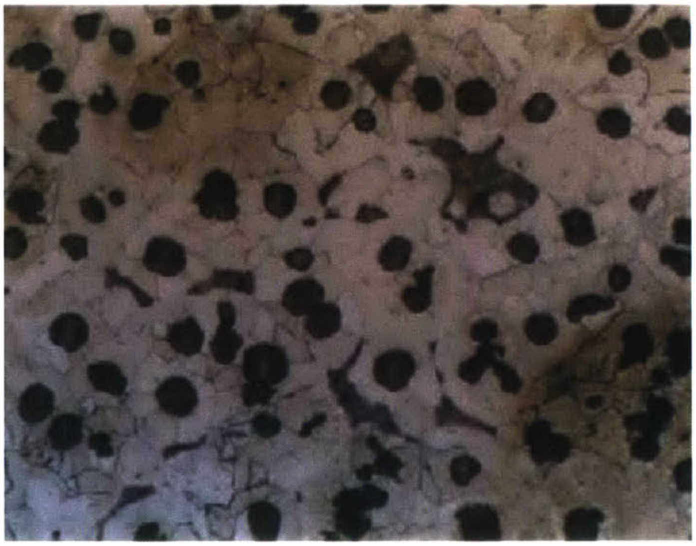

Figure 3.6 Microstructure of nodular cast iron [29]

In some steel and ductile cast iron, the material can be modeled as two-phased, with hard inclusions and other relatively soft parts, as shown in Figure 3.5. Figure 3.6 shows the microstructure of nodular cast iron, which is a typical type of ductile cast iron. It is possible to give the analytical expression for phase boundary tension, under the assumption of cylindrical and rigid inclusions [30]:

$$(\sigma_{rr})_{max} = \sqrt{3}ksin2\theta + \sqrt{3}\tau_{max}\sin2(\theta - \varphi) + \sigma_h \qquad \text{(Equation 3.1)}$$

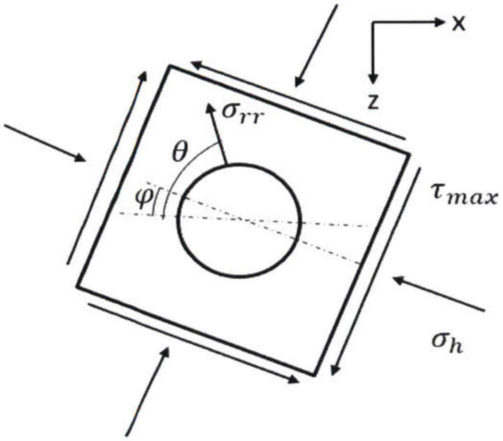

Figure 3.7 A cylindrical inclusion under stress [30]

This equation describes the boundary stress for an inclusion at a specific location, identified by coordinate (x, y, z). Where $(\sigma_{rr})_{max}$ is the maximum tensile stress on the boundary, k is the yield strength in shear, τ_{max} is the maximum shear stress at that location, and σ_h is the corresponding hydrostatic pressure. φ and θ are two angular parameters. Figure 3.7 illustrates all parameters in Equation 3.1.

In order to calculate the maximum boundary stress under different external normal stress using Equation 3.1, finite element method is used. Since the material hard inclusions are small and almost uniformly distributed, it is assumed that the material is homogenous. ABAQUS is used to perform the finite element analysis (FEA) for the stress field under a contact asperity.

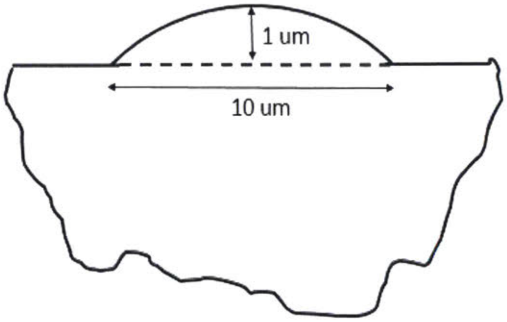

Figure 3.8 Size of the simulated asperity

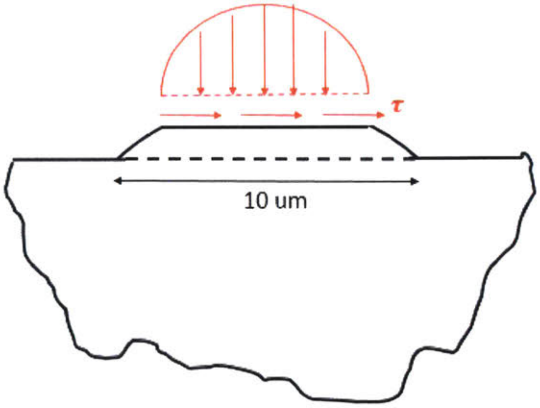

Figure 3.9 External stress for FEA

The setup of the finite element simulation is designed to meet the stress condition of one surface asperity. Because of surface honing, asperities on the liner surface are like flat bumps. In addition, the void nucleation depth is scaled to the radius of the contact region, so the simulation result is independent of body size. Therefore, the height and width are set as 1 micrometer and 10 micrometers, respectively. And this size is used for all cases with different normal pressures, as shown in Figure 3.8.

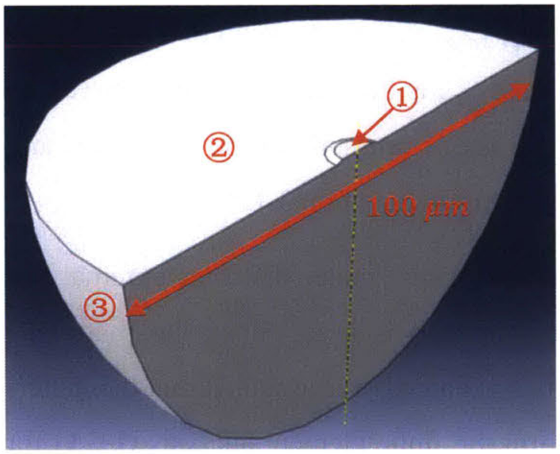

Figure 3.10 Semi-infinite body

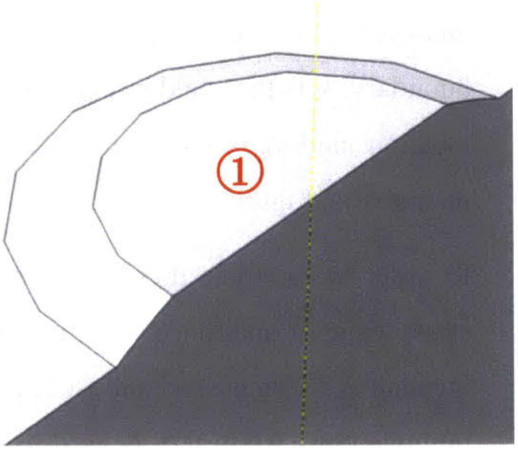

Figure 3.11 Asperity with a flattened top after loading

The asperity is rigidly attached to a large bulk of base material, with a diameter of 100 micrometers. The goal of introducing this large base is to balance out the boundary effect, and simulate the stress condition of an isolated asperity. The boundary condition is fixing the outer surface ③ in Figure 3.10, leaving other surfaces free to deform. Because the base is large enough, the boundary effect of this fixed surface on the stress field under the asperity can be neglected. The two external stresses are all assigned on the top surface ① of the asperity. One is the normal stressσ_n, increasing from 20 MPa to 720MPa, which is the possible range of normal stress for steel. The other is the shear stressσ_s, also assigned on surface ①, with magnitude$\sigma_s = 0.2\sigma_n$, indicating that the average friction coefficient is 0.2 for all asperities.

The mesh element is C3D8R, a kind of three-dimensional hexahedral element in ABAQUS. Each C3D8R element contains 8 nodes. The calculation is performed explicitly under static condition. The meshing is shown in Figure 3.12, with 14136 elements in total.

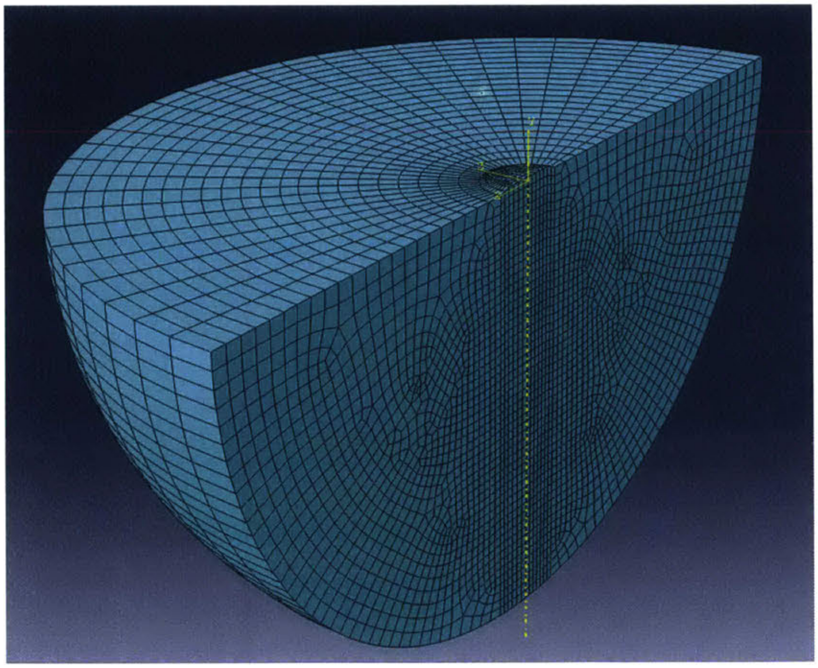

Figure 3.12 Meshing in ABAQUS

Figure 3.13 to 3.18 show Von Mises stress and the maximum boundary tensile stress σ_{rr} under different load conditions with external normal stress 80MPa, 400MPa and 720MPa. σ_{rr} is calculate using Equation 3.1, and Von Mises stress $\sigma_v$is defined as:

$$\sigma_v = \sqrt{\frac{1}{2}[(\sigma_{11} - \sigma_{22})^2 + (\sigma_{11} - \sigma_{33})^2 + (\sigma_{22} - \sigma_{33})^2 + 6({\sigma_{12}}^2 + {\sigma_{13}}^2 + {\sigma_{23}}^2)]}$$

Where σ_{11}, σ_{22}, σ_{33}, σ_{12}, σ_{13} and σ_{23} are the 6 components of the stress tensor. Von Mises stress is usually applied to define the plasticity. Once the Von Mises stress exceeds the material yielding stress σ_y, that region is plastically deformed.

80MPa, 400MPa and 720MPa are three examples of all different normal stresses, with each one representing a typical category in the FEA results.

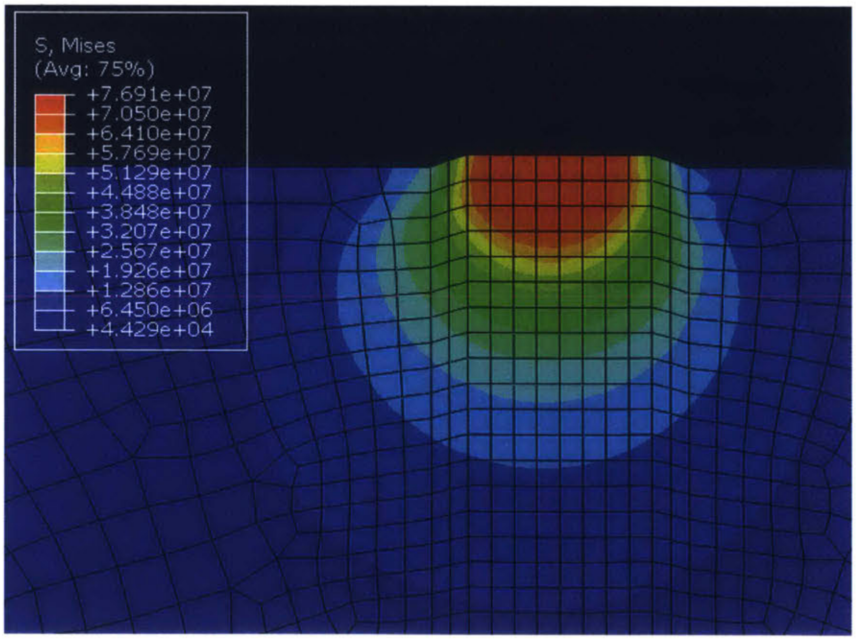

Figure 3.13 σ_v under normal stress 80MPa

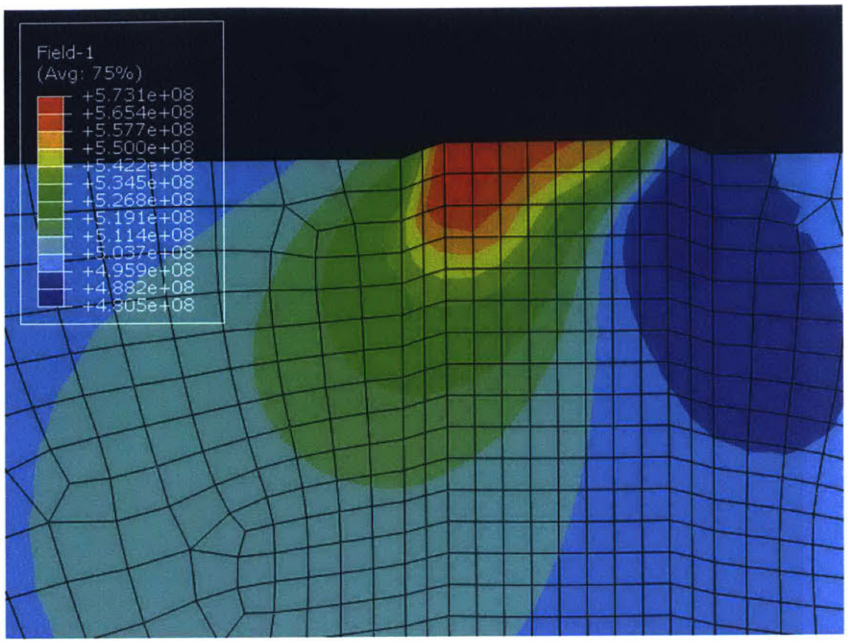

Figure 3.14 σ_{rr} under normal stress of 80MPa

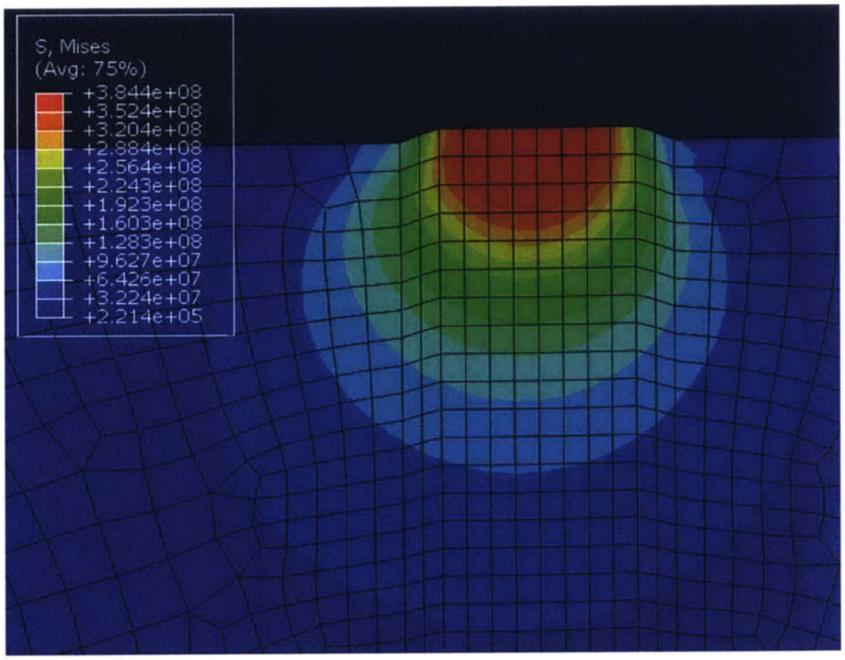

Figure 3.15 σ_v under normal stress 400MPa

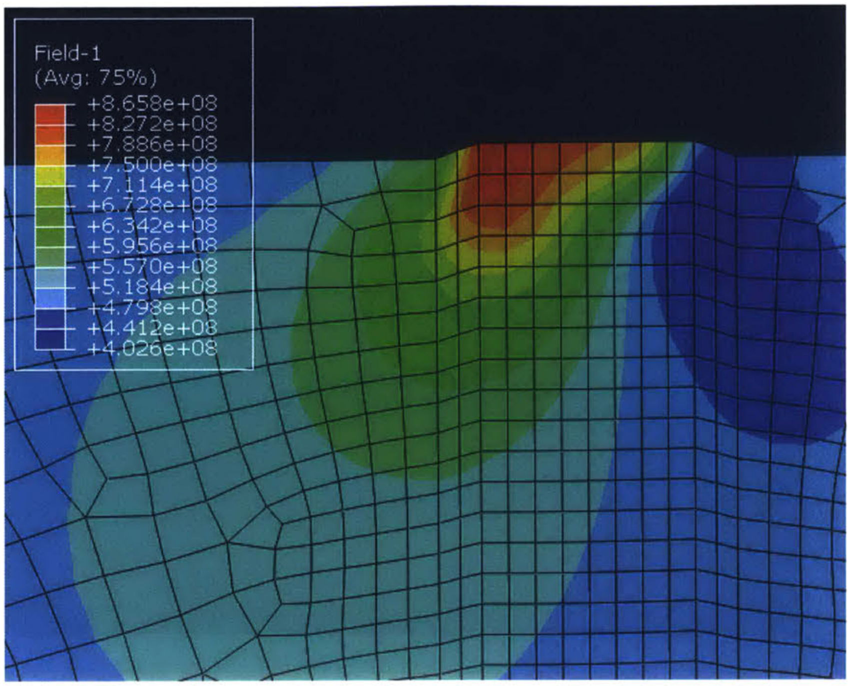

Figure 3.16 σ_{rr} under normal stress 400MPa

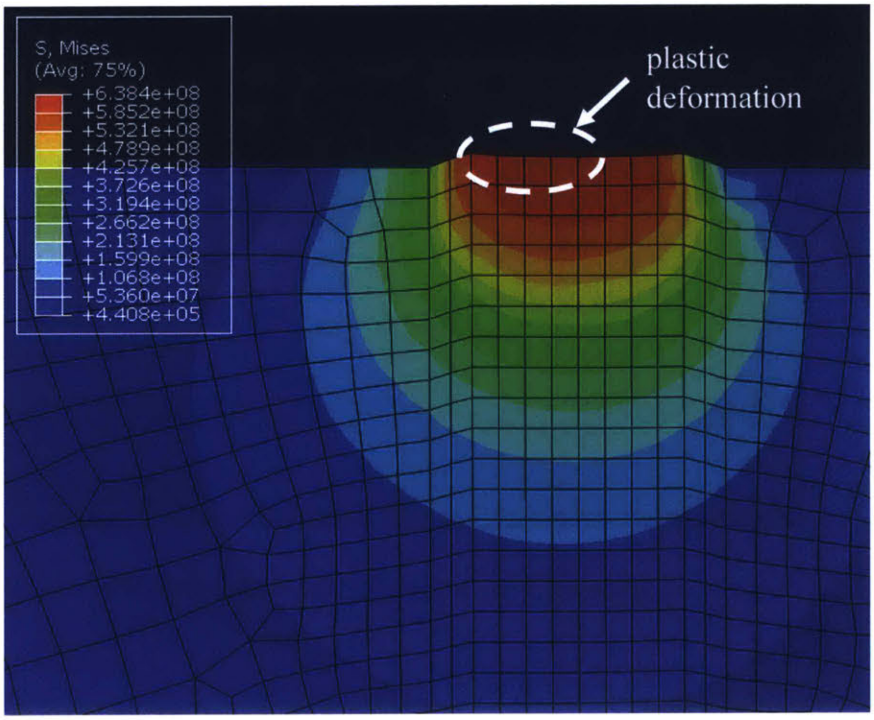

Figure 3.17 σ_v under normal stress 720MPa

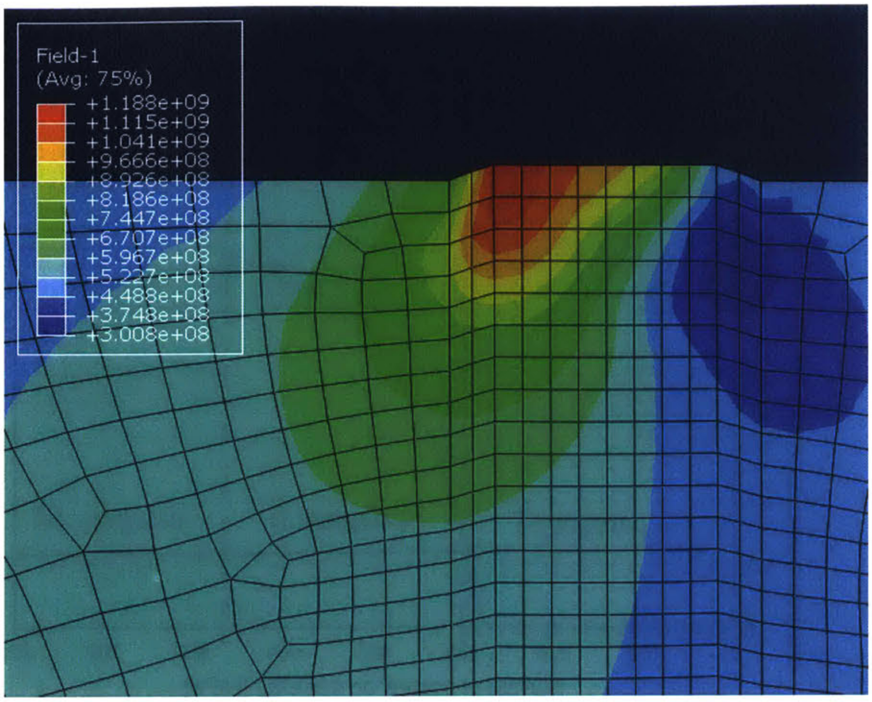

Figure 3.18 σ_{rr} under normal stress 720MPa

When normal pressure is 80 MPa, the maximum value of Von Mises stress is smaller than yielding stress σ_y (500 MPa for steel), indicating that the deformation is completely elastic. And because the maximum boundary tension stress is smaller than the critical phase bonding strength, no void would be generated under this loading condition. This is the first category: elastic deformation without voids nucleation. When the normal stress increases to 400 MPa, the maximum value of Von Mises stress is still smaller thanσ_y, but the maximum phase boundary stress actually exceeds the critical value. Therefore, this second category is that asperity is elastically deformed, but voids occur. The last condition is that the asperity is plastically deformed with voids initiation. Asperity with normal stress 720MPa, falls into this category, as shown in Figure 3.17 and Figure 3.18. All contact asperities are in these three categories when we analyze their deformation and crack initiation situations.

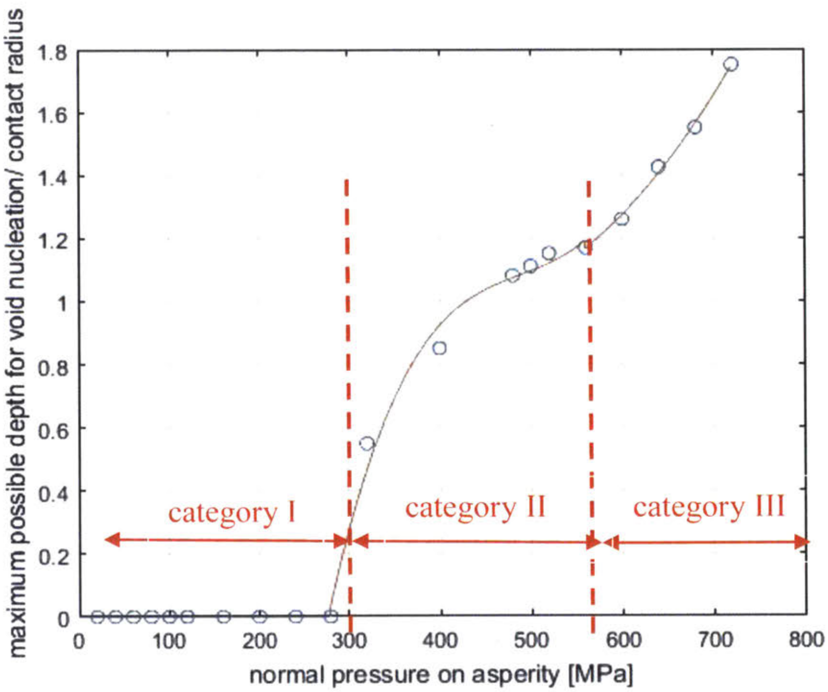

Figure 3.19 Void nucleation depth

Figure 3.19 is plot of the maximum void initiation depth as a function of normal stress from 20MPa to 720MPa. The three categories of asperities are also reflected in the trend of the void depth curve. Asperities in category I has no possibility to nucleate voids, while asperities in categories II and III will initiate voids, with elastic deformation and plastic deformation respectively. The FEA is limited to only some specific external loadings, and a third order polynomial fitting is used so that the maximum voids nucleation depth can be calculated for all normal stress, as also shown in Figure 3.19. It is important to emphasize that the depth in Figure 3.19 is the maximum possible void depth under different normal stresses. The real void initiation depth is smaller or equal to this value. In the wear simulation program, the void depth is set as a uniformly distributed random variable, with the upper bound as this maximum void depth. The depth is scaled to the ratio of void depth over the contact radius, to eliminate size effect when performing fittings.

$$\frac{maximum\ depth\ of\ voids}{contact\ radius} = c_3{P_n}^3 + c_2{P_n}^2 + c_1P_n + c_0 \qquad \text{(Equation 3.2)}$$

Where P_n is normal stress on each asperity with unit in MPa, and c_3, c_2, c_1, c_0 are the parameters in the polynomial fitting.

	category I	**category II**	**category III**
deformation	**elastic**	**elastic**	**plastic**
voids initiation	**no**	**yes**	**yes**
normal stress range [MPa]	$[0, 280)$	$[280, 560)$	$[560, 720]$
polynomial fitting parameters $[c_3, c_2, c_1, c_0]$	$[0, 0, 0, 0]$	$[8.931 \times 10^{-8}, -1.310 \times 10^{-4}, 0.065, -9.896]$	$[1.302 \times 10^{-9}, 5.446 \times 10^{-6}, -0.005, 2.001]$

Table 3.1 Summary of voids nucleation for steel

3.2.2 Nucleation of voids for gray cast iron

Section 3.2.1 introduces the void initiation process for ductile cast iron and some types of steels, and how to quantitatively calculate the related parameters, such as void initiation depth. The reason why we can precisely predict the void initiation depth for different external pressures is that the inclusions in these kinds of materials have exact shapes, spherical or cylindrical. However, this is not the case for all materials. Gray cast iron is a common type of material for cylinder liner in internal combustion engines. In gray cast iron, graphite flakes do not form into a fixed shape, which makes it very difficult to obtain an analytical expression for phase boundary stress.

According to some previous work, the fatigue process of gray cast iron is greatly related with graphite flakes imbedded in the material [31]. Voids are likely to occur at phase boundaries under external stresses. In addition, cracks also tend to propagate along those graphite flakes. However, unless we can artificially generate microstructures under each contact asperity, it is impossible to calculate voids positions and crack paths. Even artificial microstructures are generated for each asperity, the amount of calculation is extremely because thousands of asperities are contact with the ring for only a small area. Therefore, it is seasonable to consider the problem from an aspect of continuum mechanics. The maximum shear stress criterion is used for calculation of voids initiation of gray cast iron.

Figure 3.20 Microstructure of gray cast iron [32]

3.3 Crack propagation under contact asperities

With material voids generated under some contact asperities, cracks start to propagate based on these voids. If a crack meets the crack propagation criteria, it will propagate under external cyclic loading, until reaching the edge of the asperity. Then the entire asperity fractures due to this fatigue wear process. The First correlation used here is the stress intensity criteria, which tells whether a crack would keep propagating under a specific stress condition.

$$K_I = Q\sigma^{\infty}\sqrt{\pi a} > K_{IC} \qquad \text{(Equation 3.3)}$$

Equation 3.3 is the arithmetic expression of stress intensity criteria. K_I is the stress intensity factor, which is a function of geometric correlation factor Q, equivalent tensile stress σ^{∞} and half crack length a. K_{IC} is a fixed value for a material, named fracture toughness. If the stress intensity factor of a crack is greater than K_{IC}, crack would propagate, as expressed in Equation 3.3.

Once the void depth and contact radius of one asperity are calculated, the crack length leading to fracture of that asperity is also determined. The number of cycles leading to fracture is an important parameter, relating the fatigue wear process with time. Based on the work of Paris in the 1960's, fatigue life prediction for cracks was made easier and more quantitative [33]. In Paris' theory about fatigue crack propagation, it is postulated that the range of stress intensity factor is a critical parameter for crack growth under fatigue loading and the plot of crack growth rate against range of stress intensity factor gives straight lines on log-log scales [34]. This implies that:

$$\frac{da}{dN} = C(\Delta K_I)^m \qquad \text{(Equation 3.4)}$$

Where C and m are constants. N is the number of loading cycles and ΔK_I is the difference between maximum and minimum values of stress intensity factor.

$$N = \frac{1}{A}\frac{1}{(\Delta\sigma\sqrt{\pi})^m}\int_{ai}^{af}\frac{da}{(Q\sqrt{a})^m} \qquad \text{(Equation 3.5)}$$

3.4 Fatigue wear model based on two-body asperity contact

Based on each sub-model introduced in the previous content, a final two-body fatigue dominated wear model of liner surface is developed. This wear model includes the following essential steps: asperity contact, liner surface plastic deformation, voids initiation, crack propagation and asperity fracture. These steps are applied for each sliding contact. The flowchart in Figure 3.21 shows the algorithm of this fatigue wear model, which integrates all critical mechanisms in wear process.

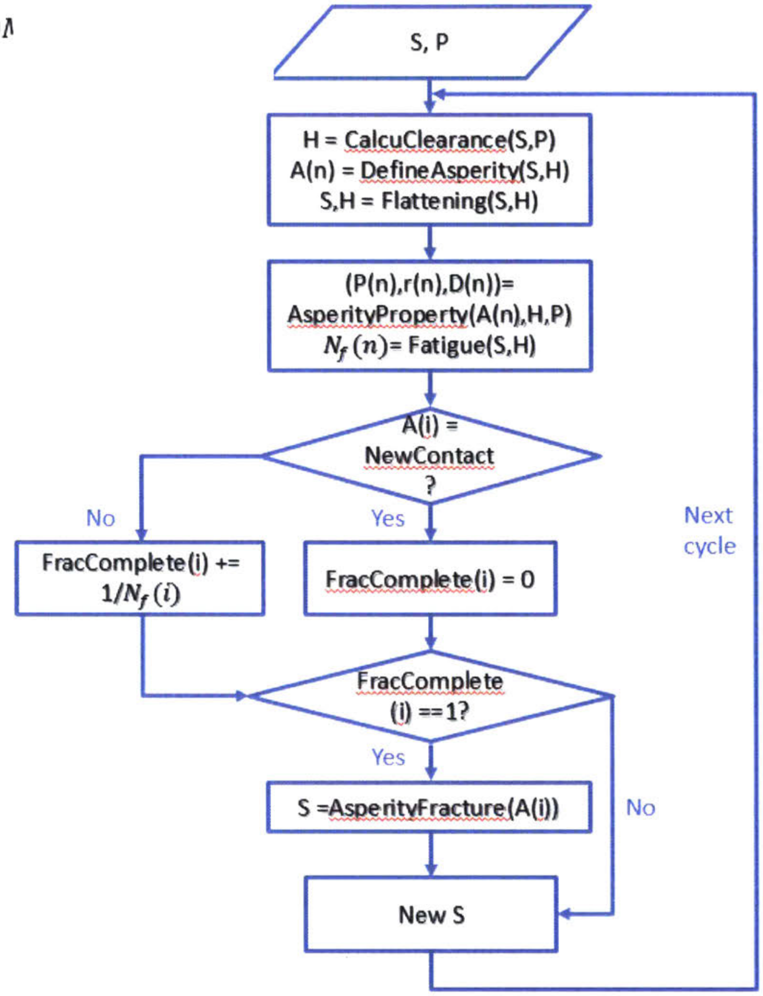

Figure 3.21 Algorithm of the fatigue wear model

In Figure 3.21, the wear algorithm needs two input variables: rough liner surface (S), represented by a matrix, and an external normal pressure (P). First, the algorithm finds the clearance (H) between the liner base altitude and the flat ring surface, according to the asperity contact model and the provided surface and pressure. All contact asperities (A(n)) are defined once the clearance is determined, including each asperity's radius of curvature, penetration depth, average normal pressure and real contact area. With all the information for each asperity, the algorithm performs the surface plastic flattening calculation, getting a new surface S and a new clearance H. At this time, most of the asperities are flattened to elastic contact with the ring. Then, the algorithm uses the parameters stored in A(n) and the current clearance, to calculate the void initiation depth D(n), and the number of stress cycles needed for each asperity to fracture $\mathrm{N_f(n)}$. Next, the algorithm checks with each asperity whether it contacts with the ring for the first time. If it is, the fracture completeness factor is set to 0, indicating the fracture process just starts. Otherwise, the fracture completeness increases with $\frac{1}{\mathrm{N_f(n)}}$. The final step for each sliding process in the algorithm is finding all the asperities with fracture completeness factors larger or equal to 1, and removing these asperities. After all these calculation processes in the algorithm for one sliding, a new surface is generated. This new surface is sent back to the beginning to replace the surface in the previous cycle, and the algorithm calculates wear loss of the next cycles based on this new surface.

The wear model presented above is a two-body contact, fatigue dominated model. The model does not include the wear effect caused by third-body particles, which mainly consist of wear debris and soot particles. Therefore, the wear rate predicted using this model underestimate the real wear rate under the same external normal load. This can also be revealed from the surface topology change, compared with experiments. Figure 3.22 to Figure 3.25 present the GG30 liner surface before and after 6×10^4 cycles of fatigue wear, where each cycle contains two sliding times. In the zoomed surface plots, Figure 3.24 and Figure 3.25, it is easy to observe that fatigue wear leads to worn surface with pits, due to asperities removal process. Because cracks form below the top surface, asperities fracture would leave regions lower than surroundings to form pits. And the depths of these pits are exactly the corresponding crack depths of those asperities when they are still in contact with the ring.

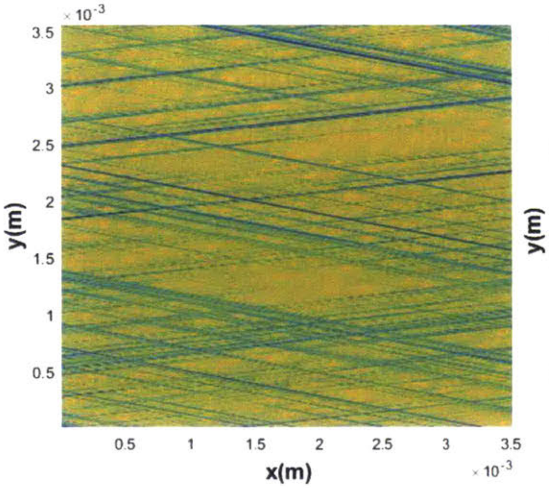

Figure 3.22 GG30 before wear

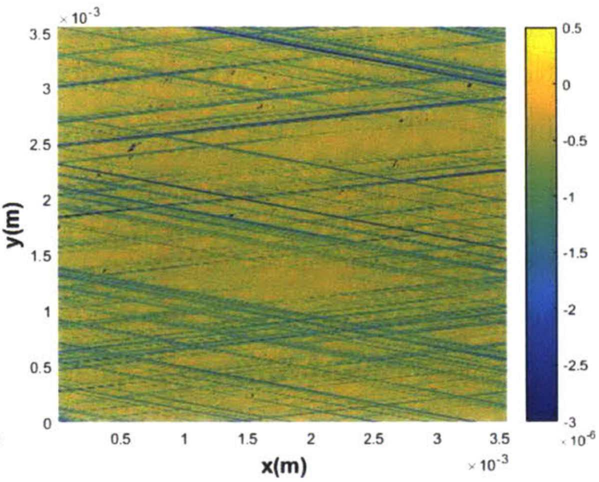

Figure 3.23 GG30 after fatigue wear

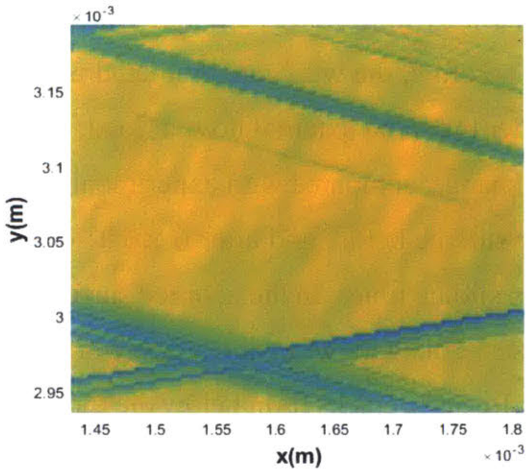

Figure 3.24 GG30 before wear (zoomed)

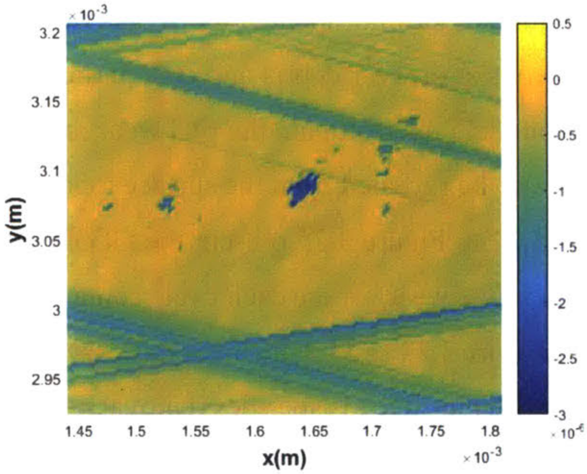

Figure 3.25 GG30 after fatigue wear (zoomed)

Pit-like structures on a worn surface are typical structures caused by fatigue wear. This is also observed by the research group of Suh. Figure 3.26 is a picture detected by electronic an electronic microscope, while a contact asperity is about to fracture due to fatigue wear. The fracture of this asperity eventually leaves a deep pit on the surface. However, in experiments, scratches are another important structures caused by third-body wear, as also shown in Figure 3.26. But such a kind of worn structures are not simulated in this two-body wear model. Some initial work for third-body wear simulation is presented in Chapter 5.

Figure 3.26 An asperity is about to wear off due to fatigue [4]

3.5 Simulation results of two-body fatigue wear model

In this section, some simulation results are presented, using the two-body contact fatigue wear model. Liner surfaces with different finishes are tested to investigate their wear behaviors, including GG07, GG09, GG21, GG28 and GG30. For each surface, external nominal pressure changes from 1 MPa to 4 MPa in order to study the effect of pressure on fatigue wear as well. The results satisfy the Archard's equation, indicating that the steady state wear rate is proportional to external normal pressure for a specific surface. In addition, some artificial liner surfaces are created by increasing or decreasing the unit length in x and y directions of surface GG30. Using these deformed surfaces as inputs of the fatigue wear model can further provides with information about how of surface properties are related to fatigue wear.

3.5.1 Fatigue wear of different liner surfaces

For wear of metals, Archard's law is a widely used correlation which describes sliding wear and is based on the theory of asperity contact. It indicates that the volume of wear debris for metal sliding is proportional to the product of normal load and sliding distance, but is inversely proportional to the material hardness [35][36].

$$V = k\frac{PL}{3H} \qquad \text{(Equation 2.6)}$$

In equation 2.6, V is the volume of wear debris, and P, L, H are external normal pressure, sliding distance, material hardness, respectively. k is wear coefficient, which is a constant for a certain material with a specific surface finish.

Wear is an integrated process of all mechanisms, with a total material removal rate indicated by equation 2.6. Moreover, it is interesting to show that fatigue wear also satisfies Archard's law based on simulation results. Wear rate in steady state is proportional to normal pressure. It is still unclear whether other wear mechanisms also have such correlations, but as one important mechanism in metal wear, fatigue wear obeys equation 2.6. Therefore, it is possible and essential to calculate the wear coefficient of surfaces with different finishes. For example, Figure 3.27 shows the wear volume of GG30 under constant normal pressure of 1 MPa to 4MPa. So as to eliminate the effect of the size of simulated surfaces, the wear volume is converted to average height reduction over the entire surface.

In Figure 3.27, an apparent conclusion is that the wear rate of the liner surface is large at the beginning, but gradually reduces to a steady value for all different nominal stresses. It is pointed out in section 2.4, plastic flattening can cause significant height reduction at the starting period of wear, increasing the portion of elastic contact at the same time. After this transition state, fatigue wear becomes the dominant mechanism while the wear rate also reaches a steady state. The wear loss curves are not smooth, with many discrete increments. Fatigue wear process is continuous since cracks are propagating at any epoch, but the fracture of asperities is a discrete process. If a crack is growing under a contact asperity, the wear loss due to the detachment of this asperity can be taken into account only at the moment when it is fractured. Moreover, the detachment of one asperity causes a loss of the total contact force with the ring, so the ring must reduce its height a little bit to increase the total contact area or find more asperities to support the load. During this piston ring height adjustment process, more plastic deformation also occurs, resulting surface height reduction. Therefore, the wear loss curves have a lot of 'discrete jumps'. To better interpret this wear loss process, the normalized piston height reduction is also plotted in Figure 3.28. At the beginning of wear, due to the significant plastic flattening, piston ring goes down fast to keep the total force as a constant. Then after the wear rate reduces to a steady state, the ring height reduction rate also reduces.

In addition, another important conclusion drawn from the wear loss plot, is that the steady state wear rate is proportional to external pressure. Figure3.29 contains the plot of steady state wear rate of GG30 as a function of external pressure, indicating the approximate linear relationship between the two parameters. Based on the Archard's correlation, the corresponding wear rate k of GG30 surface finish can be obtained through linear regression, as the red straight plotted in Figure3.29. The corresponding dimensionless wear coefficient of GG30 is about 1.5×10^{-8}.

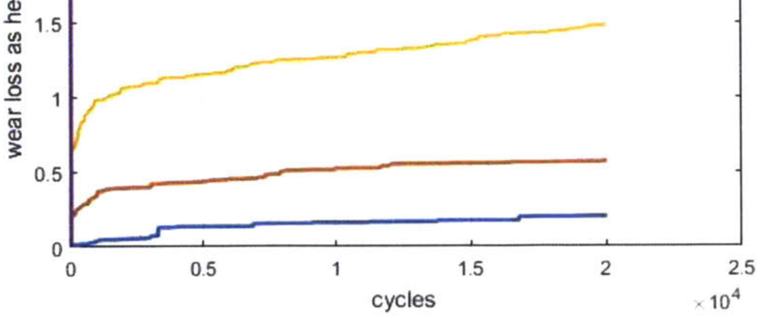

Figure 3.27 Wear loss of GG30 with different normal pressures

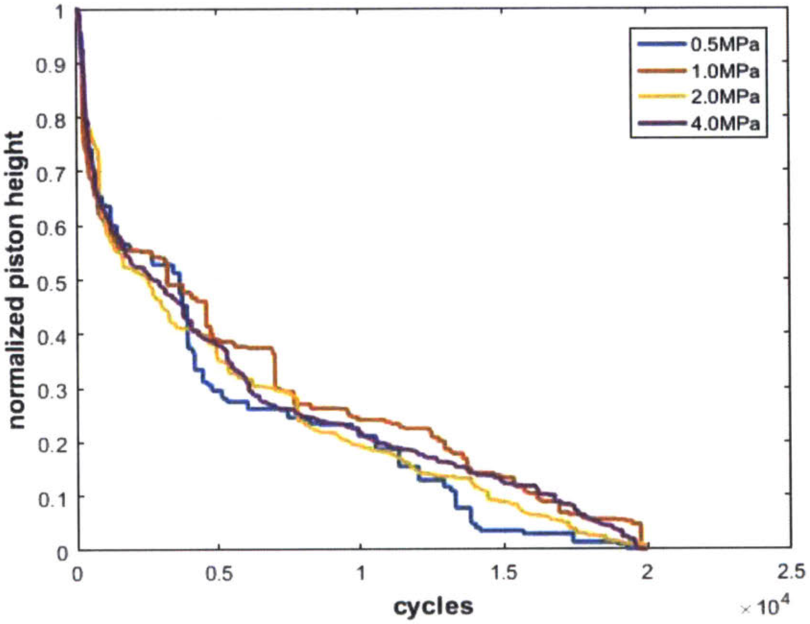

Figure 3.28 Normalized piston height change during wear of GG30

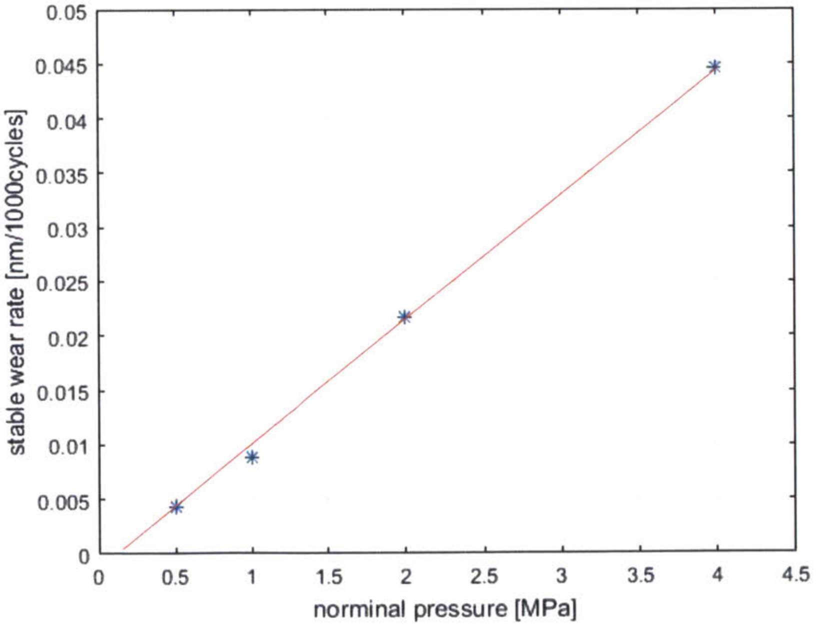

Figure 3.29 Steady state wear rate of GG30 as a function of normal pressure

So as to quantitatively understand this linear relationship between normal pressure and steady state wear rate, a new intermediate parameter is introduced: continuous wear speed. As explained in previous paragraphs, the wear loss calculation contains discrete fractures of asperities, which makes it difficult to mathematically interpret why it fits the Archard's law. The wear rate can only be obtained as a statistical parameter for all asperities over a certain time period rather than a deterministic parameter. However, the continuous wear speed is defined as a parameter which can be calculated deterministically on the level of a single asperity.

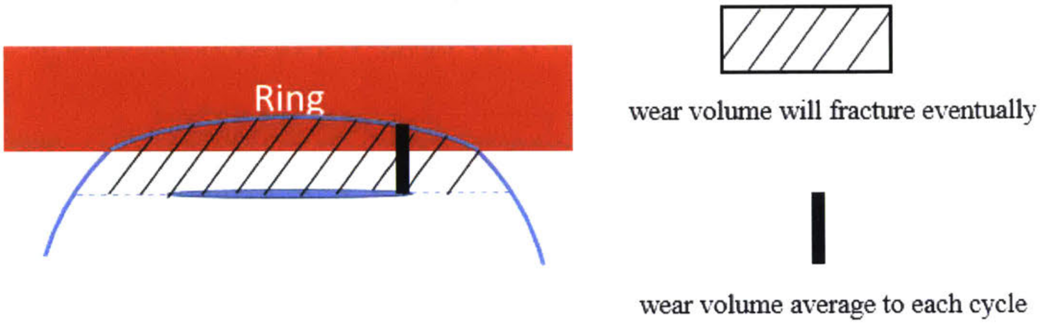

Figure 3.30 Continuous wear speed for one asperity

In the definition of continuous wear speed, wear volume of each asperity is averaged over the entire number of cycles leading to fracture. This definition makes the wear volume as a continuous process that an asperity losses its volume for every cycle. The summation of this averaged wear speed for all asperities is then the continuous wear rate for the surface. The advantage of introducing this continuous wear rate is that it provides a different aspect to interpret wear rate from the deterministic level for each asperity.

$$W_c = \sum_{i=1}^{n} \frac{V_f}{N_{cycle}} \qquad \text{(Equation 2.7)}$$

Equation 2.7 is the arithmetic expression for continuous wear speed W_c. For GG30 liner surface, W_c is also proportional to external pressure at the steady state wear period, as shown in Figure 3.31. Therefore, the real wear rate is also reasonable to be proportional to pressure because it can be viewed as a transition into discrete time space from this continuous wear speed.

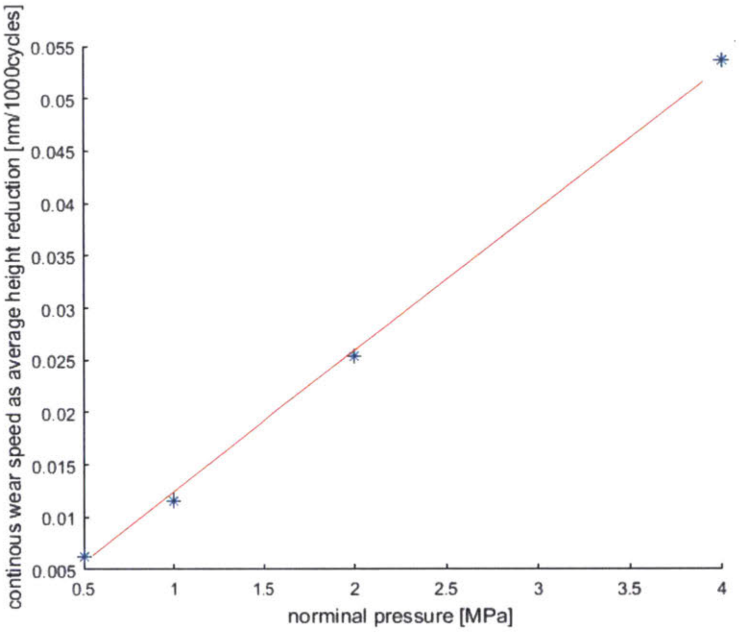

Figure 3.31 Continuous steady state wear rate of GG30

Except for GG30, some other surface finishes are also used as inputs of the fatigue wear model: GG07, GG09, GG21 and GG28. Figure 3.2 to Figure 3.35 are the corresponding wear loss plots for these surface finishes. The steady state wear rate for all these surfaces finishes are presented in Figure 3.36. From Figure 3.36, it is easy to know that the proportionality between steady state wear rate and normal pressure can be extended to all surfaces. Wear coefficient for each surface is obtained through linear regression. The slopes of regression lines in Figure 3.36 provide intuitionistic comparisons for wear coefficients. It is essential to point out that the slopes of regression lines of GG21, GG28 and GG30 have approximately the same value, indicating wear coefficients of these surfaces are very close. The reason why these three different finishes lead to similar wear coefficients of the liner surface can be explained from their manufacturing procedures. The only difference among GG21, GG28 and GG30 is the height of fine finish, as presented in Figure 3.37. The manufacturing process is the same before the step of fine finish, while the fine finish is completed at different height. Although the plateau ratios are different for these three surface finishes due to fine finish, plateau regions have the same roughness level. The size and shape of contact asperities are also statistically the same for the three finishes. This is the reason why their wear coefficients are so close.

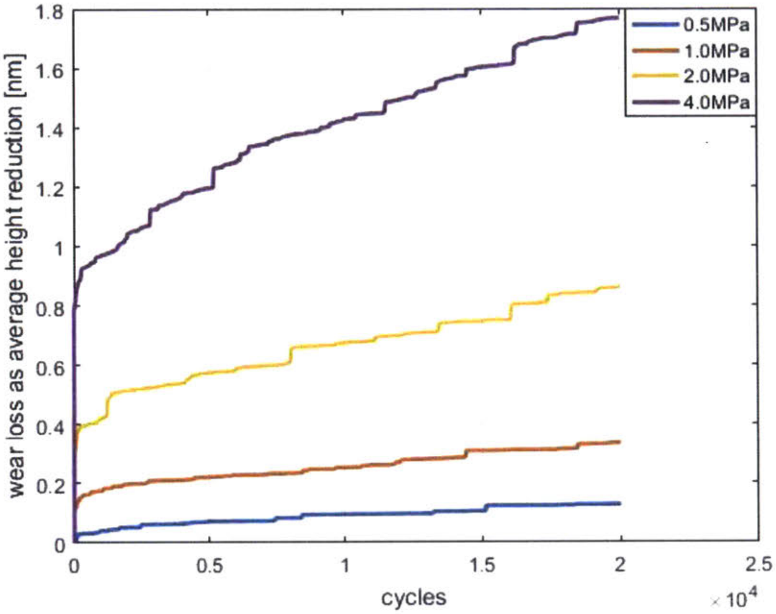

Figure 3.32 Wear loss of GG07 with different normal pressures

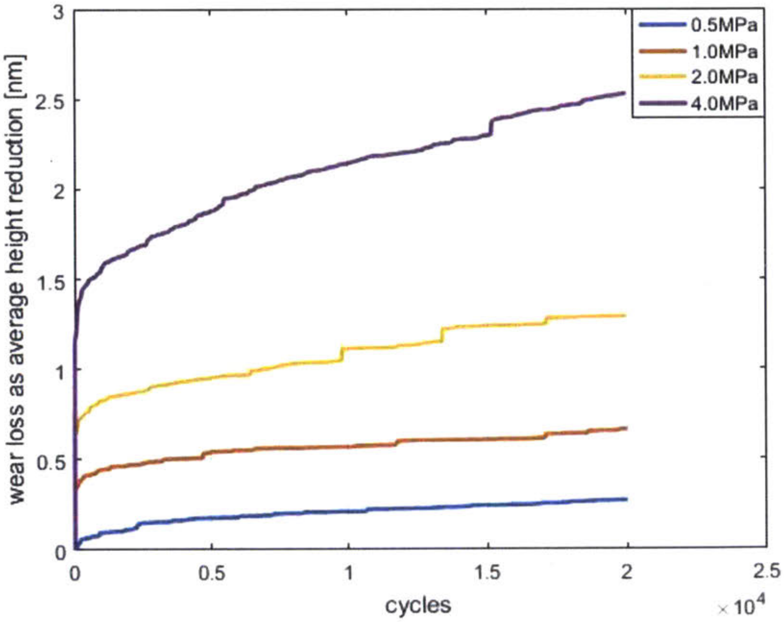

Figure 3.33 Wear loss of GG09 with different normal pressures

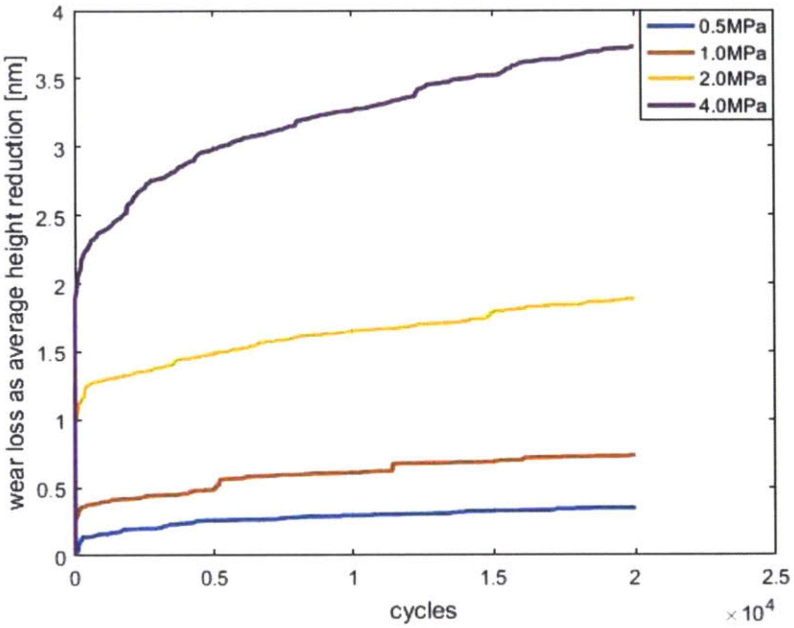

Figure 3.34 Wear loss of GG21 with different normal pressures

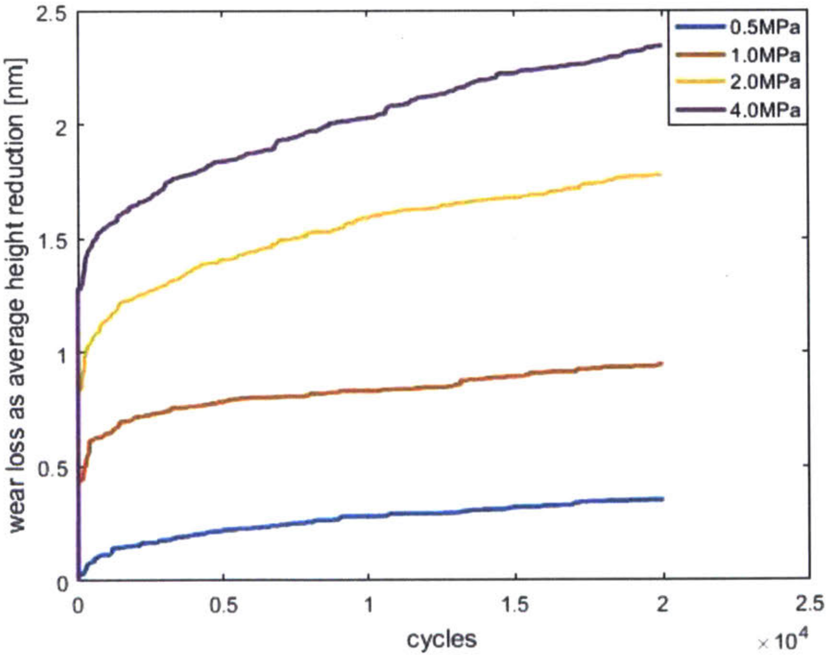

Figure 3.35 Wear loss of GG28 with different normal pressures

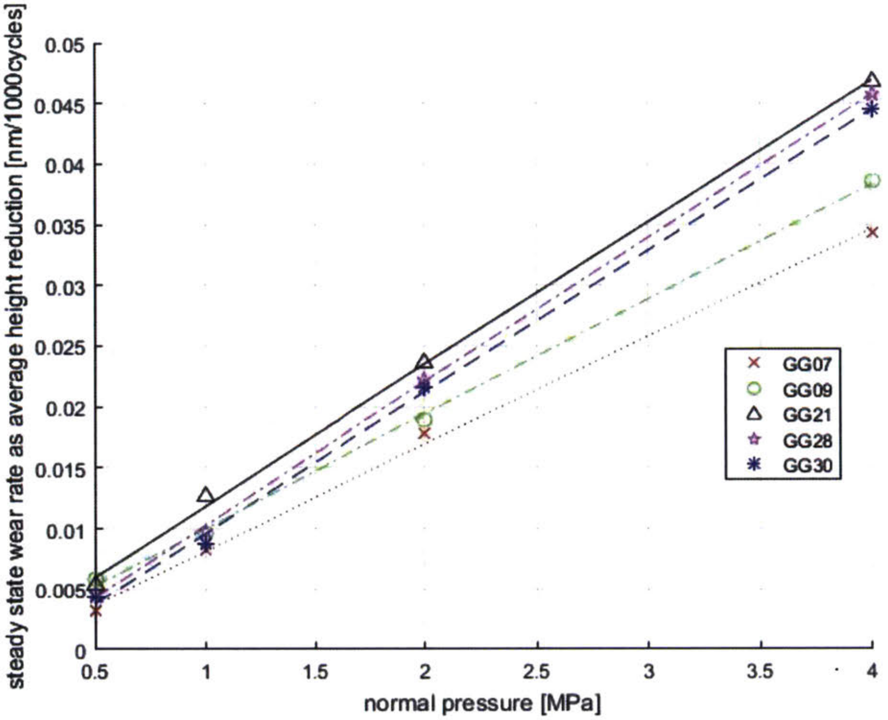

Figure 3.36 Steady state wear rate of different surface finishes

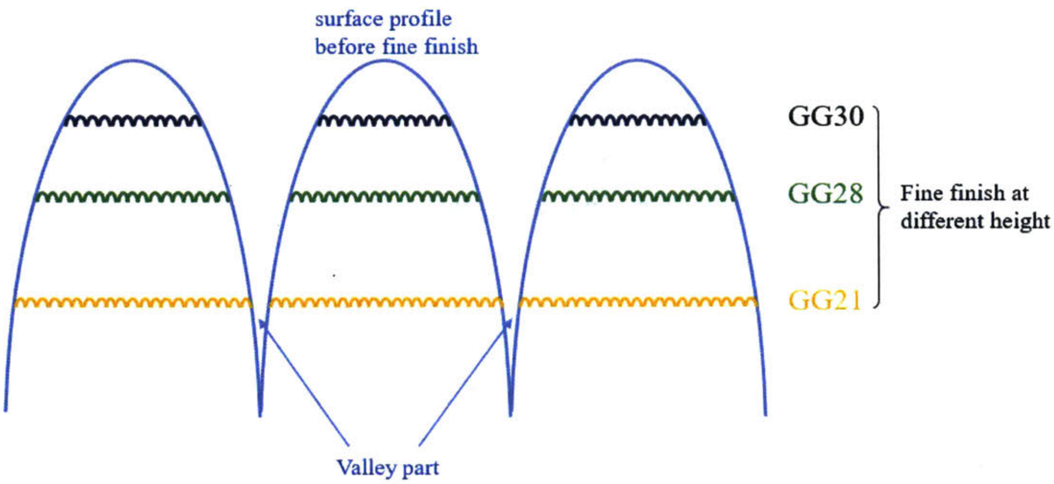

Figure 3.37 Comparison among three different surface finishes GG2, GG28 and GG30

From the above discussion, it is naturally to get a conjecture that the steady state wear rate depends on the size and shape of surface asperities. GG21, GG28 and GG30 surfaces have the same fine finish, but GG07 and GG09 are not. Therefore, the wear coefficients of GG07 and GG09 are different from the other three. Table 3.2 lists the wear coefficients of cast iron with different surface finishes. Wear coefficients of GG07 and GG09 are significantly smaller than that of GG30, mainly because the surface asperities of GG07 and GG09 are larger. The correlation between asperity size and wear coefficient will be discussed in detail in section 3.5.2.

Surface finish	**GG07**	**GG09**	**GG21**	**GG28**	**GG30**
Wear coefficient ($\times 10^{-8}$)	**1.14**	**1.22**	**1.51**	**1.53**	**1.50**

Table 3.2 Wear coefficients of GG07, GG09, GG21, GG28 and GG30

3.5.2 More investigation of fatigue wear simulation

In the previous section, the simulation results show that the wear rate of a surface depends greatly on its roughness level, especially the size and shape of contact asperities. In order to seek more detailed underlying correlations, more simulations are conducted for fatigue wear. One trial is changing the flatness of liner surface asperities, and finding some clues for design of surface manufacturing.

As mentioned in Figure 2.20, the matrix representing a rough liner surface has specific resolutions in x and y directions, dx and dy. For all previous simulations, dx and dy have the same value of 1.122 μm, which is just the resolution of the confocal microscope used in measurements. Then, in this section, dx and dy are stretched with a scale of 0.5, 2, 4 and 8, to modify the flatness of liner surface asperities. Larger stretched scale means more flat asperities. Other simulation parameters remain the same as previous simulations.

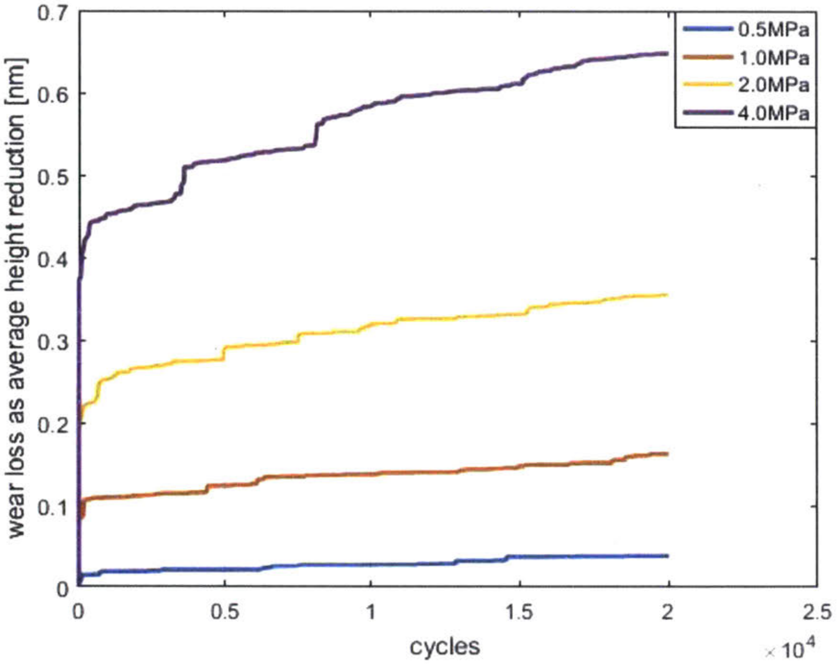

Figure 3.38 Wear loss for GG30 with stretched scale of 0.5 in x and y directions

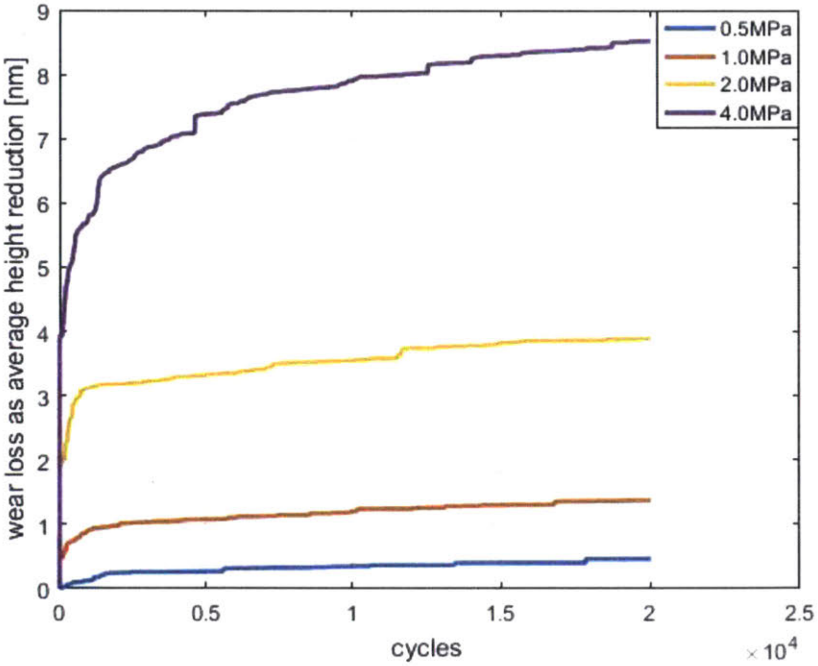

Figure 3.39 Wear loss for GG30 with stretched scale of 2 in x and y directions

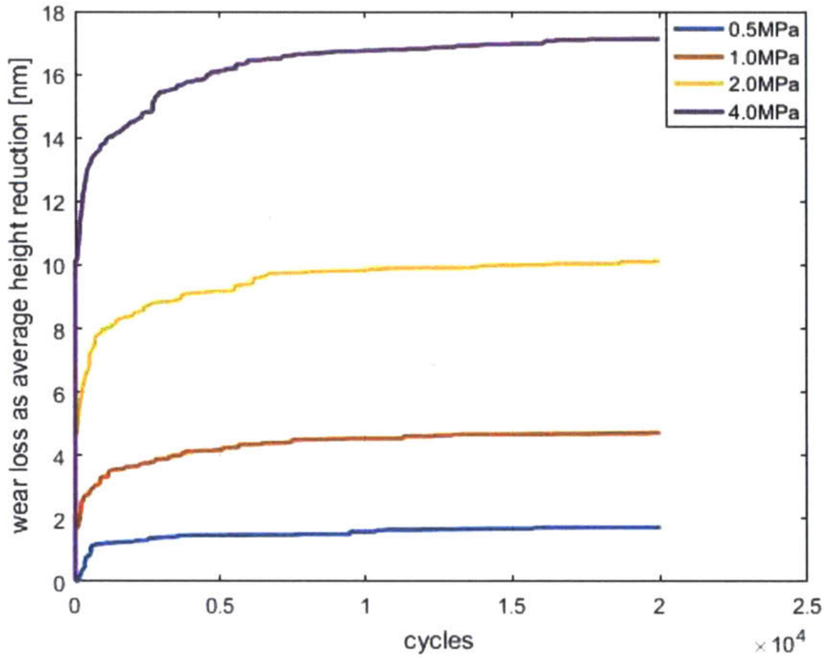

Figure 3.40 Wear loss for GG30 with stretched scale of 4 in x and y directions

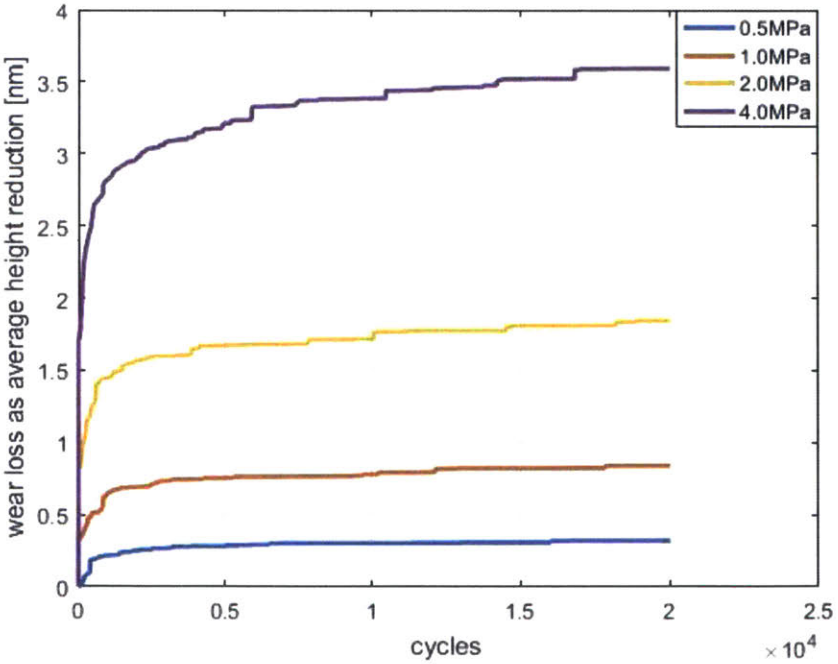

Figure 3.41 Wear loss for GG30 with stretched scale of 8 in x and y directions

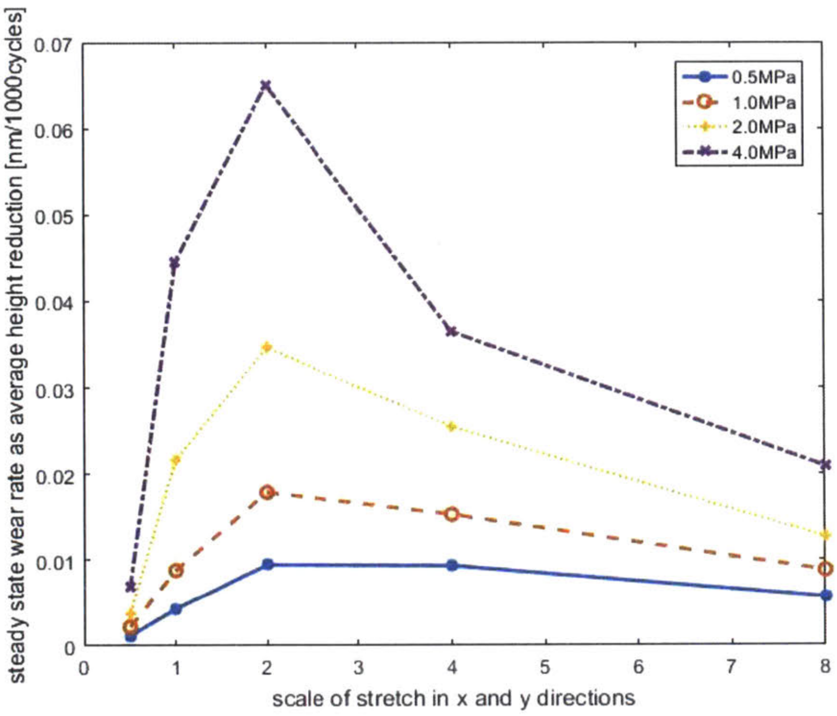

Figure 3.42 Steady state wear rate for different stretched scales in x and y directions

Figure 3.38 to Figure 3.41 show the wear loss as average height reduction for GG30 with different stretched scales, from 0.5 to 8. Wear of a stretched surface also experiences a transient period with a high wear rate, then reaches a steady wear state. Larger external pressure still leads to greater wear loss, but the proportional Archard's correlation is only valid for surfaces with stretched scale within a certain range.

The steady state wear rate under different stretched scales and normal pressures is summarized in Figure 3.42. With a constant normal pressure, the steady state wear rate first increases then decreases as the scale of surface stretch continuously increases. The maximum steady state wear rate for all normal pressures occurs with the stretched scale of 2, with the corresponding matrix resolution 2.244 μm. If liner asperities are too sharp or too flat, the steady state wear rate would be small. This interesting result indicates that there is an optimal asperity flatness if the designer of liner surfaces wants to minimize the break-in period. Figure 3.43 explains why this optimal asperity flatness exists.

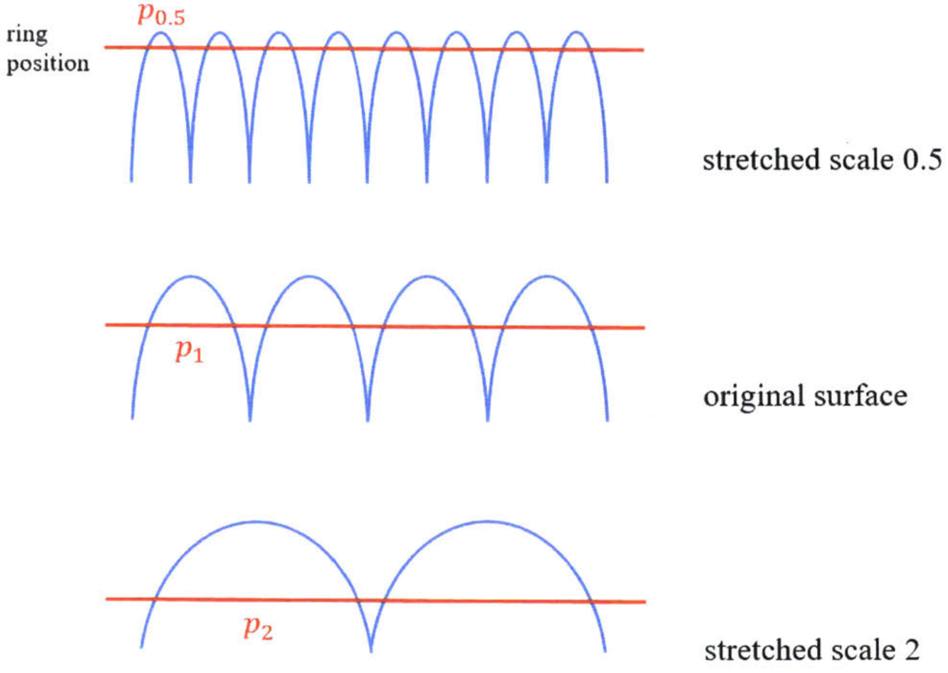

Figure 3.43 Asperities with different flatness under the same normal pressure.

As shown in Figure 3.43, the original surface is modified with a stretched scale of 0.5 and 2, keeping the height of asperities a constant. It is assumed that all asperities have the exact same shape. Because asperities of the surface with stretched scale 0.5 have the smallest radius of curvature, they have the largest average contact pressure $p_{0.5}$ when the liner contacts with the ring. Therefore, the overlapping volume of this liner surface and the ring is also the smallest, resulting a low steady wear rate. When the asperities are continuously flattened, the overlapping volume also increases as in Figure 3.43 since the average contact pressure is decreasing. However, because of the reduction of contact pressure on each asperity, the crack propagation rate actually decreases. The two influence factors, overlapping volume and crack propagation rate, are actually competitive as asperities are flattened. If the effect of crack propagation rate reduction takes the dominant position, the steady wear rate will decrease. This is the reason why the maximum wear rate occurs at a certain asperity flatness level.

The simulation results in Figure 3.42 also reveals that the Archard's law only fits with stretched scale of 0.5, 1 and 2. When asperities become too flattened, the proportional relation in Archard's law no longer exists. An extreme case can be helpful to understand this trend: when the liner surface is ideally smooth with only a single flat asperity, the contact pressure on this asperity is just equal to the external normal pressure. External normal pressure is usually far below the critical pressure value leading to fatigue wear, resulting that the wear rate is always zero.

Conclusion

Unlike the mechanism of surface plastic flattening, fatigue wear is continuous and occurs at least after several hundreds of cycles. Fatigue wear can always reach steady state with a constant wear rate. Simulation results indicate that Archard's law can be applied to different liner finishes, with proportional correlations between external pressure and steady state wear rate.

The wear coefficient is greatly influenced by asperity flatness, which is mainly determined by the fine finish process. GG21, GG28 and GG30 have approximately the same wear coefficient value because they experience the same fine finish step during manufacturing. Under the same external pressure, a specific asperity flatness level corresponds to the maximum steady wear rate. This may be applied to surface roughness design in the future to minimize the break-in period.

Chapter 4. Influence of liner wear on lubrication

In this chapter, the influence of liner wear on lubrication conditions is studied and compared with experimental results, through the friction calculation under one complete cycle. The theoretical calculation of friction is performed by both the model of hydrodynamic pressure and the model of dry contact. The wear process of different liner finishes is simulated by the two-body wear model, and friction curves are plotted for surfaces before wear and after wear. Although only the two-body mechanisms are considered in the wear model, the results of friction calculation are in accordance with experimental friction measurements.

4.1 Hydrodynamic correlations and the dry contact model

As the piston ring slides to different positions on the liner, the mean clearance also changes, leading to the change of hydrodynamic pressure. In order to obtain the correlations between the ring-liner clearance and hydrodynamic pressure, a deterministic model is applied. According to this model, the dependency of the average hydrodynamic pressure on the ring-liner clearance can be expressed by the following equation [37]:

$$P_{hydro} = \frac{\mu V}{\mu_0 V_0} P_h (\frac{h}{\sigma_p})^{-K_h} \qquad \text{(Equation 4.1)}$$

In Equation 4.1, μ_0 and V_0 are the reference viscosity and reference sliding speed, while μ and V are the corresponding real parameters. P_h and K_h are constants. $\frac{h}{\sigma_p}$ is the ratio of average clearance and the standard deviation of the plateau part.

Similarly, the hydrodynamic shear stress can be correlated with the ratio $\frac{h}{\sigma_p}$ through the following analytical expression [37]:

$$f_{hydro} = \frac{\mu V}{h}\left(C_1 + C_2 \exp\left(C_3 \frac{h}{\sigma_p}\right)\right) \qquad \text{(Equation 4.2)}$$

C_1, C_2 and C_3 are constants

The total pressure is the sum of contact pressure and hydrodynamic pressure. The contact pressure also depends on clearance, which can be determined by the contact model in Chapter 2. So as to integrate the contact correlation into the friction model of the entire engine cycle, an analytical expression is also developed [38]:

$$P_c = K'E'A\left(\Omega - \frac{h}{\sigma_p}\right)^Z \qquad \text{(Equation 4.3)}$$

Here K', A, Ω and Z are constants for a specific surface. E' is the equivalent elastic modulus of the two contact surface:

$$E' = \frac{2}{\frac{1-v_1{}^2}{E_1} + \frac{1-v_2{}^2}{E_2}}$$

Where v_1, v_2, E_1 and E_2 are the Poisson ratio and elastic modulus of the two contact materials.

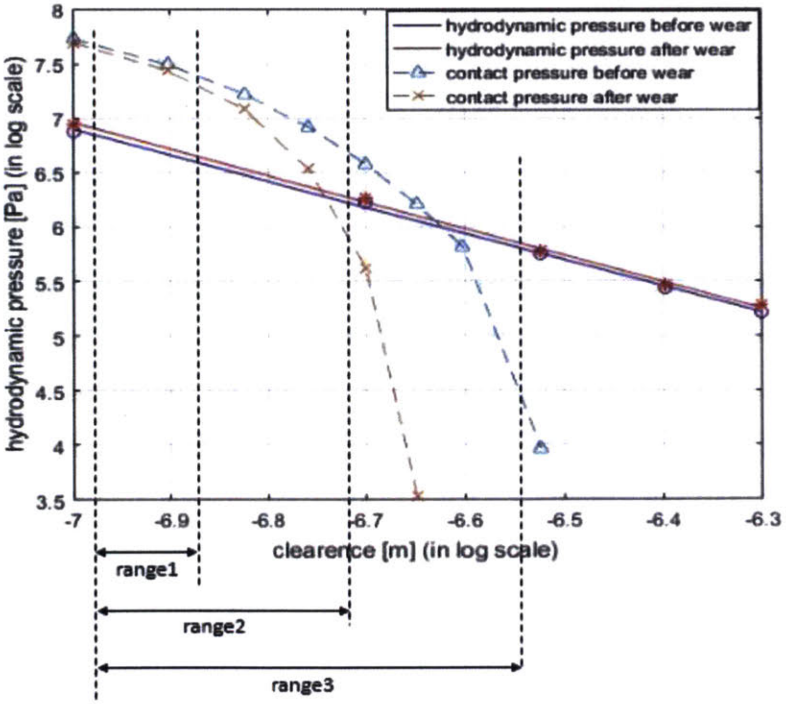

Figure 4.1 Hydrodynamic pressures and contact pressures of GG30, before wear and after 5 hours running under external load 2MPa

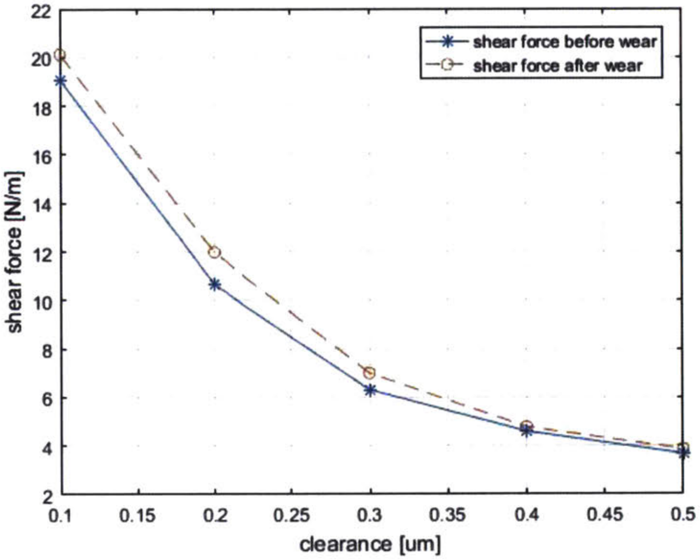

Figure 4.2 Normalized shear stress of GG30, before wear and after 5 hours running under external load 2MPa

Both contact pressure and hydrodynamic pressure of GG30 surface finish are plotted in Figure 4.1 as functions of the ring-liner clearance. The wear simulation of GG30 is done by the two-body fatigue, with simulated duration 5 hours, engine speed 400 rpm and external nominal pressure 2MPa. Compared with the original surface, the surface after wear simulation has approximately the same hydrodynamic pressure, but the contact pressure is greatly reduced because the asperities are flattened and gradually fractured. When the ring-liner clearance is small, the contact pressure has not changed due to the wear process since the surface honing structure still remains after 5 hours' break-in wear. Small clearance exists for low sliding conditions, especially when the piston moves to the top dead center or the bottom dead center. When the clearance becomes larger, the reduction of the contact pressure is significant, and this can be reflected in the friction plot for the entire running cycle, which will be discussed in Section 4.2. The hydrodynamic friction force is plotted in Figure 4.2, with fitted curves of Equation 4.2. Although the hydrodynamic shear stress increases after wear, the total friction between the ring and the liner usually decreases because of the loss of contact pressure.

4.2 Friction for the entire engine cycle

In this section, the correlations of hydrodynamic pressure, hydrodynamic shear stress and contact pressure introduced in the previous section are utilized to obtain the friction curves for the entire engine cycle. Friction curves of different liner finishes are compared with the experimental measurements. All parameters used in experiments and simulations are listed in Table 4.1.

Ring width	Ring tension	Cylinder temperature	Oil temperature	Oil type	Liner finish
0.15mm	19.5N	80°C	80°C	HTHS 1.4	GG07, GG09, GG21, GG30

Table 4.1 Variables used in experiments and the friction cycle model

As the ring-liner clearance depends largely on the ring sliding speed, the friction also varies for each engine cycle, with the minimum friction value occurs at the mid stroke. As noted in Figure 4.1, the range of clearance for an engine cycle, is determined by the engine running speed. Range1, range 2 and range 3 are the range of clearance for engine speed 100rpm, 500rpm and 1000rpm, respectively. Since the sliding speed is about zero at the top dead center or the bottom dead center, these three ranges have close lower bounds. When the clearance reaches this smallest value, both contact pressure and hydrodynamic pressure do not have obvious change after wear. This is consistent with the friction curves in Figure 4.3 to Figure 4.5, in which the friction does not change much after wear when the crank angle is near 0 or 180 degrees. Unlike the lower bound of the clearance range, the upper bound can vary with different sliding speed, increasing as the engine speed increases. When the engine speed is 100rpm, the contact pressure has a slight drop at the upper bound of clearance, as shown in Figure 4.1. This leads to the friction reduction after wear at the mid stroke in Figure 4.3, and contact pressure is always the dominant one, much larger than the hydrodynamic pressure. As the engine

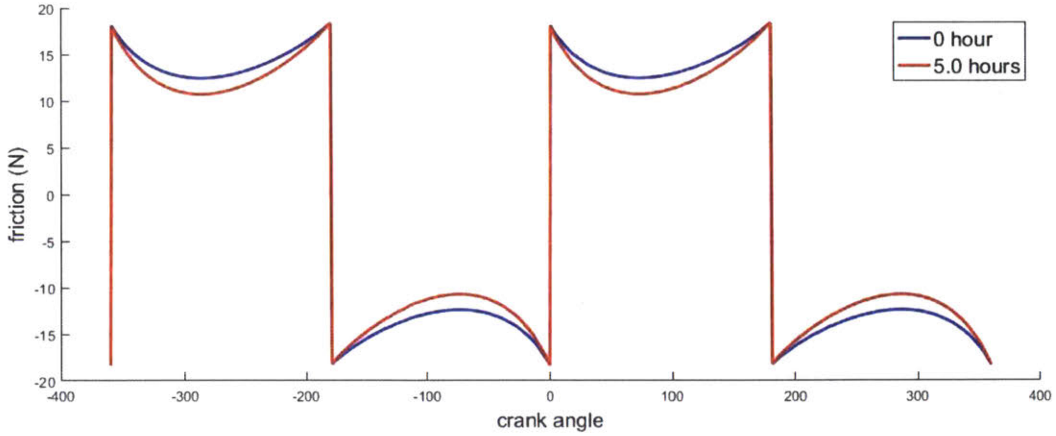

Figure 4.3 Friction of GG30 for the entire engine cycle with speed 100rpm

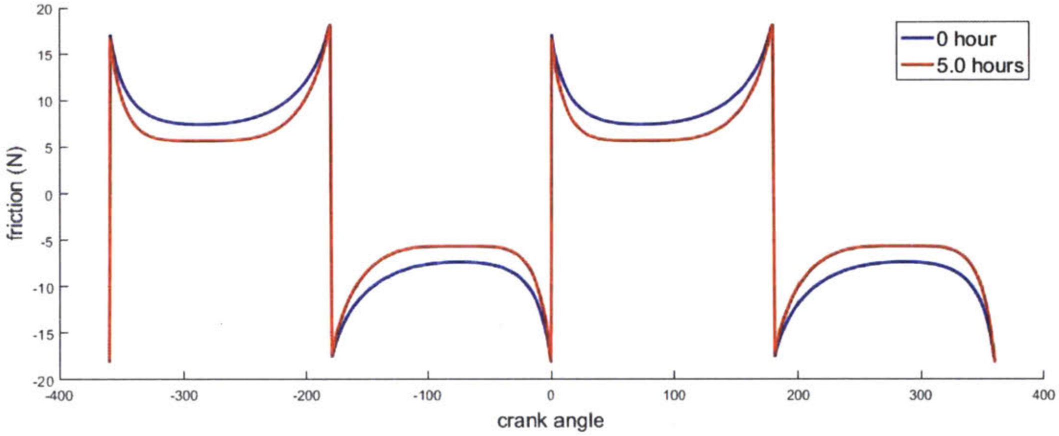

Figure 4.4 Friction of GG30 for the entire engine cycle with speed 500rpm

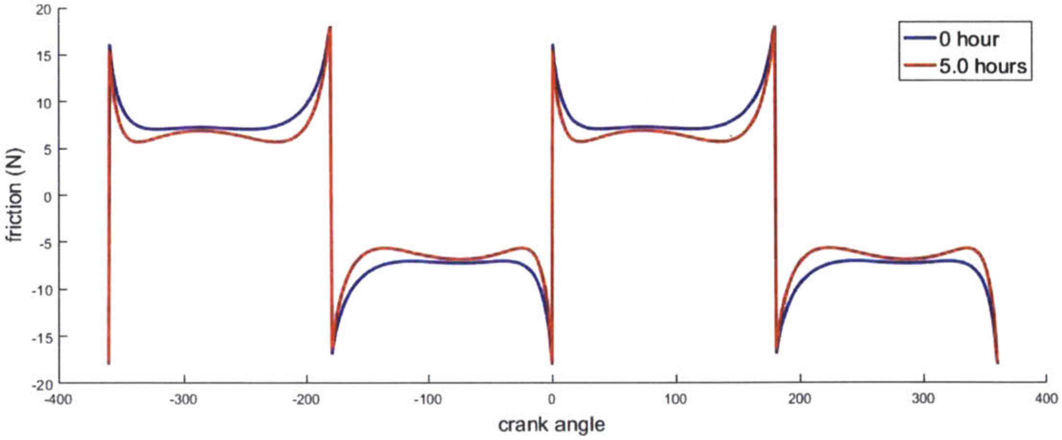

Figure 4.5 Friction of GG30 for the entire engine cycle with speed 1000rpm

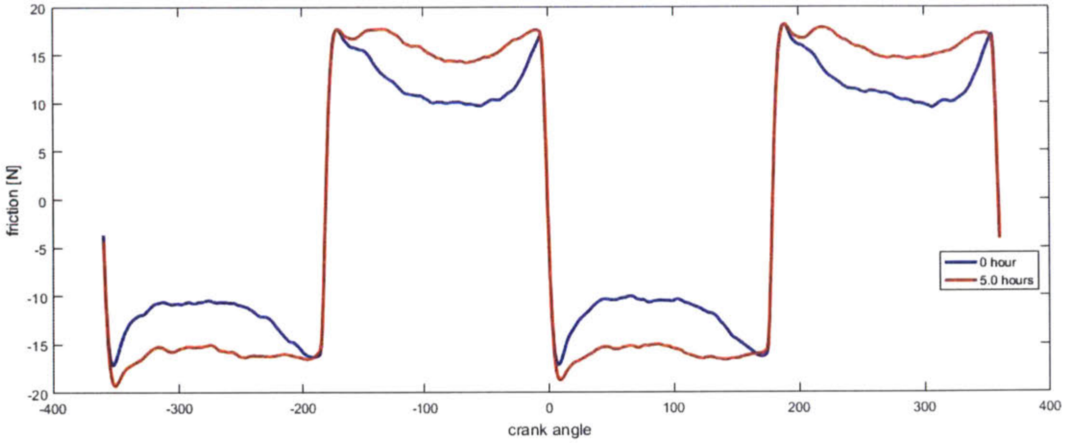

Figure 4.6 Experimental measurements for friction of GG30 with speed 100rpm [39]

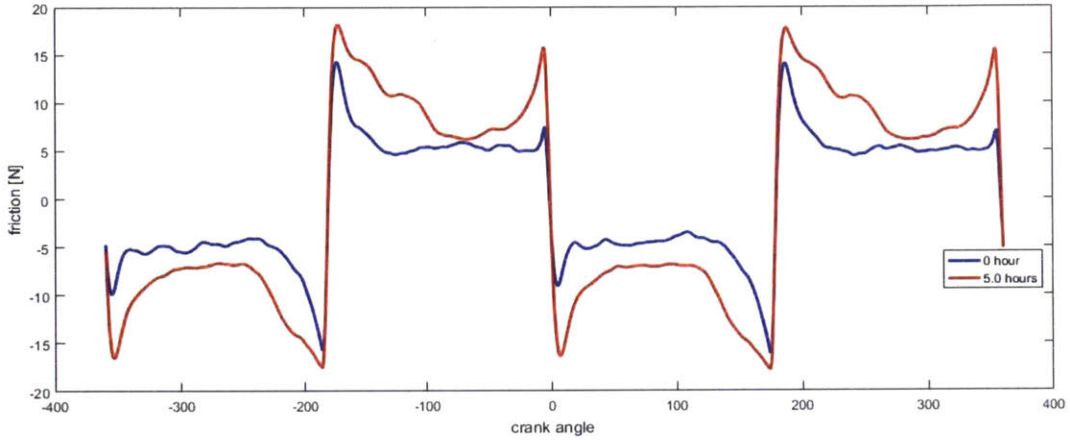

Figure 4.7 Experimental measurements for friction of GG30 with speed 500rpm [39]

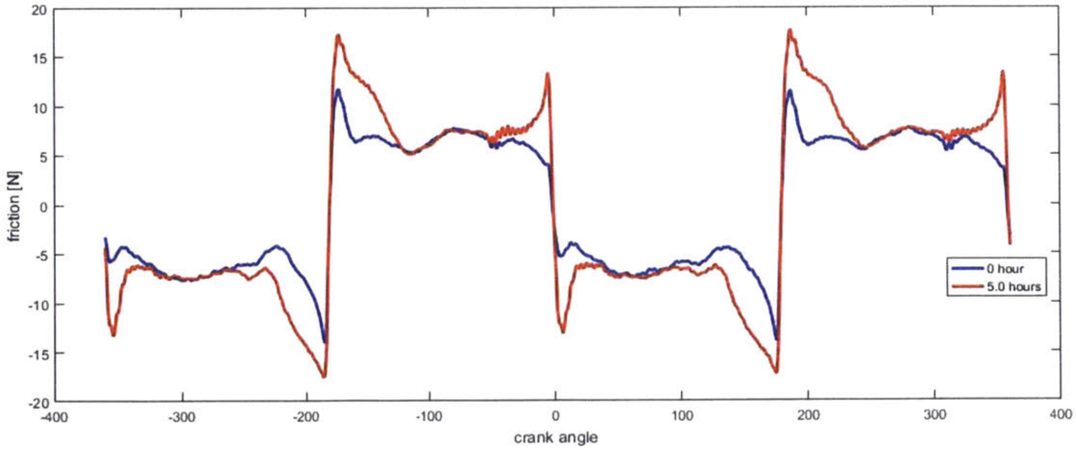

Figure 4.8 Experimental measurements for friction of GG30 with speed 1000rpm [39]

speed increases to 500 rpm, contact pressure still takes the major role at the mid stroke before wear, but it reduces below the hydrodynamic pressure. This is reflected in the friction plot in figure 4.4, the dominant role is switched from contact pressure to hydrodynamic pressure after 5 hours' wear simulation. When the engine speed reaches 1000rpm, contact pressure is much lower than hydrodynamic pressure at the mid stroke, for both before and after wear. Therefore, as shown in Figure 4.5, the friction curves become almost overlapped in the middle.

Compared with the friction measurements obtained experimentally, the trend of the relative importance between hydrodynamic pressure and contact pressure agrees well. However, the friction change after wear actually could be much larger as shown in Figure 4.6 to Figure 4.8, because only two mechanisms are included in the two-body wear model: surface plastic flattening and fatigue wear. Another important mechanism, third-body abrasive wear can actually even cause more wear loss than two-body wear does. Some work of third-body wear will be discussed in the next chapter.

Similar to liner finish GG30, the friction curves of GG07 and GG09 are also obtained through the cycle model. Unlike GG30, the contact pressure is always playing the major role regardless of the piston position, and this situation does not change after wear for 5 hours. Two reasons contribute to the difference with GG30. First, the GG07 surface finish is rougher than GG30, leading to a weaker hydrodynamic correlation. The standard deviation of the plateau part of GG 07 is 9.1×10^{-8}m, and corresponding σ_p of GG30 is only 5.8×10^{-8}m. Second, the average asperity size of GG07 is larger compared with GG30, resulting lower two-body wear rates as mentioned in Chapter 3. Therefore, the surface topology change of GG07 is also smaller, so that the friction drop of GG07 after wear is not as remarkable as GG30. The experimental measurements also support this difference between GG07 and GG30. The friction curves of GG09 indicate that the hydrodynamic pressure is about to exceed the contact pressure when the engine speed is 1000rpm, as shown in Figure 4.17. The reduction of friction is not significant since the wear rate of GG09 is also lower than GG30.

As introduced in Chapter 3, the fine finish is the same for GG21 and GG30, leading to close plateau roughness and wear rates. Therefore, as plotted in Figure 4.21 to Figure

4.23, the friction curves of GG21 for one engine cycle show similar trends as friction of GG30.

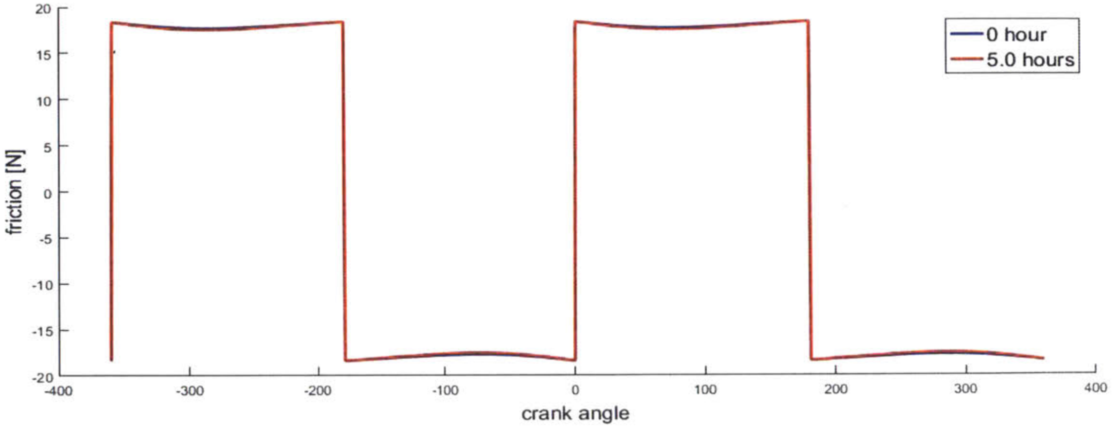

Figure 4.9 Friction of GG07 for the entire engine cycle with speed 100rpm

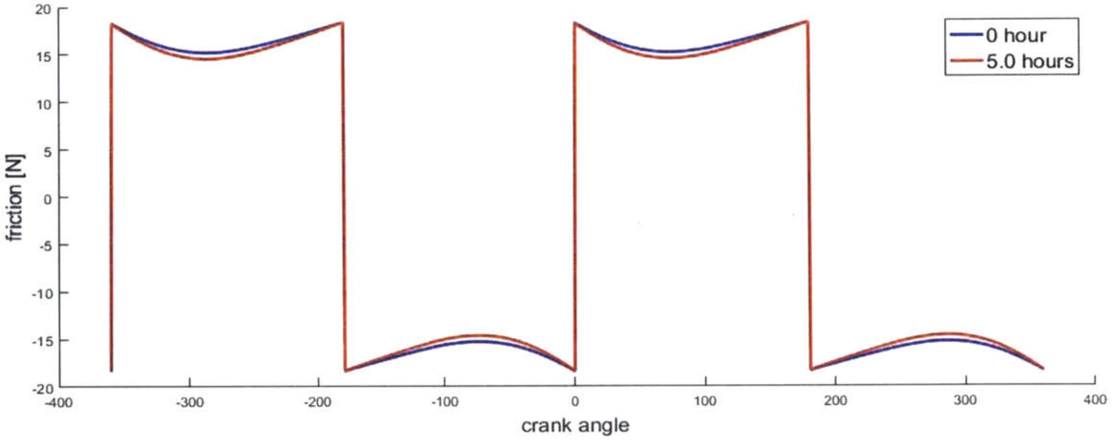

Figure 4.10 Friction of GG07 for the entire engine cycle with speed 500rpm

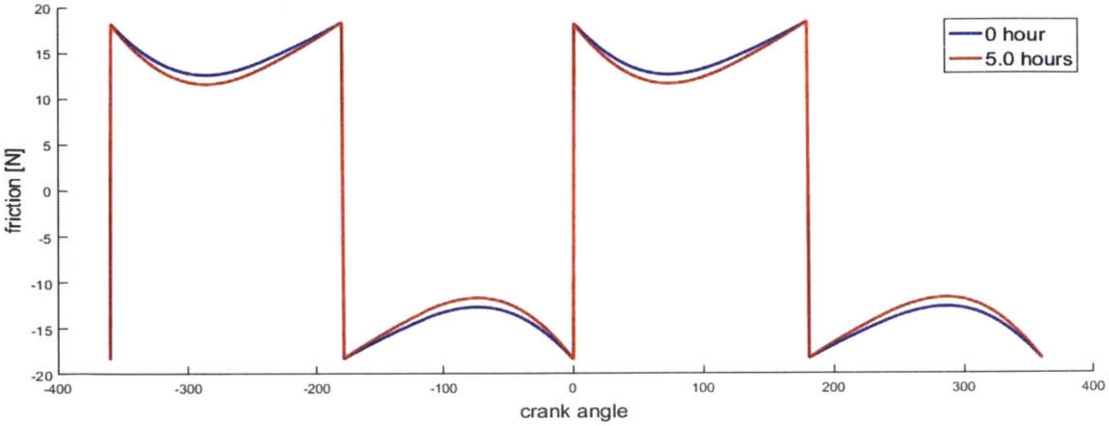

Figure 4.11 Friction of GG07 for the entire engine cycle with speed 1000rpm

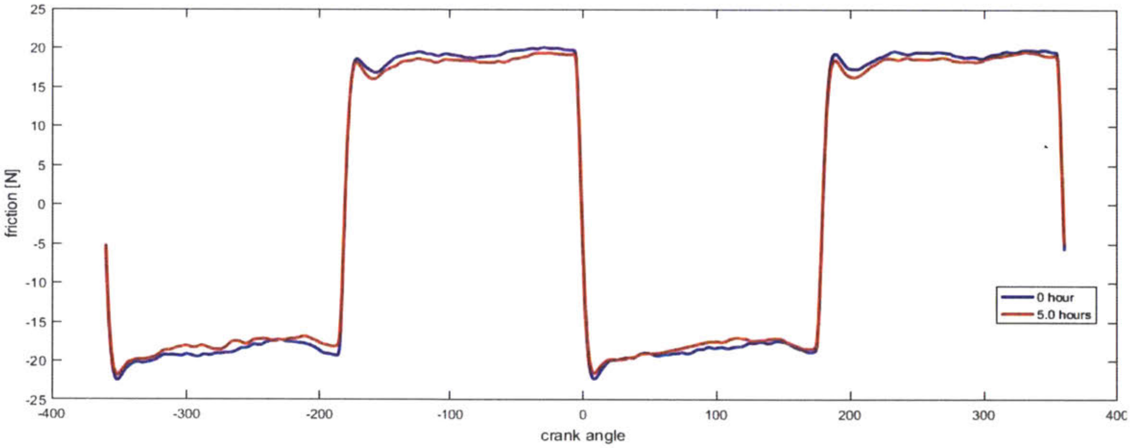

Figure 4.12 Experimental measurements for friction of GG07 with speed 100rpm [39]

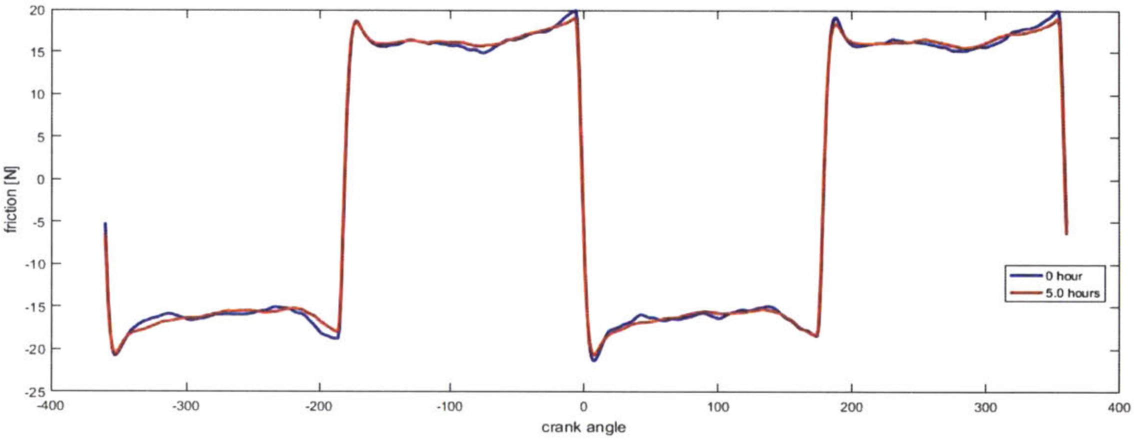

Figure 4.13 Experimental measurements for friction of GG07 with speed 500rpm [39]

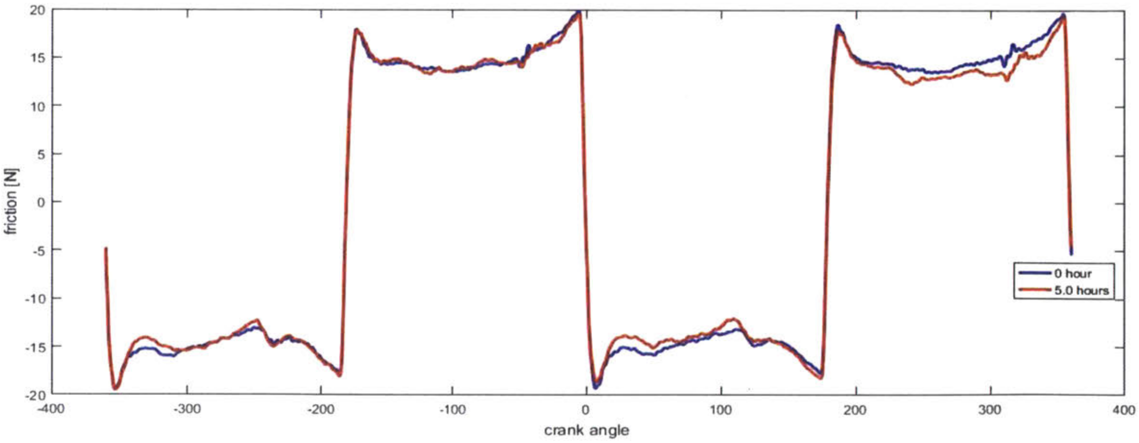

Figure 4.14 Experimental measurements for friction of GG07 with speed 1000rpm [39]

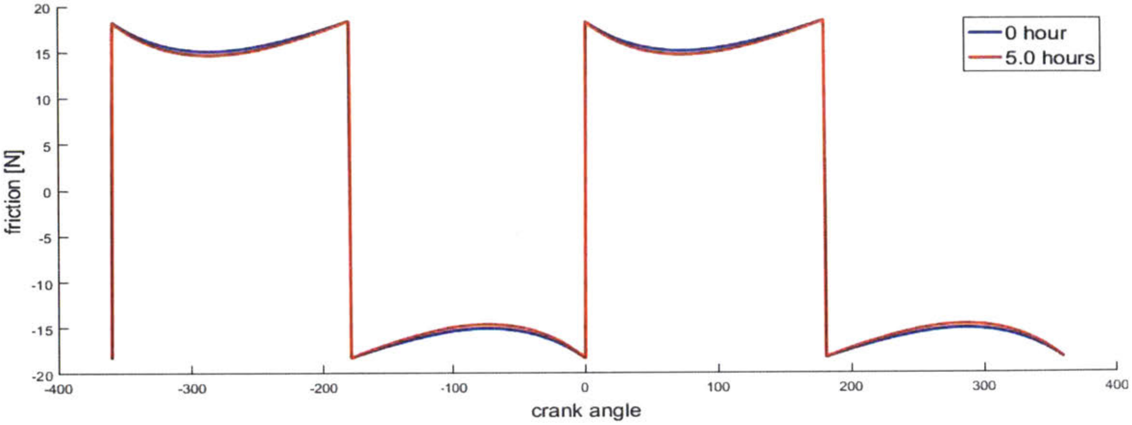

Figure 4.15 Friction of GG09 for the entire engine cycle with speed 100rpm

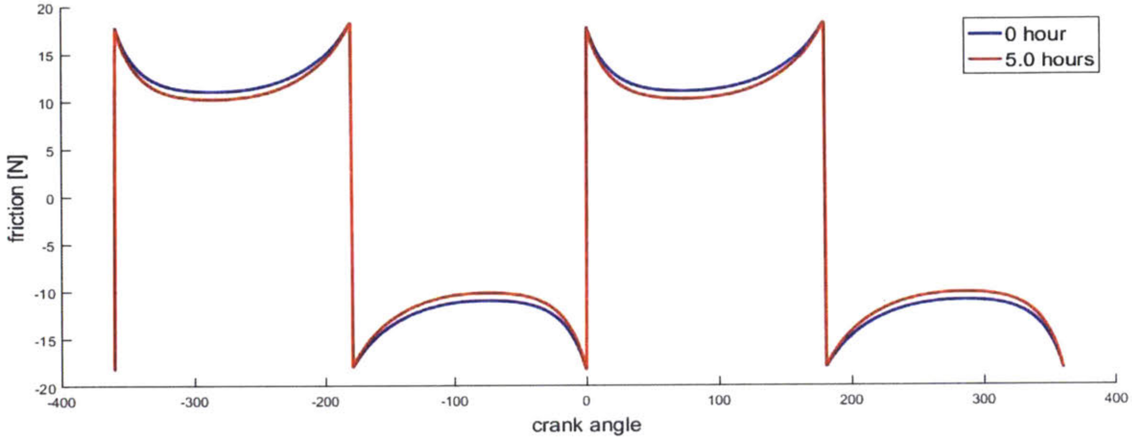

Figure 4.16 Friction of GG09 for the entire engine cycle with speed 500rpm

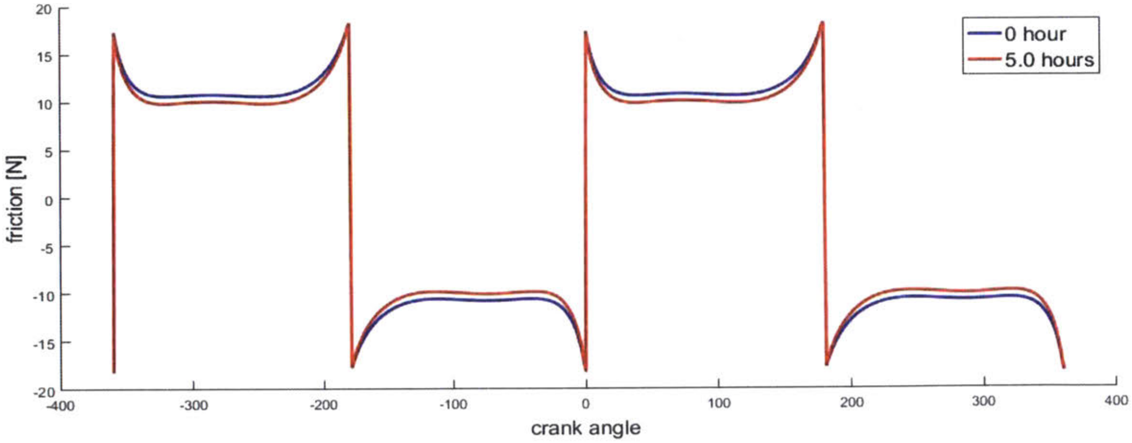

Figure 4.17 Friction of GG09 for the entire engine cycle with speed 1000rpm

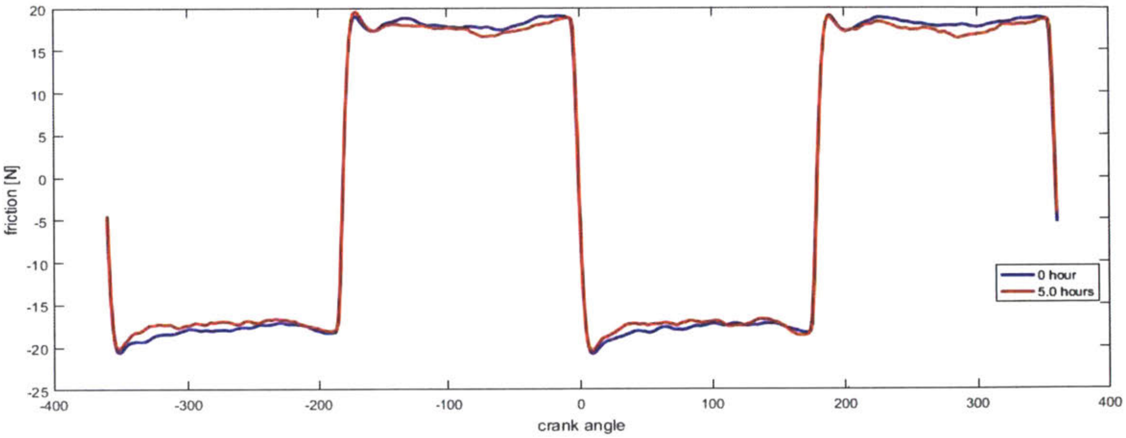

Figure 4.18 Experimental measurements for friction of GG09 with speed 100rpm [39]

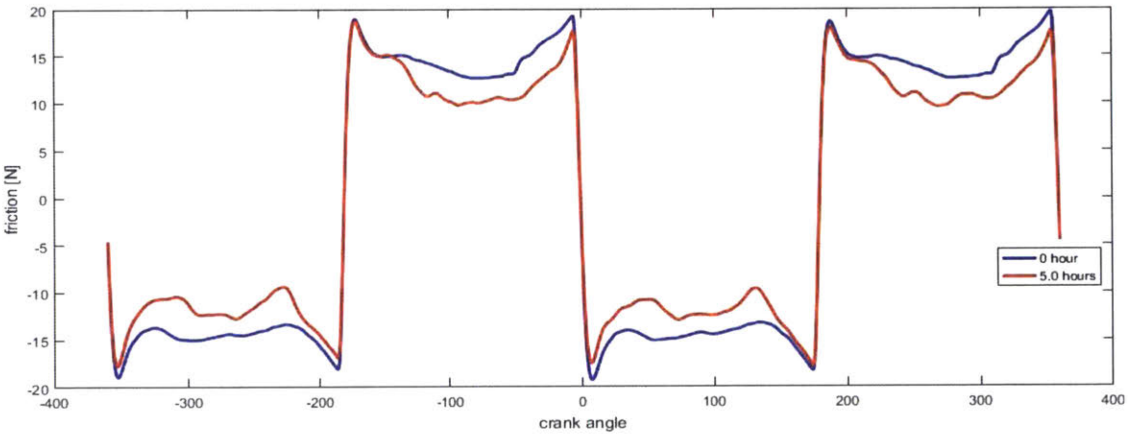

Figure 4.19 Experimental measurements for friction of GG09 with speed 500rpm [39]

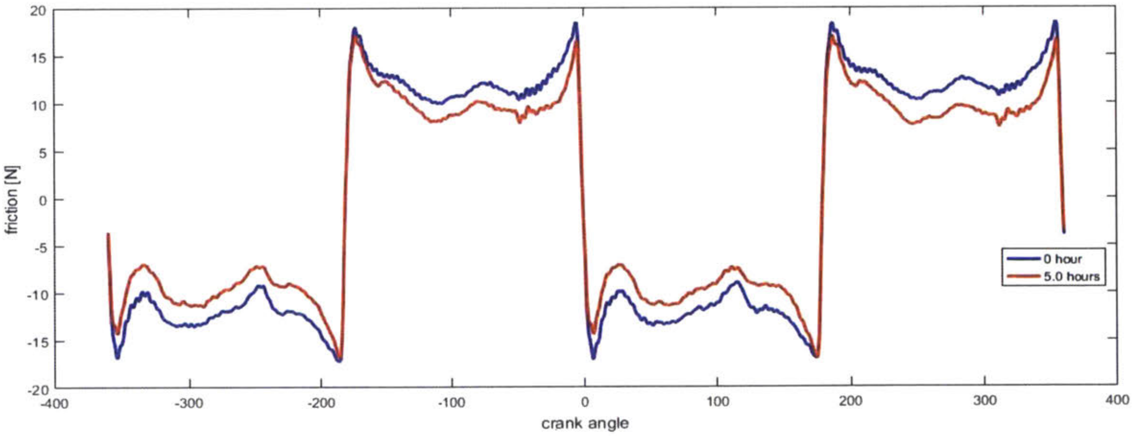

Figure 4.20 Experimental measurements for friction of GG09 with speed 1000rpm [39]

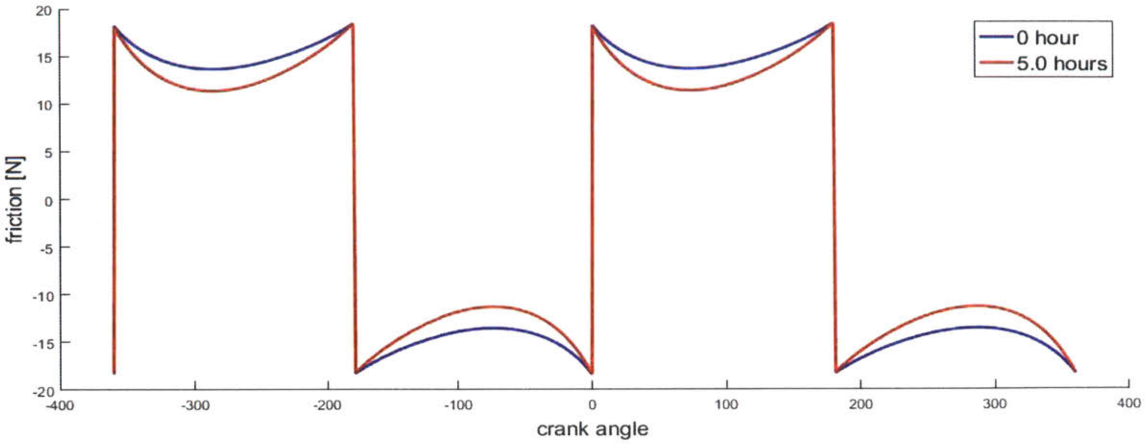

Figure 4.21 Friction of GG21 for the entire engine cycle with speed 100rpm

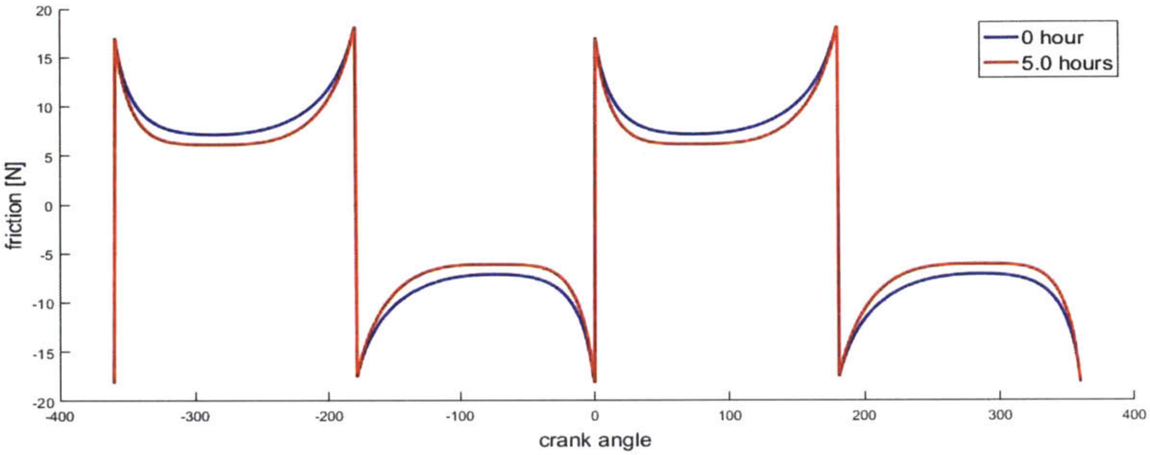

Figure 4.22 Friction of GG21 for the entire engine cycle with speed 500rpm

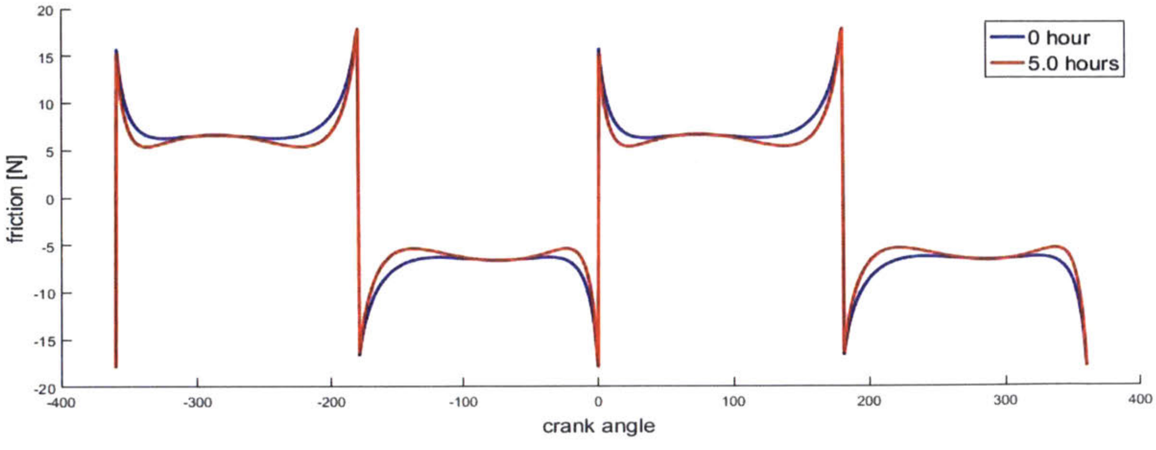

Figure 4.23 Friction of GG21 for the entire engine cycle with speed 1000rpm

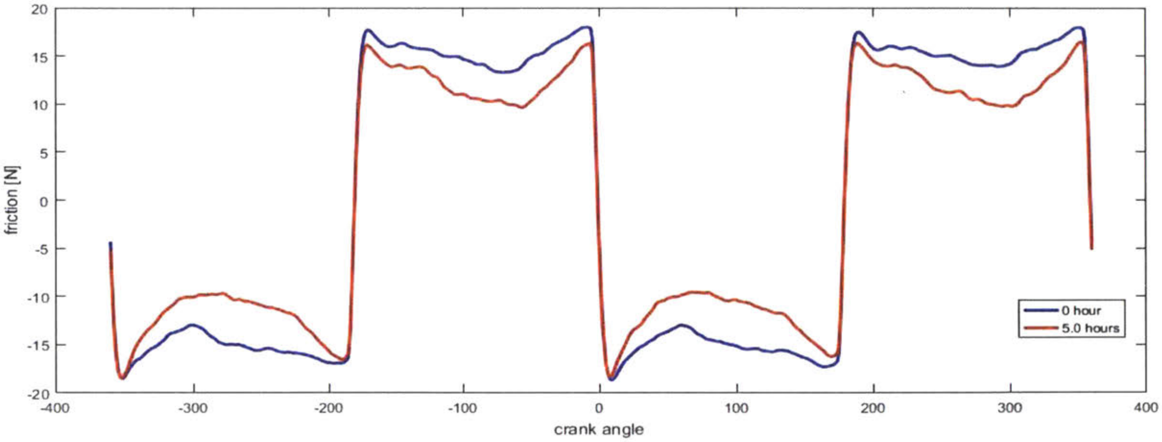

Figure 4.24 Experimental measurements for friction of GG21 with speed 100rpm [39]

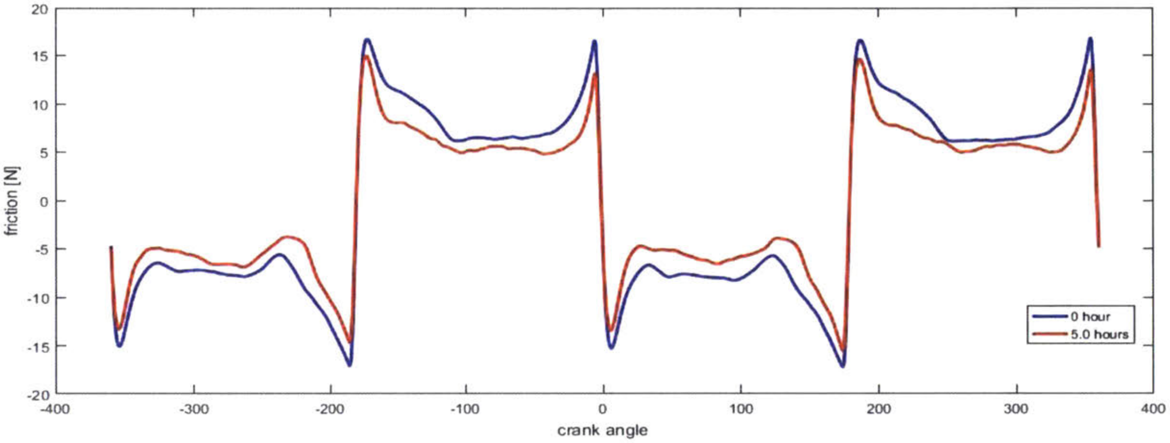

Figure 4.25 Experimental measurements for friction of GG21 with speed 500rpm [39]

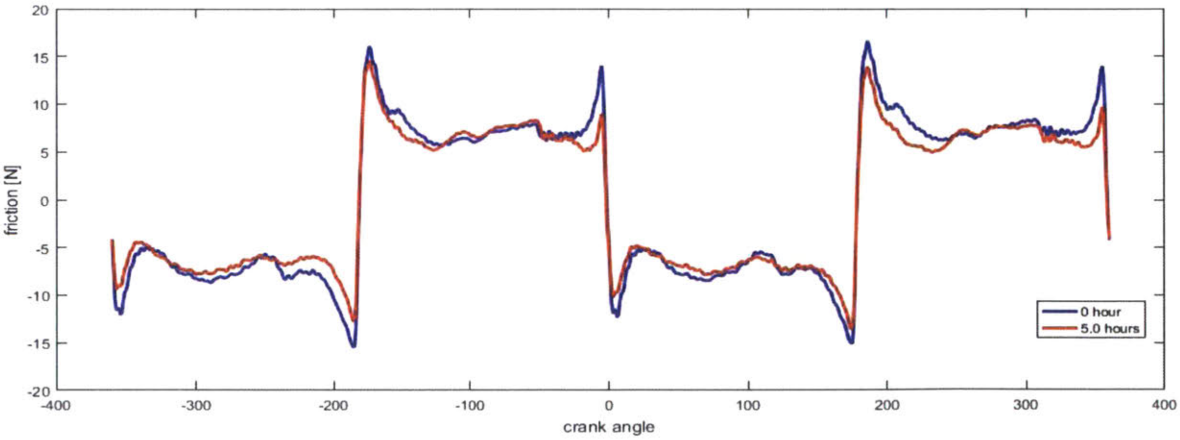

Figure 4.26 Experimental measurements for friction of GG21 with speed 1000rpm [39]

Chapter 5. Initial Work on Third-body Abrasive Wear

Besides surface plastic deformation and fatigue wear, another important wear mechanism is abrasive wear. As sketched in Figure 5.1, abrasive wear can be caused by both two-body contact and third-body particles trapped between sliding surfaces. For a ring-liner wear system, abrasive wear due to third-body particles is dominant compared with two-body abrasive wear, because the ring coating has much smaller roughness than the liner surface. Therefore, third bodies have more significant effect on abrasive wear, while the influence of tiny asperities on the ring surface can be neglected. With the same assumption made in two-body fatigue wear simulation, ring is assumed to be rigid and flat in the abrasive wear simulation of liner in this chapter. Figure 5.2 is an SEM image of the abrasive wear scars of the cast iron flat specimen worn in the M11 HST oil.

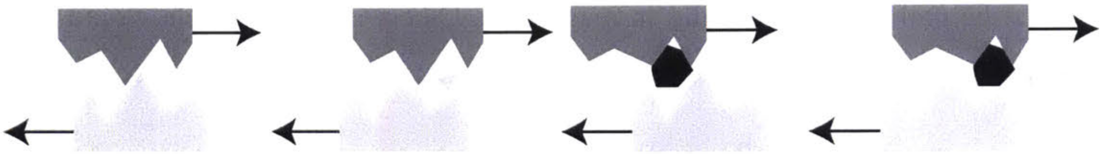

Figure 5.1 two-body and third-body abrasive wear [40]

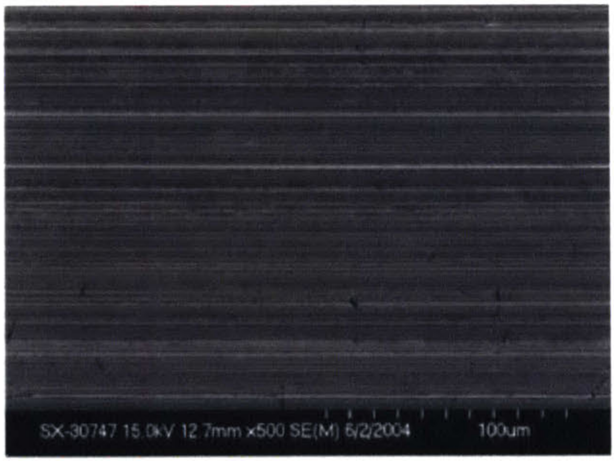

Figure 5.2 SEM image of abrasive wear scars of the cast iron specimen [41]

In this chapter, some initial work of third-body abrasive wear is presented, along with future potential work of this liner wear simulation project. GG30 liner surface is used as a testing surface to combine two-body fatigue wear and third-body abrasive wear simulations and make comparisons. The simulation is based on some third-body wear and transport theories, as introduced in section 5.1 and 5.2.

5.1 Third-body particles transport

Some valuable work of third-body particles transport is completed by former researchers. In this section, two widely accepted transport models are introduced. The first one is the model assuming particles are two-dimensional rhombuses [42]. As shown in Figure 5.3, the longest diagonal of a rhombic particle has a length of D, and the larger interior angle 2β. The particle is trapped between two surfaces, with material hardness H_1 and H_2. For steady state, the external forces exerted by the two surfaces must be collinear and equally in magnitude. Otherwise, the particle would rotate to reach its steady state, where corresponding tilted angle θ can be expressed as [43]:

$$\theta = -2\beta + \cos^{-1}\left(-\frac{h}{D}\tan\beta\right) \qquad \text{(Equation 5.1)}$$

where h is the local clearance between two surfaces.

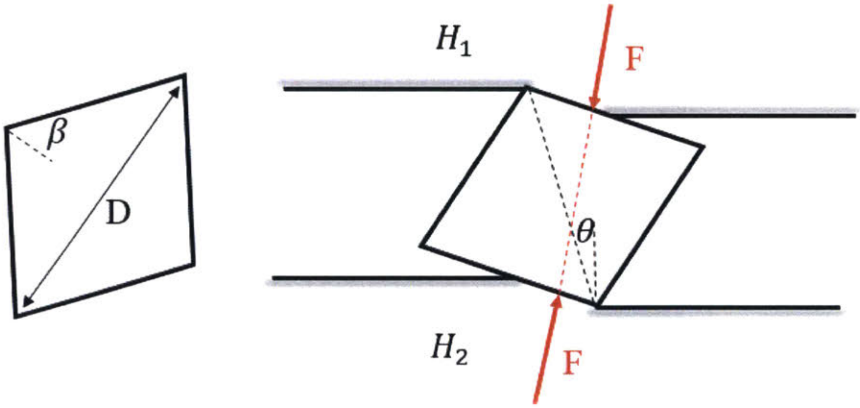

Figure 5.3 The model of two-dimensional rhombus for third-body wear

Based on Equation 5.1 and some other parameters, the particle transport pattern can be classified as follows.

I. $\frac{\pi}{4} \leq \beta \leq \frac{\pi}{3}$

  i. If $\frac{D}{h} \leq \frac{1}{\cos\beta}$: the particle rotates between the two surfaces, causing little damage to both surfaces. No abrasive wear occurs in this case.

  ii. If $\frac{D}{h} > \frac{1}{\cos\beta}$ and $\frac{1}{H} > 4(\cos\beta)^2 - 1$: both surfaces experience abrasive wear as the particle having relative sliding motion against them. $H = \frac{H_{hard}}{H_{soft}}$, defined as the hardness ratio of the sliding pair.

  iii. If $\frac{D}{h} > \frac{1}{\cos\beta}$ and $\frac{1}{H} < 4(\cos\beta)^2 - 1$: the particle is embedded into the softer surface, moving together with the softer surface but causing abrasive wear on the harder surface.

II. $\frac{\pi}{3} < \beta \leq \frac{\pi}{2}$

  i. If $\frac{D}{h} \leq \frac{1}{\cos\beta}$: the particle rotates between the two surfaces.

  ii. If $\frac{D}{h} > \frac{1}{\cos\beta}$: both surfaces experience abrasive wear.

It is easy to see that when β is in the range of $\left(\frac{\pi}{3}, \frac{\pi}{2}\right]$, the particle has no chance to be embedded into one surface. This can be intuitively understood that particles with 'blunt' corners are less likely to become embedded into sliding surfaces.

The second model of third-body particle transport is first developed by Professor Liang Fang in Xi'an Jiao Tong University. In this model assumes to have ellipsoidal or spherical shapes [44][45]. As a simple introduction, only the case with spherical particles is briefly introduced here.

The length parameters in this model are all presented in Figure 5.4. If the friction coefficient between the particle and the surfaces is a constant μ, then the particle rotates if μ is larger than the ratio $\frac{e}{h}$. On the contrary, abrasive wear occurs when μ is smaller or equal to $\frac{e}{h}$, with the particle sliding against worn surfaces. If the normal load on this particle P is known, then all the geometric parameters can be connected into a set of equations.

$$\xi_1 = 1 - \left(1 - \frac{P}{4\pi R^2 H_1}\right)^2 ; \ \xi_2 = 1 - \left(1 - \frac{P}{4\pi R^2 H_2}\right)^2$$

$$\frac{e}{h} = \frac{P}{2\pi^2 R^2 H_1} \frac{\xi_1^{\frac{1}{2}} + \xi_2^{\frac{1}{2}}}{\xi_1^{\frac{3}{2}} + \frac{H_2}{H_1}\xi_2^{\frac{3}{2}}} \qquad \text{(Equation 5.2)}$$

After calculating $\frac{e}{h}$ using Equation 5.2, it is easy to know the particle movement pattern through comparing to friction coefficient μ.

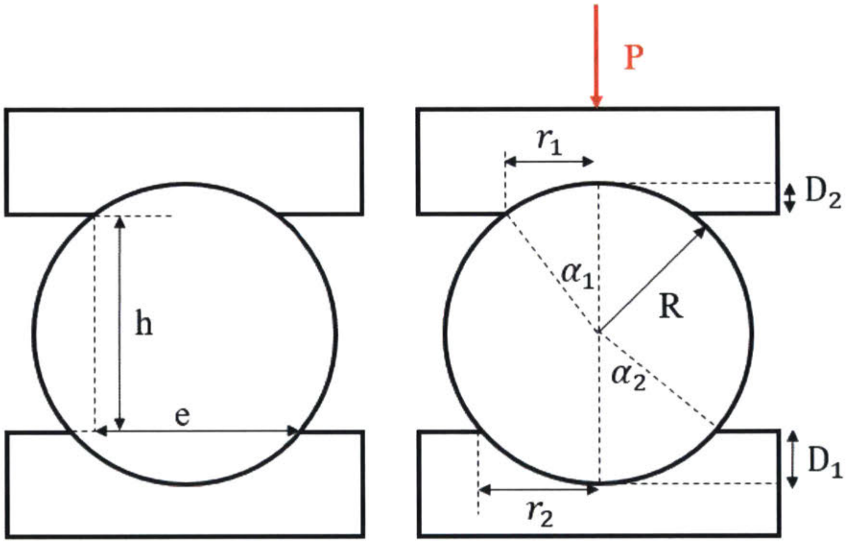

Figure 5.4 The model of a spherical particle for third-body wear

For the initial work of third-body particle transport, these two transport models are not completely adopted because some input parameters are difficult to obtain. In the rhombic particle model, it is hard to define β and D for all third-body particles, derived from fractured asperities. The second spherical particle model is also difficult to use because the load P on each particle is not easy to obtain if only the total load P is known. Solving how to calculate the distribution of the total load on each contact asperity and third-body particle is an important but hard step. Therefore, a simple assumption is made for particles transport simulation: a particle will slides along with the piston ring if the particle diameter is larger than the local clearance. In this case, the particle will cause abrasive wear scars on the liner surface. Otherwise, if the particle diameter is smaller than local clearance, it will just stay on the liner surface, as illustrated in Figure 5.5. This assumption is originated from the second model, simply assuming that $D_1 = D_2 = 0$. Based on this assumption, it can be expected that many particles would fall into honing grooves during sliding process, and this is confirmed from simulation results.

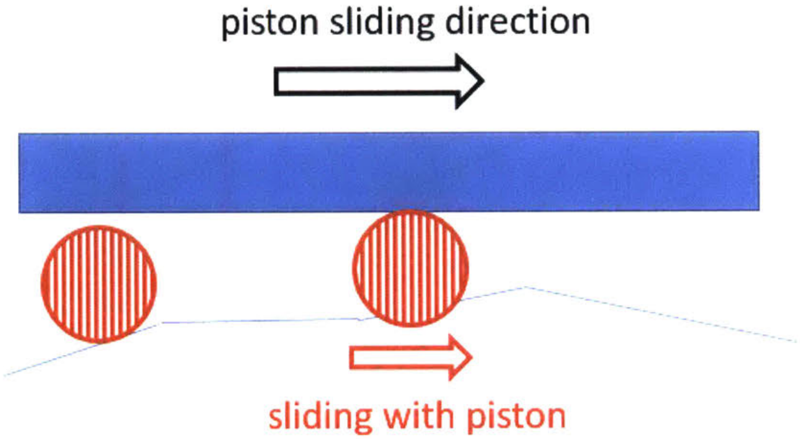

Figure 5.5 Particle transport model used in abrasive wear simulation

5.2 Plowing and cutting effect of third-body particles

As mentioned in the previous section, only sliding motion can cause significant and continuous abrasive wear, leading to third-body scratches on the liner surface. After making reasonable assumptions and getting a simple model for particle transport, it is important to know how a sliding particle performs abrasive wear on the original surface. Modeling of abrasive wear is extremely complex, because many parameters actually can influence the results of abrasion, such as attack angle, penetration depth, particle relative hardness and microstructures of the worn material. However, efficient models can still be established under some assumptions and approximations. Three models are introduced in this section.

The simplest model, illustrated in Figure 5.6, is that of a particle with a conical tip, carrying a normal load P cutting a groove with depth h. the key assumption in this model is that all third-body particles have at least one conical tip and always use their conical tips to cut the surface when they are sliding with the other surface. The material volume loss is also assumed to be equal to the all the overlapping volume during sliding [46].

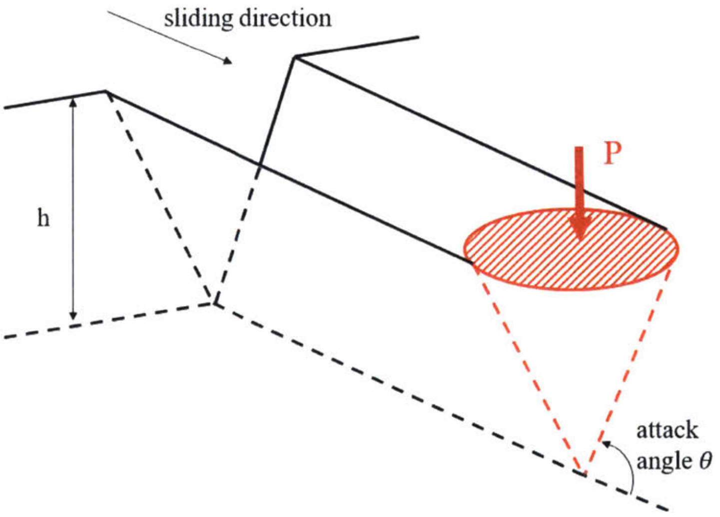

Figure 5.6 Third-body cutting model for a particle with a conical tip

Under this simplest situation, the abrasive wear rate of a single particle can be expressed as:

$$\text{wear rate} = \frac{2\tan\theta}{\pi}\frac{Pv}{h} \qquad \text{(Equation 5.3)}$$

In Equation 5.3, v is the particle sliding speed. Thus we have an 'Archard's law' for abrasive wear, with the wear coefficient $k = \frac{2\tan\theta}{\pi}$. Particles with blunt tips, will have larger values of θ and so will be expected to cause more wear damage [47]. However, the limitations for the use of this simple wear model are also obvious. As mentioned in section 5.1, it is still not clear how to obtain the normal load P on each third-body particle, leaving Equation 5.3 too many unknowns. The second limitation is that this model only takes cutting effect into consideration, but simply neglects plowing effect. When third-body particles are sliding between two surfaces, a portion of original material in wear grooves is squeezed to two sides, instead of being completely removed due to particle cutting.

A better model can integrate cutting and plowing into a bigger structure. As sketched in Figure 5.7, the ratio of volume of material removed as wear debris to the volume of the wear groove can be mathematically described by the parameter f_{ab}, which is defined through the following equation [48][49]:

$$f_{ab} = \frac{A_v - (A_1 + A_2)}{A_v} \qquad \text{(Equation 5.4)}$$

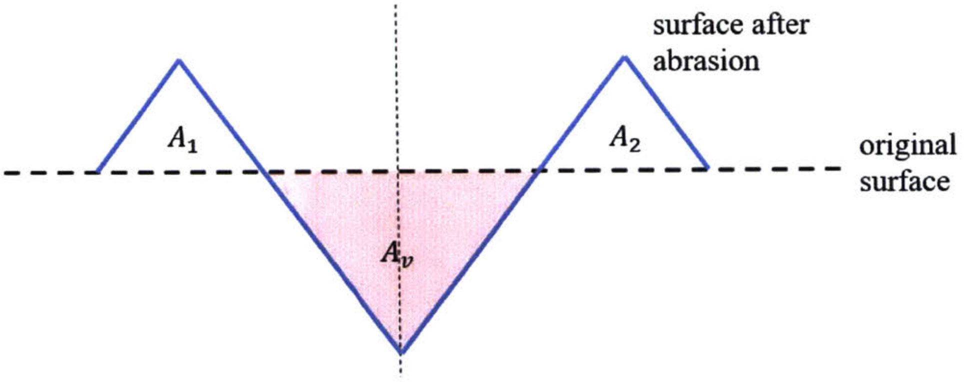

Figure 5.7 The cross section of a third-body wear groove

where A_v is the cross-sectional area of the groove and $(A_1 + A_2)$ is the cross-sectional area of the material being pushed to the two sides. From the material aspect, the ratio f_{ab} can be expressed as [48]:

$$f_{ab} = 1 - \left(1 - \frac{1}{\beta}\ln\left(\frac{\varphi_s}{\varphi_{lim}}\right)\right)^2 \qquad \text{(Equation 5.5)}$$

where φ_s is the deformation on wearing surface and φ_{lim} is the corresponding upper limit of surface deformation. β is defined as a work-hardening parameter $\beta = \sqrt[3]{\frac{H_{def}}{H}}$, as a function of surface material hardness H and hardness of highly deformed wear debris H_{def}. With equation 5.4 and 5.5, this abrasive wear model can simulate both cutting and plowing effect of third-body abrasive particles.

The model used in this project also considers both particles' cutting and plowing as the previous model does. However, particles are assumed to be perfect spheres. According to contact mode and geometric properties of wear grooves, abrasive wear of particles is classified to three categories.

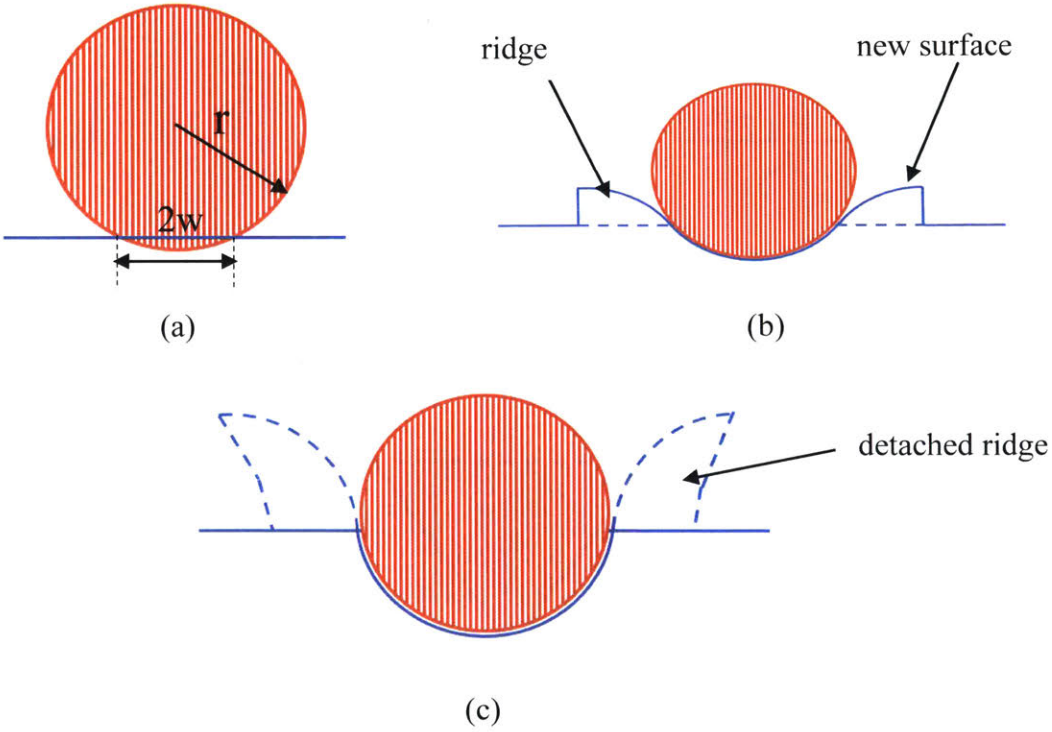

(a) Elastic contact (b) Plastic plowing with ridges formed on two sides

(c) Particle cutting with ridges all fractured

Figure 5.8 Three categories of abrasive wear of hard spherical particles

Figure 5.8 shows the cross section of all three categories, in which r is the radius of the spherical particle and w is the half contact width. Different abrasion categories are divided through the range of $\frac{w}{r}$:

I. If $\frac{w}{r} < 0.28$:

The particle moves along with the piston ring, but no abrasive wear scar is left because the contact is purely elastic.

II. If $0.28 \le \frac{w}{r} < 0.87$:

The particle is plowing the surface, pushing the overlapping volume to two sides of the groove due to plastic deformation and resulting abrasive wear.

III. $\frac{w}{r} \ge 0.87$:

The third-body particle is cutting the original surface, with ridges on the two sides all fractured.

With appropriate models for particle transport and third-body abrasive wear, we can perform simulations for third-body wear and investigate some underlying correlations.

5.3 Simulation results for third-body abrasive wear

GG 30 is used as the testing surface finish for third-body abrasive wear simulation, with different external normal pressures, 1MPa and 2MPa. The simulation is the combination of surface plastic flattening, fatigue wear and third-body abrasion. Except for abrasive wear, all other simulations steps are the same as fatigue wear simulation introduced before. External pressures are kept the same during the entire simulation time period. It is important to point out some essential assumptions for simulations of abrasive wear. First, every third-body particle is derived from one fractured asperity, without any agglomeration or break-up. This naturally results that the number of particles equals to the number of asperities fractured until this simulation epoch. The assumption also indicates that soot particles are not considered here although it is one of the major source of wear particles. The second major assumption is that third-body particles are perfectly spheres and rigid. This assumption eliminates the possible deformations of particles during wear. The simulation results may differ from experimental results because the two major assumptions can introduce some inconsistence with real situations, but we can still do some inspection and extract some useful information from the simulation results.

Fig 5.9 – 5.14 are the plots for third-body particle positions during the entire wear of 1×10^6 running cycles when the external pressure is 1MPa. The number of particles increases with time as more contact asperities becomes fractured due to fatigue wear. The interesting thing is that as the number of particles increases, particles are gradually concentrated in honing grooves, because the local clearance of grooves is larger than clearance of plateau part. Therefore, particles have higher chance to be trapped in grooves rather than continuously scratching. This can also be reflected from the surface topology change in Figure 5.15 –5.20. Abrasive scratches are generated due to sliding particles, with many of them ending in grooves.

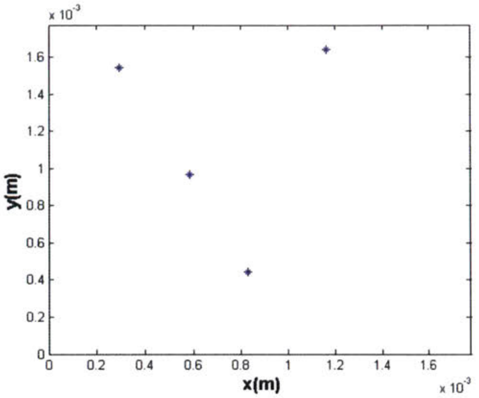

Figure 5.9 Particles after 5×10^3 cycles

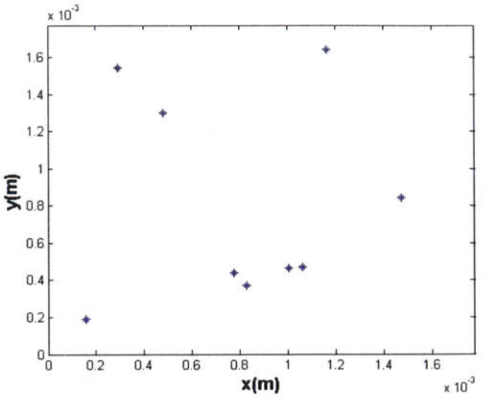

Figure 5.10 Particles after 1×10^4 cycles

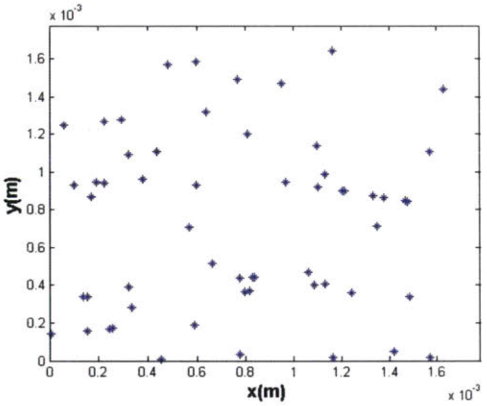

Figure 5.11 Particles after 5×10^4 cycles

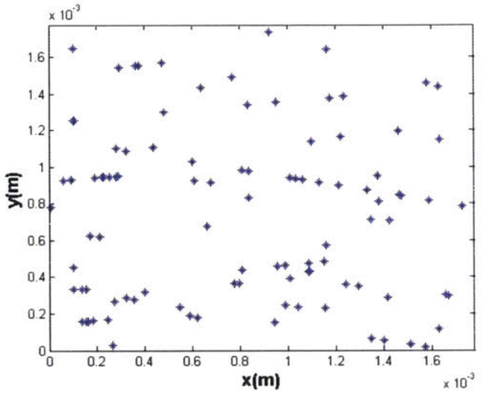

Figure 5.12 Particles after 1×10^5 cycles

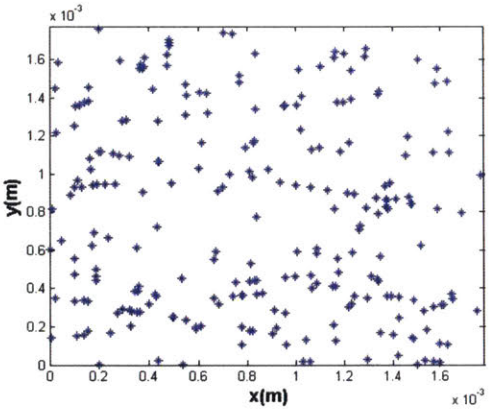

Figure 5.13 Particles after 5×10^5 cycles

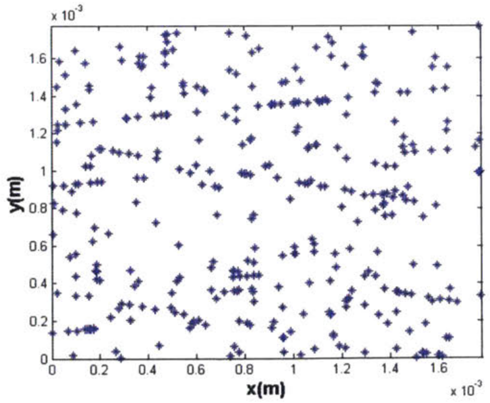

Figure 5.14 Particles after 1×10^6 cycles

Figure 5.9 – Figure 5.14 Particle positions change under normal stress 1MPa

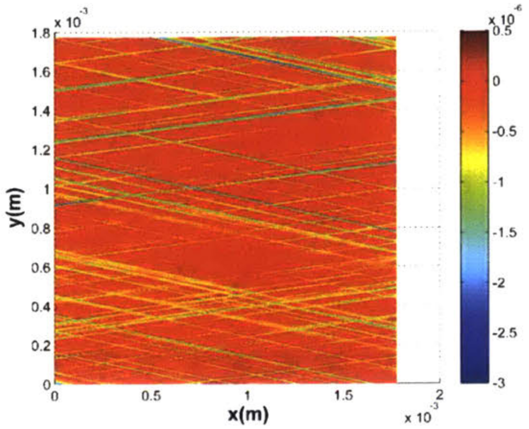

Figure 5.15 Surface after 5×10^3 cycles

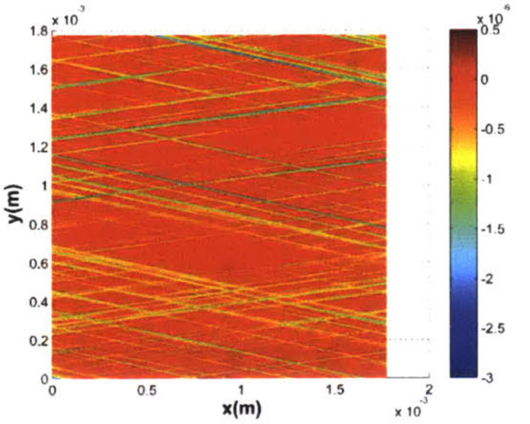

Figure 5.16 Surface after 1×10^4 cycles

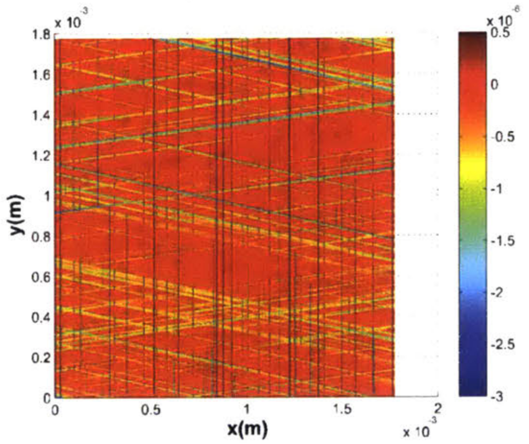

Figure 5.17 Surface after 5×10^4 cycles

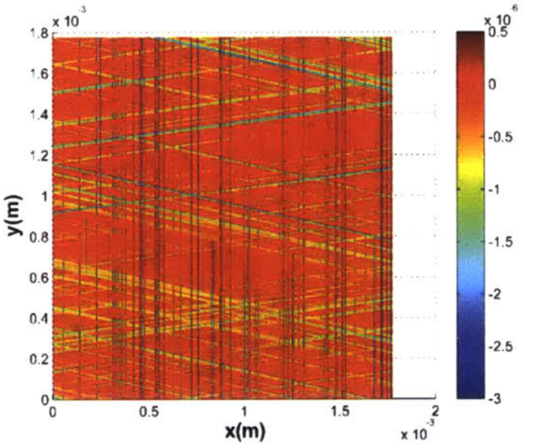

Figure 5.18 Surface after 1×10^5 cycles

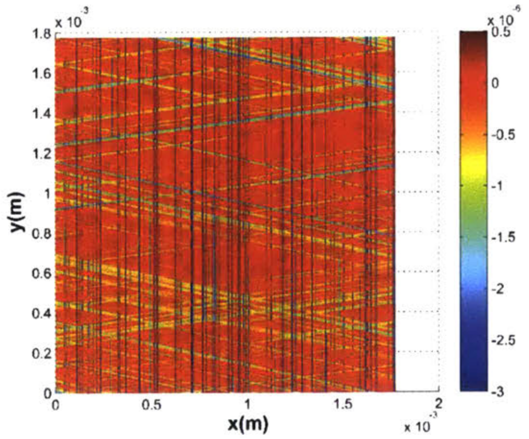

Figure 5.19 Surface after 5×10^5 cycles

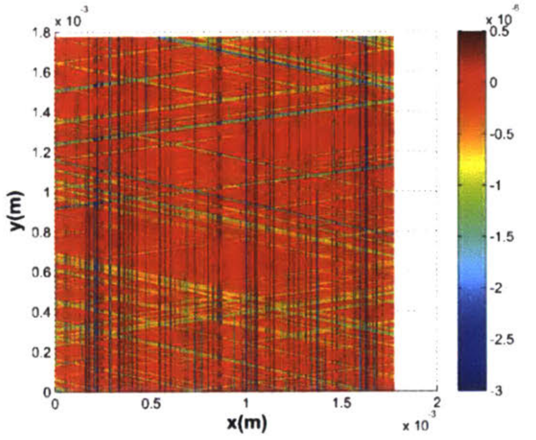

Figure 5.20 Surface after 1×10^6 cycles

Figure 5.15 – Figure 5.20 Liner surface topology change under normal stress 1MPa

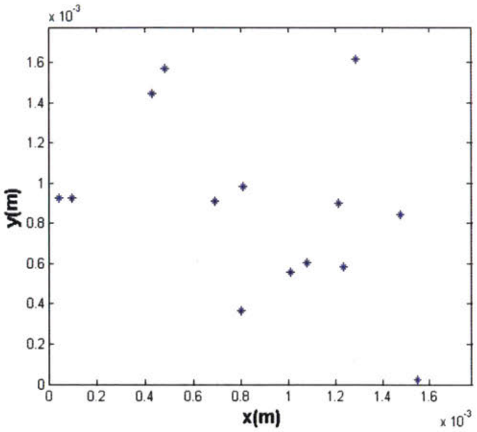

Figure 5.21 Particles after 5 × 10^3 cycles

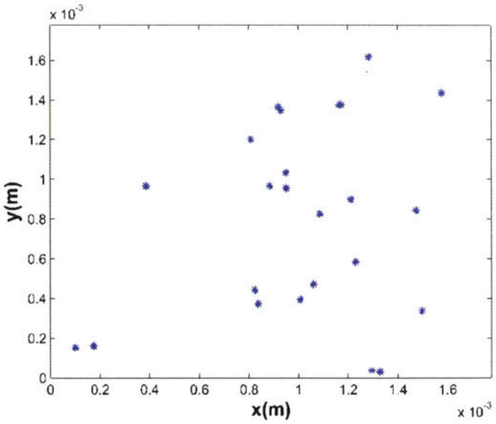

Figure 5.22 Particles after 1 × 10^4 cycles

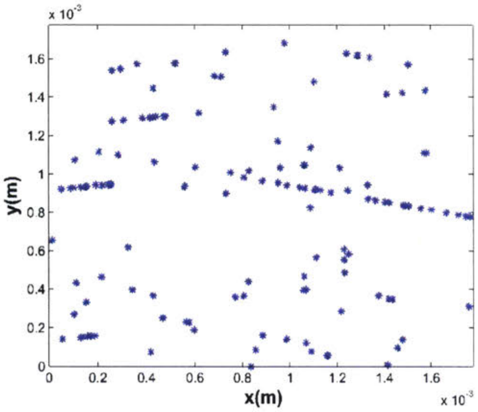

Figure 5.23 Particles after 5 × 10^4 cycles

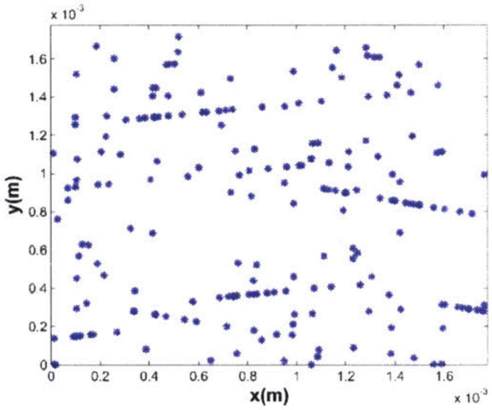

Figure 5.24 Particles after 1 × 10^5 cycles

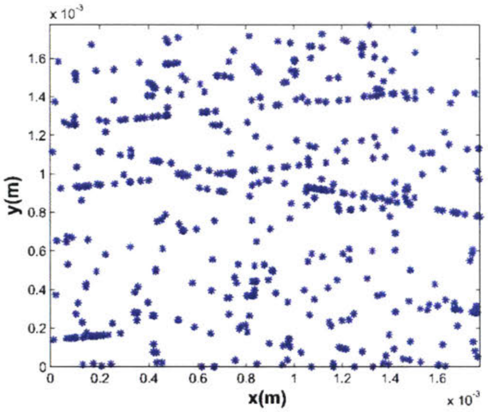

Figure 5.25 Particles after 5 × 10^5 cycles

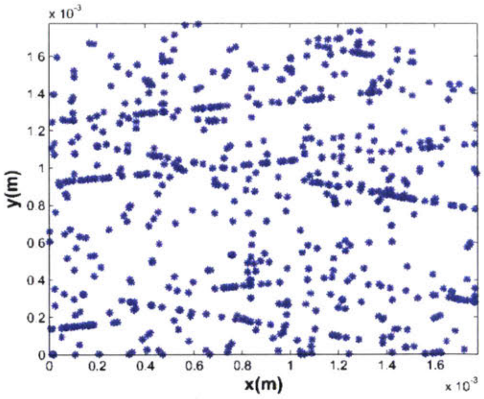

Figure 5.26 Particles after 1 × 10^6 cycles

Figure 5.21 – Figure 5.26 Particle positions change under normal stress 2MPa

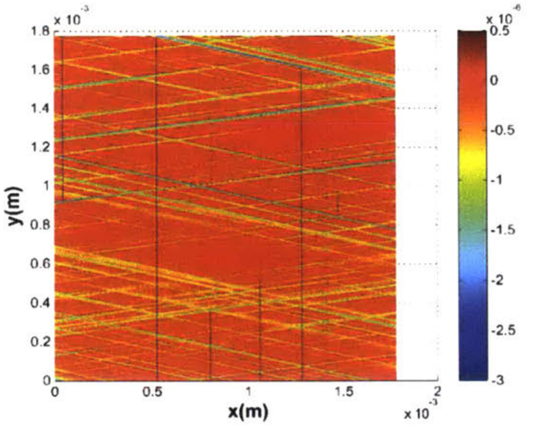

Figure 5.27 Surface after 5×10^3 cycles

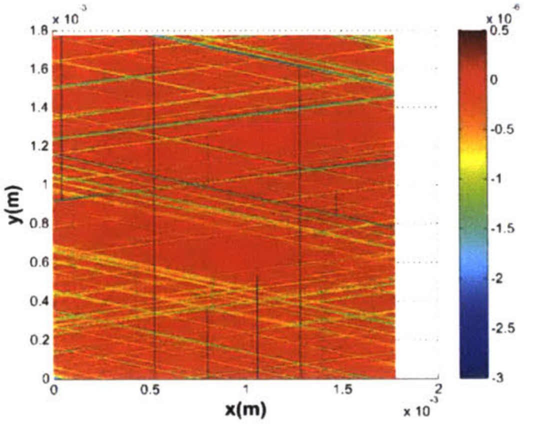

Figure 5.28 Surface after 1×10^4 cycles

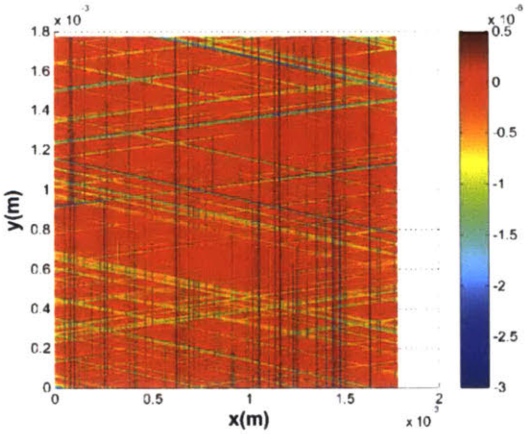

Figure 5.29 Surface after 5×10^4 cycles

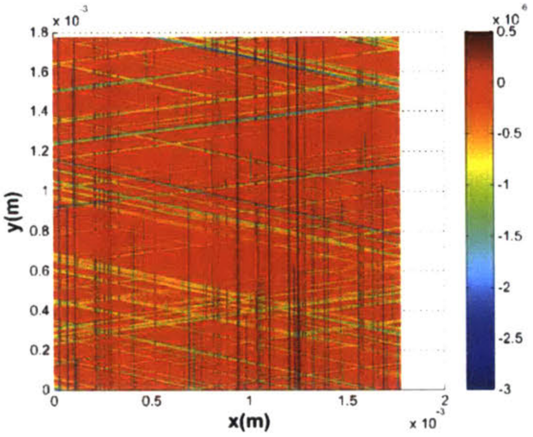

Figure 5.30 Surface after 1×10^5 cycles

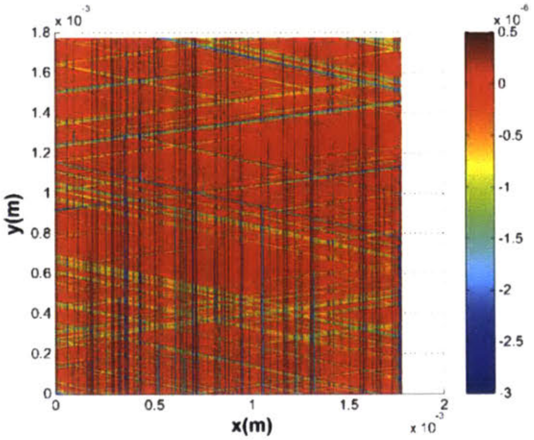

Figure 5.31 Surface after 5×10^5 cycles

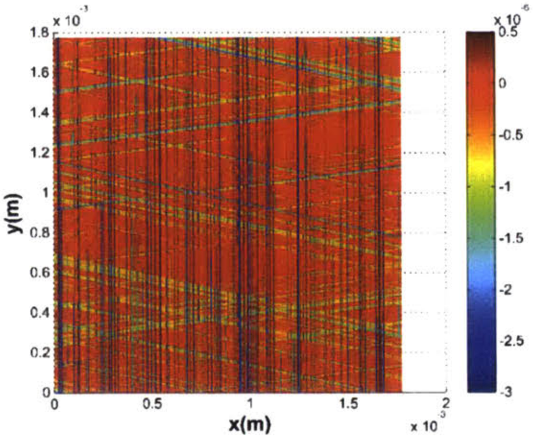

Figure 5.32 Surface after 1×10^6 cycles

Figure 5.27 – Figure 5.32 Liner surface topology change under normal stress 2MPa

The simulation results show that honing structure on the liner surface can prevent particles causing continuous abrasive wear since it can trap particles and stop them when they are sliding. However, honing grooves cannot prevent wear scars caused by some extremely large particles, leaving them always sliding against the liner surface and creating continuous scratches throughout the entire simulated surface region, as shown in Figure 5.20 and Figure 5.32.

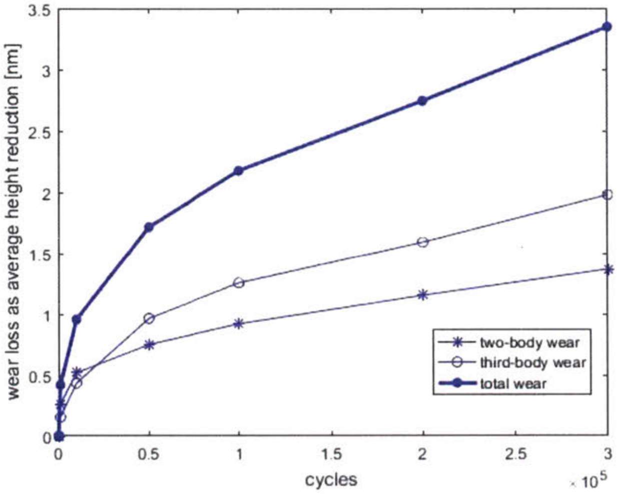

Figure 5.33 Two-body and third-body wear loss for external pressure 1MPa

Figure 5.33 is the plot of two-body wear loss, third-body wear loss and total wear loss when the external normal pressure is 1 MPa. Both wear mechanisms experience a break-in period, before goes into steady wear state. The break-in period of third-body wear is slightly longer than that of two-body fatigue, because all particles are formed from fractured asperities. Therefore, at the beginning 2.5×10^4 cycles, volume loss due to two body wear is larger than the loss of third-body abrasion. However, as the wear process enters to the steady state, wear rate of third-body wear is larger than that of two-body wear, because large particles are always trapped between sliding surfaces while asperity fracture only occurs as a discrete process.

The potential future work includes simulating soot particle transport and agglomeration process and using some parameters, like aspect ratio, to put the shape of particles into the simulation model. These work would be helpful to improve the efficiency of simulating liner wear process.

Chapter 6. Conclusion and Future Work

6.1 Summary and main findings

In this work, a model of two-body contact, fatigue dominated wear of cylinder liner in internal combustion engines is established and a simple model of third-body abrasive wear is also developed. Three different mechanisms leading to liner surface has been studied: surface plastic deformation, fatigue wear and third-body particle abrasion. Meanwhile, some underlying correlations are studied based on the simulation results, which may provide guidance for liner surface manufacturing and engine lubrication.

In Chapter 2, the effect of liner surface plastic flattening is discussed and modeled. Both experiments and simulations reveal that this mechanism is the dominated wear mechanism at the beginning and the major contribution for transient wear. During the first several cycles, the liner surface is significantly flattened, leading to the transition for most asperities from plastic contact to elastic contact.

In Chapter 3, fatigue wear model is established based the theory of delamination wear. Simulation results agree with Archard's wear law that for a specific liner surface finish, the steady state wear rate is proportional to external normal load. However, this proportional correlation is only valid for a surface within a certain roughness range. Otherwise, if the surface asperities are too flat, subsurface cracks can hardly be generated due to low contact pressure, leading to zero fatigue wear. Simulations also indicate that the maximum steady state wear rate can be obtained for a specific surface roughness. This may be applied in the future for liner surface design to minimize the break-in time.

The functional change due to the wear on liner roughness using the model developed here shows the same trend on liner finish dependency and running time as the results obtained with the floating liner engine previously. The liner finish with smoother plateau exhibits faster breakin than the rougher liner. Moreover, the evolution of the friction predicted is comparable to the measurement in magnitude, implying the potential of the model in predicting duration of the break-in period and asymptotic friction.

Initial work for simulations of third-body abrasive wear shows that third-body can cause continuous wear, leading to higher steady state wear rate than fatigue wear does. The detailed correlations of third-body still need further investigation.

6.2 Potential future work

The future work basically includes the following three parts: modeling third-body particle transport and agglomeration, modeling formation and removal of tribo-layer, and providing guidance for liner surface manufacturing. So far, the third-body wear model does not include soot particles. The complexity of transport and agglomeration of soot particles plays an essential role in third-body wear. In addition, the current wear model can only deal with material removal process during wear, but in real situations tribo-layer is gradually built, protecting the original surface. Finally, analyzing simulation results of the wear model is expected to find some critical parameters, which can provide some guidance for liner surface design, in order to achieve the purpose anti-wear and efficient lubrication.

Reference

[1] Richardson, D.E., "Review of Power Cylinder Friction for Diesel Engines", ASME Journal of Engineering for Gas Turbines and Power, 2000.

[2] L. Sabri, S.Mezghani, M. El Mansori, H. Zahouani, "Multiscale Study of Finish-Honing Process in Mass Production of Cylinder Liner", Wear, March 2010.

[3] D. Lawrence, "An Accurate and Robust Method for the Honing Angle Evaluation of Cylinder Liner Surface Using Machine Vision", Int. J. Adv. Manuf. Technol., 2011.

[4] Nam P. Suh, "Tribophysics", Massachusetts Institute of Technology, 1986.

[5] Tian Tian, "Oil Transport and Oil Consumption Connecting Different Scales".

[6] Mobarak, H. M., H. H. Masjuki, E. Niza Mohamad, SM Ashrafur Rahman, K. A. H. Al Mahmud, M. Habibullah, and S. Salauddin. "Effect of DLC coating on tribological behavior of cylinder liner-piston ring material combination when lubricated with Jatropha oil.", 2014.

[7] Reizer, Rafal, Pawel Pawlus, Lidia Galda, Wieslaw Grabon, and Andrzej Dzierwa. "Modeling of worn surface topography formed in a low wear process." Wear, 2012.

[8] Chen H., "Modeling of Liner Finish Effects on Oil Control Ring Lubrication in Internal Combustion Engines Based on Deterministic Method", Massachusetts Institute of Technology, Cambridge, USA, 2008.

[9] Giorgio, Massimiliano, Maurizio Guida, and Gianpaolo Pulcini. "Stochastic processes for modeling the wear of marine engine cylinder liners." In Statistics for Innovation, 2009.

[10] Stachowiak, Gwidon, and Andrew W. Batchelor. "Engineering tribology". Butterworth-Heinemann, 2013.

[11] Rigo, Jürgen, and Paul Feinle. "SRV Tribometer." In Encyclopedia of Lubricants and Lubrication, pp. 1949-1956. Springer Berlin Heidelberg, 2014.

[12] Obert, Petra, Torben Müller, Hans-Jürgen Füßer, and Dirk Bartel. "The influence of oil supply and cylinder liner temperature on friction, wear and scuffing behavior of piston ring cylinder liner contacts–A new model test." Tribology International, 2016.

[13] Kao, W. H., Y. L. Su, J. H. Horng, S. H. Yao, and H. C. Huang. "The tribological properties of Zr/aC: Zr/Zr-C: H-x films with various pulsed-direct current power frequency sliding against various normal loading." Materials Research Innovations, 2015.

[14] Fernández-Pérez, Xana, Amaya Igartua, Roman Nevshupa, Patricio Zabala, Borja Zabala, Rolf Luther, Flavia Gili, and Claudio Genovesio. "Innovative "Green" Tribological Solutions for Clean Small Engines." 2013.

[15] Vorburger, Theodore V., H-G. Rhee, Thomas B. Renegar, J-F. Song, and A. Zheng. "Comparison of optical and stylus methods for measurement of surface texture." The International Journal of Advanced Manufacturing Technology, 2007.

[16] Qing Zhao, "Modeling of Contact between Liner Finish and Piston Ring in Internal Combustion Engines Based on 3D Measured Surface", Massachusetts Institute of Technology, 2014.

[17] Renze Wang, "Numerically Generating Topology of the Liner Finish in Internal Combustion Engines", Massachusetts Institute of Technology, 2014.

[18] D. Semwogerere, E. R. Weeks, "Confocal Microscopy", Encyclopedia of Biomaterials and Biomedical Engineering, 2013.

[19] Maietta, David M., and L. Chang. "An asperity microcontact model incorporating the transition from elastic deformation to fully plastic flow", 2000.

[20] Andersson, Sören, Anders Söderberg, and Ulf Olofsson. "A random wear model for the interaction between a rough and a smooth surface." Wear, 2008.

[21] Johnson, Kenneth Langstreth, and Kenneth Langstreth Johnson. "Contact mechanics" Cambridge university press, 1987.

[22] Zach Westerfield, “A Study of the Friction of the Power Cylinder System in Internal Combustion Engines using a Floating Liner Engine”, Master Thesis, Massachusetts Institute of Technology, 2015.

[23] Mercedez-Benz, "Honen von Zylinder-Laufflachen," 2008.

[24] Greenwood, J. A., and J. B. P. Williamson. "Contact of nominally flat surfaces." In Proceedings of the Royal Society of London A: Mathematical, Physical and Engineering Sciences, 1966.

[25] Suh, Nam P. "An overview of the delamination theory of wear." Wear, 1977.

[26] Fang, Liang, X. L. Kong, J. Y. Su, and Q. D. Zhou. "Movement patterns of abrasive particles in three-body abrasion." Wear, 1993.

[27] De Pellegrin, D. V., and G. W. Stachowiak. "Simulation of three-dimensional abrasive particles." Wear, 2005.

[28] Kusano, Yukihiro, and I. M. Hutchings. "Modelling the entrainment and motion of particles in a gap: application to abrasive wear." Proceedings of the Institution of Mechanical Engineers, Part J: Journal of Engineering Tribology, 2003.

[29] Alabeedi, K. F., J. H. Abboud, and K. Y. Benyounis. "Microstructure and erosion resistance enhancement of nodular cast iron by laser melting." Wear, 2009.

[30] Jahanmir, S., and N. P. Suh. "Mechanics of subsurface void nucleation in delamination wear." Wear, 1977.

[31] Collini, L., G. Nicoletto, and R. Konečná. "Microstructure and mechanical properties of pearlitic gray cast iron." Materials Science and Engineering, 2008.

[32] Goodrich, George M. "Cast iron microstructure anomalies and their cause." AFS Transactions, 1997.

[33] Paris, Paul C., Mario P. Gomez, and William E. Anderson. "A rational analytic theory of fatigue." The trend in engineering, 1961.

[34] Paris, Paul Croce, and Fazil Erdogan. "A critical analysis of crack propagation laws." ASME, 1963.

[35] Archard, J. F., and W. Hirst. "The wear of metals under unlubricated conditions." In Proceedings of the Royal Society of London A: Mathematical, Physical and Engineering Sciences, 1956.

[36] Archard, JeFoa. "Contact and rubbing of flat surfaces." Journal of applied physics, 1953.

[37] Haijie Chen, "Modeling the lubrication of the piston ring pack in internal combustion engines using the deterministic method", Ph.D. Thesis, Massachusetts Institute of Technology, 2011.

[38] Aral, Takayuki, Yoichi Kobayashi, and Shunichi Aoyama. "Numerical simulation of piston ring in mixed lubrication—a nonaxisymmetrical analysis." Journal of tribology, 1994.

[39] Kai Liao, "Factors affecting piston ring friction", Ph.D. Thesis, Massachusetts Institute of Technology, 2013.

[40] Michael Barrett. "An effective program can increase the reliability and availability of machinery while minimizing maintenance costs." Pumps and systems,

http://www.pumpsandsystems.com/pumps/november-2015-get-most-lubricants-through-quality-oil-analysis

[41] Truhan, John J., Jun Qu, and Peter J. Blau. "The effect of lubricating oil condition on the friction and wear of piston ring and cylinder liner materials in a reciprocating bench test." Wear, 2005.

[42] Williams, J. A., and A. M. Hyncica. "Mechanisms of abrasive wear in lubricated contacts." Wear, 1992.

[43] Kusano, Yukihiro, and I. M. Hutchings. "Modelling the entrainment and motion of particles in a gap: application to abrasive wear." Proceedings of the Institution of Mechanical Engineers, Part J: Journal of Engineering Tribology, 2003.

[44] Fang, Liang, X. L. Kong, J. Y. Su, and Q. D. Zhou. "Movement patterns of abrasive particles in three-body abrasion." Wear, 1993.

[45] Fang, Liang, Jia Zhao, Bo Li, and Kun Sun. "Movement patterns of ellipsoidal particle in abrasive flow machining." Journal of Materials Processing Technology, 2009.

[46] Suh, Nam P. "New theories of wear and their implications for tool materials." Wear, 1980.

[47] Roylance, B. J., J. A. Williams, and R. Dwyer-Joyce. "Wear debris and associated wear phenomena—fundamental research and practice." Proceedings of the Institution of Mechanical Engineers, Part J: Journal of Engineering Tribology, 2000.

[48] Zum Gahr, K-H. "Wear by hard particles." Tribology International, 1988.

[49] Jacobson, Staffan, Per Wallén, and Sture Hogmark. "Fundamental aspects of abrasive wear studied by a new numerical simulation model." Wear, 1988.